UNIVERSITAT POLITÈCNICA DE CATALUNYA BARCELONATECH

Exploring quantum memory schemes in cold atoms for quantum repeaters

Lukas Heller

Universitat Politècnica de Catalunya

PhD program in Photonics

Exploring quantum memory schemes in cold atoms for quantum repeaters

Author:
Lukas Heller

Supervisor:
Prof. Dr. Hugues de Riedmatten

A thesis submitted to obtain the title of Doctor by the Universitat Politècnica de Catalunya

in the

QPSA - Quantum Photonics with Solids and Atoms *group,*
ICFO - The Institute of Photonic Sciences

August 1, 2023

"It's still magic even if you know how it's done."

Terry Pratchett, A Hat Full of Sky

Abstract

Quantum memories are devices that are able to store photonic quantum states and entanglement. Future quantum networks, which could enhance cybersecurity through quantum key distribution, improve the precision in atomic clock networks, and connect quantum devices over long distances, rely on them. This thesis reports on experiments towards improved quantum memories for quantum repeaters used in long-distance quantum communication.

The quantum memory is based on a cloud of laser-cooled Rubidium-87. Thanks to collective interference effects, this system enhances the light-matter interaction compared to that of a single atom. This is exploited to either create long-lived quantum correlations between light and atomic excitations through probabilistic light scattering (DLCZ protocol) or to efficiently absorb an incoming single photon (Raman protocol). In both cases, the excitation is retrieved after a programmable delay as a single photon. An optical cavity around the atoms further enhances the light-matter coupling.

In a first experiment, the DLCZ protocol is combined with a photon echo protocol, allowing for the sequential creation of excitations in N distinguishable temporal modes. This is known as temporal multiplexing. Multiplexing improves the rate at which entanglement is created in a network link by a factor N. Here, the cavity is essential to suppress noise originating from the probabilistic scattering of light in the DLCZ protocol. Ten temporal modes are stored while maintaining strong quantum correlations between the scattered photon and the atomic excitation.

In a second experiment, a quasi-deterministic single photon is stored in

the cloud following the Raman protocol. The photon originates from an ensemble of laser-cooled Rydberg atoms. Strong dipole-dipole interactions prevent the excitation of more than one atom to the Rydberg level, leading to the creation of a single collective Rydberg excitation which is later retrieved as a single photon. A deterministic source, opposed to a probabilistic source, improves the entanglement creation rate as it generates single photons at higher rates. The single photon is stored and faithfully retrieved from the memory while maintaining its single-photon nature. The cavity is not being used in this experiment.

In a third experiment, the retrieval efficiency of a stored excitation is increased by cavity-enhancing the read-out process. Highly-efficient memories are important because the entanglement distribution scales strongly with memory efficiency. The intra-cavity efficiency could be improved by a factor 2-3, depending on the protocol, even for a non-optimal cavity setup.

Finally, ongoing work towards efficient entanglement between an atomic excitation and a telecom photon is presented, involving a cavity-enhanced DLCZ memory, an atomic dipole trap and quantum frequency conversion (QFC) to the telecom C-band. As the memory operates in the optical domain, where photonic transmission losses are large, QFC will be needed to communicate over large distances. This setup will be used in the future for a hybrid experiment connecting the cold atomic memory to a solid state memory.

These investigations target intrinsic limitations of early, proof-of-principle quantum links. They can therefore help to build practical links in the future.

Resum

Les memòries quàntiques són dispositius capaços d'emmagatzemar estats quàntics fotònics i entrellaçament. Les xarxes quàntiques futures, que podrien millorar la ciberseguretat mitjançant la distribució de claus quàntiques, millorar la precisió de les xarxes de rellotge atòmic i connectar dispositius quàntics a llargues distàncies, depenen d'elles. Aquesta tesi presenta experiments cap a memòries quàntiques millorades per a la comunicació quàntica a llarga distància.

La memòria quàntica es basa en un núvol de Rubidi-87 refrigerat per làser. Gràcies als efectes d'interferència col·lectiva, la interacció llum-matèria d'aquest sistema es millora en comparació amb la d'un sol àtom. Això s'aprofita per crear correlacions quàntiques de llarga duració entre la llum i les excitacions atòmiques mitjançant la dispersió probabilística de la llum (protocol DLCZ) o per absorbir de manera eficient un fotó únic entrant (protocol Raman). En ambdós casos, l'excitació es recupera després d'un retard programable com un fotó únic. Una cavitat òptica al voltant dels àtoms millora encara més l'acoblament llum-matèria.

En un primer experiment, el protocol DLCZ es va combinar amb un protocol d'eco de fotons per permetre la creació i la recuperació distingible de N excitacions atòmiques que es van crear seqüencialment en el mateix mode espacial. Això es coneix com a multiplexació temporal. La multiplexació millorarà la velocitat a la qual es crea l'entrellaçament en una xarxa per un factor N. Aquí, la cavitat era essencial per suprimir el soroll provinent de la dispersió probabilística de la llum al protocol DLCZ. Es van emmagatzemar 10 modes temporals mantenint fortes correlacions quàntiques entre el fotó

dispers i l'excitació atòmica.

En un segon experiment, es va emmagatzemar un fotó únic quasi determinista al núvol seguint el protocol Raman. El fotó es va originar a partir d'un conjunt d'àtoms de Rydberg refrigerats per làser. Les fortes interaccions dipol-dipol impedeixen l'excitació de més d'un àtom al nivell de Rydberg, donant lloc a la creació d'una única excitació col·lectiva de Rydberg que després es recupera com un sol fotó. Una font determinista, oposada a una font probabilística, millora la velocitat de creació d'entrellaçament ja que genera fotons únics a velocitats més altes. Vam demostrar que el fotó únic es podia emmagatzemar i recuperar fidelment de la memòria mantenint la seva naturalesa de fotó únic. La cavitat no es va utilitzar aquí.

En un tercer experiment, l'eficiència de recuperació d'una excitació emmagatzemada es va augmentar mitjançant un procés de lectura millorat per una cavitat. Les memòries altament eficients són importants, ja que la distribució de l'entrellaçament escala fortament amb l'eficiència de la memòria. L'eficiència intra-cavitat es va millorar en un factor 2-3, depenent del protocol, fins i tot per a una configuració de cavitat no òptima.

Finalment, es presenta el treball en curs cap a l'entrellaçament eficient entre una excitació atòmica i un fotó de telecomunicacions, que inclou una memòria DLCZ millorada per cavitat, una trampa de dipols atòmics i conversió de freqüència quàntica (QFC) a la banda C de telecomunicacions. Com que la memòria opera en el domini òptic, on les pèrdues de transmissió fotònica són grans, caldrà QFC per comunicar-se a grans distàncies. Aquesta configuració s'utilitzarà en el futur per a un experiment híbrid que connecti la memòria atòmica freda amb una memòria d'estat sòlid.

En aquestes investigacions ens centrem en les limitacions intrínseques de les primeres proves de principi de connexions quàntiques. Per tant, podrien ajudar a construir connexions pràctics en el futur.

Resumen

Las memorias cuánticas son dispositivos capaces de almacenar estados cuánticos de la luz. De ellas dependen las futuras redes cuánticas, que podrían mejorar la ciberseguridad mediante la distribución de claves cuánticas, aumentar la precisión de las redes de relojes atómicos y conectar dispositivos cuánticos a larga distancia. En esta tesis se presentan experimentos para mejorar las memorias cuánticas utilizadas en repetidores cuánticos que permitirán la comunicación cuántica a larga distancia.

Aquella memoria cuántica se basa en una nube de Rubidio-87 refrigerada por láser. Gracias a los efectos de interferencia colectiva, la interacción luz-materia de este sistema es mayor que la de un solo átomo. Esto se aprovecha para crear correlaciones cuánticas duraderas entre la luz y las excitaciones atómicas mediante la dispersión probabilística de la luz (protocolo DLCZ) o para absorber eficazmente un solo fotón entrante (protocolo Raman). En ambos casos, tras la excitación se recupera un fotón único después de un retardo programable. Una cavidad óptica alrededor de los átomos mejora aún más el acoplamiento luz-materia.

En un primer experimento, el protocolo DLCZ se combinó con un protocolo de eco de fotones que permite crear excitaciones atómicas secuencialmente en N modos temporales distinguibles. Esto se conoce como multiplexación temporal. La multiplexación mejorará la velocidad a la que se crea entrelazamiento en una red en un factor N. En este caso, la cavidad era esencial para suprimir el ruido originado por la dispersión probabilística de la luz en el protocolo DLCZ. Se almacenaron 10 modos temporales mientras se mantenían fuertes correlaciones cuánticas entre el fotón dispersado y

la excitación atómica collectiva.

En un segundo experimento, se almacenó en la nube un único fotón cuasi-determinista siguiendo el protocolo Raman. El fotón procedía de un conjunto de átomos Rydberg refrigerados por láser. Las fuertes interacciones dipolo-dipolo impiden la excitación de más de un átomo al nivel de Rydberg, lo que conduce a la creación de una única excitación colectiva de Rydberg que posteriormente se recupera como un único fotón. Una fuente determinista, en contraposición a una fuente probabilística, mejora la velocidad de creación de entrelazamiento, ya que genera fotones únicos a tasas más altas. Demostramos que el fotón único podía almacenarse y recuperarse fidedignamente de la memoria manteniendo su naturaleza de fotón único. En este experimento no se utilizó la cavidad.

En un tercer experimento, se aumentó la eficiencia de recuperación de una excitación almacenada, mejorando el proceso de lectura mediante la cavidad. Las memorias de alta eficiencia son importantes, ya que la distribución del entrelazamiento depende en gran medida de la eficiencia de la memoria. La eficiencia intracavitaria se mejoró en un factor 2-3, dependiendo del protocolo, incluso para una configuración de cavidad no óptima.

Por último, se presentan los trabajos en curso para lograr un entrelazamiento eficiente entre una excitación atómica y un fotón en el rango de las telecomunicaciones, que implican una memoria DLCZ mejorada por cavidad, una trampa dipolar atómica y conversión de frecuencia cuántica (QFC) a la banda C de telecomunicación. Como la memoria funciona en el dominio óptico, donde las pérdidas de transmisión fotónica son grandes, se necesitará QFC para comunicarse a grandes distancias. Esta configuración se utilizará en el futuro para un experimento híbrido que conecte la memoria atómica fría con una memoria de estado sólido.

Estas investigaciones se centran en las limitaciones intrínsecas de los primeros enlaces cuánticos, que se han realizados a escala de laboratorio. Por tanto, podrían ayudar a construir enlaces prácticos en el futuro.

Acknowledgements

This document of barely 120 pages is an attempt to summarise four and a half years of doctoral studies, excitement, sweat and tears. None of this would have been possible without the guidance and support from my supervisor, co-workers, family and friends.

First of all, I would like to thank Hugues for giving me the opportunity to pursue a PhD in this group, trusting that I would be a good candidate to master this experiment and develop it further. Thank you for letting me explore this field of physics that doesn't stop to amaze me. In addition, I would like to thank the thesis committee for taking the time to proofread the manuscript, provide feedback and attend my defence.

This document would not exist without the training, guidance and help from my PostDocs. RuGway, for getting me hooked on atomic physics. Georg, who bequeathed me both a beautiful experiment and flat. Pau, for patiently explaining and showing me everything I needed to know. I would have been lost without you. Klara, for her patience and discussions. Felix, for taking over both the cold-atom and QFC experiments, a truly challenging task, proofreading this thesis and being a really cool guy.

Special thanks go to my accomplice Jan for sharing office, lab, excitement and suffering, for the longest time. It would have been pretty boring without you and your occasional non-sense. And also to Auxi, for being a lab and office mate and later on also a bit of a PostDoc for me. Your kindness and

patience are unprecedented.

I owe a bunch of thanks to the entire QPSA group. You are a great crowd and a true team. You have been always super helpful and I have learnt a lot from you on the way, and on many levels. Specifically, I want to thank Soeren for figuring out QFC with me, and Bernardo and Edu for their "IT support".

In addition, I would like to express my immense gratitude to the teams of the electronic and mechanical workshops, the IT and the Human Resources departments. Your support is essential for the success of numerous PhD projects, and makes life at ICFO so much easier.

Another big shoutout goes to YAO, and the YAO2023 organising team, for keeping me busy during the past months and pulling together a really nice scientific conference. It was an intense but rewarding experience.

Finally, I am very grateful to my family and friends, who supported me in my choices and were always there for me when I needed help.

Thank you Kora, for always listening to me, showing interest in my stuff and empathy when I was complaining about the world. Thanks for supporting me during all this time. Thank you for building Streusel.

Publication list

Publications arising from this work

- Lukas Heller, Pau Farrera, Georg Heinze, and Hugues de Riedmatten. *Cold-Atom Temporally Multiplexed Quantum Memory with Cavity-Enhanced Noise Suppression.* Phys. Rev. Lett. **124**, 210504 (2020).

- Lukas Heller*, Jan Lowinski*, Klara Theophilo, Auxiliadora Padrón-Brito, and Hugues de Riedmatten. *Raman Storage of Quasideterministic Single Photons Generated by Rydberg Collective Excitations in a Low-Noise Quantum Memory.* Phys. Rev. Applied **18**, 024036 (2022).

Publications not included in this thesis

- Jan Lowinski*, Lukas Heller*, Félix Hoffet, Auxiliadora Padrón-Brito, Klara Theophilo and Hugues de Riedmatten. *Strongly non-linear interaction between non-classical light and a blockaded Rydberg atomic ensemble.* (submitted).

* Authors contributed equally to this work.

Contents

Chapter 1

Long-distance quantum communication

Triggered by the invention of the transistor in 1947 and other technological breakthroughs, societies worldwide have transitioned from the Industrial Age to the Information & Communication age. While the times following the Industrial Revolution were marked by mechanisation and electrification, the information age is characterised by (digital) information technology (IT) as the main driver of transformation.

Information technology has radically changed the way we live, work, consume and organise our societies. In the late 1980s (shortly before the year of birth of the author of this thesis), only 1% of the world's technologically stored information was saved digitally, surpassing more than 99% in 2012 [1]. The world's capacity to store information almost doubled every three years during this period of time. Thanks to optical technologies, we can share information across the globe at speeds close to the ultimate speed limit set by nature. The growth of storage and communication capacity is only outperformed by computational capacity, doubling every 1 to 2 years [2]. This has led to data-driven technologies such as artificial intelligence (AI) and 'Big Data'. In March 2015, world's top Go player Lee Sedol lost to the Google AI AlphaGo. Sedol later renounced from professional Go referring

to AI as "an entity that cannot be defeated" [3].

This development is not limited exclusively to classical IT anymore. Exploiting the laws of quantum mechanics, the so-called Second Quantum Revolution has led to quantum-mechanical counterparts for storage, communication and processing units. In recent times, the event which generated most public attention was the announcement by Google to have reached quantum supremacy with a sampling algorithm in 2019 [4][1]. Those devices share conceptual analogies with classical IT, with the main difference being the underlying carrier of information, the qubit. Quantum-mechanical superposition and entanglement has, however, many use cases going beyond quantum information applications. Quantum technologies hold promise for processing at unprecedented speed of certain computational problems, sensing devices that surpass classical noise limitations, more secure communication or enhanced precision of atomic clocks, amongst others.

My experimental effort is dedicated to the development of *long-distance quantum communication through fiber networks*. In this chapter, I introduce concepts that could lead to its implementation in the not-too-distant future.

1.1 Quantum links & quantum internet

In analogy to the classical internet, Kimble introduced the easy-to-grasp term "Quantum Internet" [6] for a network that features the inter-connectivity of (quantum) processor nodes through (quantum) transmission links[2]. Such a network will enable numerous novel applications [8]. In an early development stage with limited functionality, applications could include trusted-node networks for point-to-point quantum key distribution, entanglement-based quantum cryptography [9], or teleportation [10]. Further stages featuring the possibility to store and process quantum information enable blind & distributed quantum computing [11], or improved sensitivity in sensor networks

[1] This claim was later-on softened, as it was shown that the same computation could be performed classically in a similar amount of time [5].

[2] The term ´Quantum Internet' seems to be used somewhat differently in the literature. While some use it only for a global network of quantum computers [7], others include any two-party inter-connectivity via quantum links [8].

like telescopic arrays [12] and atomic clock networks [13]. Apart from direct qubit state transfer, employed for example in two-party cryptography such as the BB84 key distribution protocol [14], all those applications rely on entanglement distributed to the parties taking part in the communication.

There is little ambiguity that the communication channel will use photons as information carrier. Photons travel fast, they do not interact with one another and exhibit low transmission losses in either free-space links or fiber networks. The quantum information they carry will then be stored, processed and interconnected in some kind of light-matter interfaces, which form the physical quantum nodes of the network. Some nodes might be responsible for processing information, others may take care of distributing information across the network. Therefore, the network will most likely be hybrid and incorporate different platforms depending on the needs of the individual node. Promising candidates for network nodes providing the necessary light-matter interaction include single trapped atoms & ions [15], ensembles of atomic emitters [16, 17], rare-earth-ion-doped solids [18, 19], quantum dots [20], colour centres in diamonds [21], among others.

Interfacing those different platforms while optimizing their light-matter interaction is a challenging task. The platforms differ in terms of bandwidth and wavelength. Hence, quantum frequency conversion (QFC) [22] and/or bandwidth conversion will become necessary. Additionally, many quantum communication operations rely on quantum interference, for example when performing Bell-state measurements [10]. This requires indistinguishable photons. Despite significant progress in the development of its building blocks [23–28], a functional, hybrid network has not been implemented yet. There have been, however, experimental steps towards this goal [29, 30].

Engineering light-matter interaction and making hybrid devices talk to each other is a necessary requirement. However, in the envisioned quantum internet, devices are potentially very far apart from each other, and the photon arrival probability diminishes exponentially with distance. QFC could alleviate the problem by converting any wavelength to the telecom range, allowing low-loss transmission in optical fibers at ≈ 1250 to 1675 nm (many candidates for light-matter-interfaces operate in the VIS or NIR range). Nevertheless, even for high-quality optical cables with a state-of-

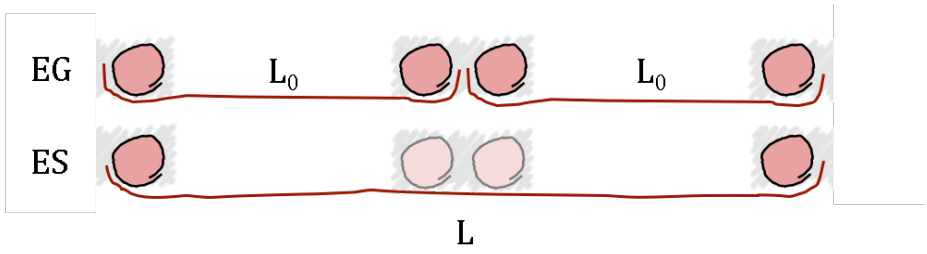

Figure 1.1: A schematic quantum repeater with two links and one central node. EG: entanglement generation; ES: entanglement swapping; spheres: Light-matter interfaces storing remote heralded entanglement.

the-art attenuation coefficient of $\alpha = 0.2\,\mathrm{dB\,km^{-1}}$ in the telecom C-band, the probability to find an input photon on the other side of the channel is reduced to 1% after only 100km of optical fiber cable.

While the classical solution would be to amplify the signal, this is not a possibility for quantum states due to the non-cloning theorem [31]. One proposed pathway to long-distance quantum communication is the *quantum repeater* [32], which we will discuss in the following section.

1.2 Quantum repeater based on optical quantum memories

The task is to establish remote entanglement, which is then consumed as a resource by the communicating parties for their protocol of choice.

1.2.1 Operation principle of the quantum repeater

The proposal relies on entanglement generation on shorter links, for which photon transmission rates are higher, followed by entanglement swapping between adjacent links to increase the entangled distance. This is shown schematically in Fig. 1.1 for a channel divided into two links. First, attempts to generate remote entanglement are performed on each link separately.

The link that succeeds first, stores its entanglement until the second link also signals successful entanglement generation. An entanglement swapping operation then connects the two links, effectively extending the entangled distance. This way, entanglement between both ends of the channel is created even though they have never interacted.

Here, two important requirements have been implicitly introduced: entanglement storage and heralded entanglement generation. If $P \ll 1$ would be the probability for entanglement creation in one trial across the whole channel L without division, the individual success probability per link is increased to $P^{1/2}$, because photons travel only half the distance. Of course, the probability for both links to succeed simultaneously is $P^{1/2}P^{1/2} = P$, so there would be no net-gain in terms of overall rate. In order to increase the overall rate, entanglement has to be stored in each link in *quantum memories* until both links have succeeded and entanglement can be swapped. This also requires that entanglement is created in a *heralded* way, as otherwise the entanglement swapping would be probabilistic.

For the case of two links, we can quantify the gain from dividing the channel, assuming perfect memories and $P \ll 1$. $T = L/(cP)$ would be the average time it takes to generate heralded entanglement across the *undivided* channel, where c is the speed of light in the channel. L/c is the time a photon signal needs to travel to a central station and produce a heralding click, plus a classical signal that is sent back to the note to inform about the success. This, in turn, ultimately limits the repetition rate at which entanglement trials can be performed. Dividing the channel in two reduces the average time of entanglement generation per link to $T_0 = L/(2cP^{1/2})$. The average time one needs to wait until both links have succeeded is $T_1 = 3/2\,T_0$. The coefficient $3/2$ accounts for the fact that entanglement has to be created independently on *two* links. Intuitively, if T_0 is the time it takes to generate entanglement on one link, it takes $T_0/2$ for either of the two links to succeed. Following this, one needs to wait another time T_0 for the remaining link, adding up to $3/2\,T_0$ ([17], Appendix A). Including also the success probability of the BSM in the entanglement swapping, P_{BSM}, the average entanglement distribution time is $T' = 3/2\,L/(2cP^{1/2}P_{\mathrm{BSM}}) + L/(2c) \approx 3/2\,L/(2cP^{1/2}P_{\mathrm{BSM}})$, where the time needed to inform the end nodes about a successful trial has been

neglected. For $P = 1\%$ and $P_{\mathrm{BSM}} = 1/2$, this provides a more than 26-fold decrease in average waiting time T', compared to T, for a fixed repetition rate [3]. A general formula for n intermediate links is given in [17]. It was shown that the repeater strategy relaxes the exponential scaling with distance to a polynomial scaling [4][32].

The first proposal for the actual implementation of a practical repeater was introduced by Duan, Lukin, Cirac and Zoller (DLCZ proposal) [16]. We will review this proposal in the next section.

1.2.2 DLCZ-type quantum repeater

Each link is comprised of two cold atomic ensembles, one at each end, see Fig. 1.2. The use of ensembles, as opposed to single quantum systems, is motivated by its strong and controllable coupling to light. In each ensemble, quantized long-lived atomic excitations are generated, that are correlated with a "write" photon. Those correlations are generated by shining a laser pulse on the atoms, prepared in a certain inter-atomic state, and collecting probabilistically scattered Raman photons that correspond to decay to a different atomic state. In contrast to an *absorptive* memory, which stores an input quantum state, this type of memory is also called *emissive* memory, as the quantum state is generated internally.

Overlapping those photonic modes on a central beam splitter allows for the generation of entanglement between the ensembles. The detection of a single photon click after the beam splitter heralds the existence of a single atomic excitation shared between two memories. This Fock-entangled state for the first link in Fig. 1.2 becomes

$$|\Psi\rangle = 1/\sqrt{2}\ (|1_A 0_B\rangle \pm e^{i\phi}\,|0_A 1_B\rangle), \tag{1.1}$$

where the sign depends on which detector clicked, and the phase ϕ is a

[3] T assumes one entanglement attempt per communication time. In direct transmission, the repetition rate can potentially be much larger.

[4] Of course, T' still scales exponentially with distance. However, if one optimizes the number of links for a given distance, the scaling becomes polynomial.

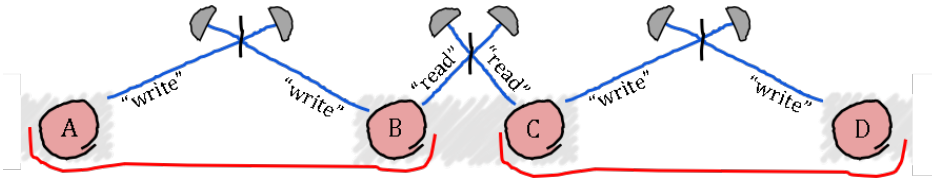

Figure 1.2: Schematic DLCZ quantum repeater with two links and one central node. Sphere: atomic ensemble; black line and grey half circles: beam splitter and single-photon detectors; blue lines: transmission channels.

differential phase between the two photon paths and excitation lasers[5]. Once all the links have succeeded, the excitations are read-out on demand as "read" photons, and mixing those modes on a second beam splitter swaps entanglement and extends the entangled distance. For a fully-functional repeater, a second parallel channel is necessary to convert this single-excitation number-state entanglement into two-photon entanglement, for example in the polarisation basis [16, 23]. The details of this scheme will be reviewed in chapter 2. For now, it is sufficient to understand that the coherence of the stored excitation is (furthermost) related to the fact that we use very cold atoms, and the strong light-matter interaction needed for "reading" is provided by collective ensemble effects.

The obvious beauty and simplicity of this scheme comes at the cost of noise, that is, additional excitations that go undetected because of limited storage, transmission and detection probabilities. As all ensembles have an equal probability of emitting a "write" photon, and as correlations are generated *probabilistically* involving many atoms, there is the chance that more than one excitation is created per link. This is detrimental to the desired atom-photon correlation and can only be by avoided by limiting the excitation probability to $p \ll 1$, in turn limiting the entanglement generation rate. This is a problem intrinsic to any protocol building on

[5]As a single detector click is sufficient to herald entanglement, generating path entanglement in this way is efficient. Heralding entanglement on the detection of the two photons is also possible, which is more robust against phase fluctuations at the expense of lower heralding rates [17].

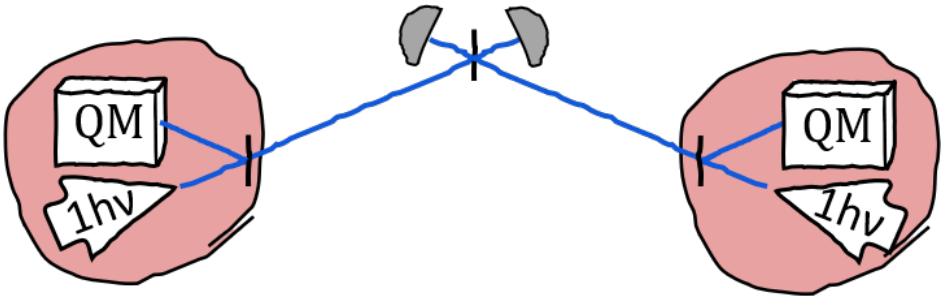

Figure 1.3: Schematic link based on deterministic single-photon sources. Sphere: light-matter interface, comprised of a quantum memory (QM) and single-photon source ($1h\nu$); black line and grey half circles: beam splitter and single-photon detectors; blue lines: transmission channels.

probabilistic photon sources, like, for example, spontaneous parametric down-conversion (SPDC). Additionally, as the heralding of successful trials introduces communication overhead, the repetition rate is low.

In this thesis, I will experimentally investigate two proposals that respond to these problems. The probabilistic photon source, limiting the generation probability, can be replaced by a deterministic single-photon source. The necessity for a heralding signal to travel between the nodes, limiting the repetition rate, can be mitigated by multiplexed memories, able to store and read out many excitations independently. Those proposals are discussed in greater detail in the following sections.

1.2.3 Quantum repeater based on single photon sources & quantum memories

The problem of multi-photon errors was tackled in a proposal by Sangouard *et al.* [33]. The scheme is sketched out in Fig. 1.3. The main building block consists of a single photon source emitting a photon deterministically, a beam splitter with reflection and transmission coefficients α and β satisfying $|\alpha|^2 + |\beta|^2 = 1$, and an absorptive quantum memory. At the start of each trial, both sources generate a photon. The modes that are transmitted

through the beam splitter are overlapped on a central station, while the reflected modes are stored in a memory. If both photons are reflected, the memories are loaded, but no entanglement was heralded, so the trial will be repeated. If one of the photons is transmitted and the other one stored, this leads to a heralding click. This is the desired case. If both photons are transmitted, and one photon is detected, this can lead to a false heralding which can not be distinguished from the second case. However, in the latter case, none of the memories will be loaded, and subsequent entanglement swapping will not succeed. Upon a photon click at the central station, the generated state reads

$$\rho_{AB} = \beta \left|0\right\rangle \left\langle 0\right| + \alpha \left|\Psi\right\rangle \left\langle \Psi\right|, \text{ with } \left|\Psi\right\rangle = 1/\sqrt{2}\ (\left|10\right\rangle \pm \left|01\right\rangle). \tag{1.2}$$

In none of the scenarios, a component of the form $|11\rangle$ is generated, which would correspond to more than one excitation being present across the link. Therefore, errors due to multi-photon components in the read-out are suppressed. This means that this scheme can operate at photon generation probabilities close to unity, which in turn enhances entanglement distribution rates (provided that the source efficiency is above a given threshold). This gain was exemplarily calculated for a repeater with a length of 1000km in [33]. The entanglement distribution rate is enhanced by a factor 18 in this deterministic protocol, compared to the probabilistic DLCZ protocol, for equal memory efficiencies of 90% and a source efficiency of 95%. The implementation is difficult, however, as the photons generated by deterministic photon sources usually cannot be stored efficiently in quantum memories. In chapter 5, we experimentally investigate the storage of single photons from a quasi-deterministic source in a laser-cooled ensemble.

1.2.4 Multiplexed quantum repeater

The heralding probability for quantum repeater architectures based on single-photon interference scales with the probability $p_{\text{her}} \propto p_{\text{gen}} p_{\text{trans}} p_{\text{det}}$ to generate, transmit and detect a single photon at the intermediate station. For repeaters based on probabilistic sources, p_{gen} is kept small in order to suppress the emission of multiphoton components. For any repeater scheme,

p_{trans} and p_{det} are limited by losses and current detector technologies. On the other hand, as the node has to wait for a signal indicating a successful heralding event, the memory can only be reset after a communication time $\tau_{\text{com}} = L_0 n/c$, where L_0 is the fiber length between two nodes and n the refractive index of the fiber core. For a link with $L_0 = 100\,\text{km}$, which is roughly the distance that optimises the total success probability in repeater channels, τ_{com} becomes $\approx 500\,\mu\text{s}$. The heralding rate $R = R_{\text{gen}} p_{\text{her}}$ is therefore limited by p_{her} and the repetition rate $R_{\text{gen}} = 1/\tau_{\text{com}}$ of photon generation.

As p_{her} is intrinsically limited, the only way to increase R is by performing more attempts per communication time. For this, a resource-efficient way is the implementation of multi-mode memories, capable of holding many distinguishable entangled states simultaneously and reading them out selectively [34]. The rate then scales linearly with the number of modes N stored in memory, as long as $N p_{\text{her}} \ll 1$. In turn, larger entanglement distribution rates also relax the storage time requirements. Probably, a practical quantum repeater will require multiplexing of some sort.

Ensemble-based platforms are well suited for multiplexing. Different degrees of freedom have been considered for the multiplexed modes, such as frequency, space or time. In chapter 4, the implementation of a temporally multiplexed DLCZ source will be demonstrated.

1.3 Light-matter interfaces for quantum communication

This section introduces quantum memories and other light-matter interfaces that might play a role in future long-distance quantum communication. We will review the state-of-the-art of the individual building blocks as well as proof-of-concept experiments providing heralded entanglement to the user.

1.3.1 Quantum memories for quantum repeaters

A quantum memory is a device that stores quantum states locally. In the scope of quantum repeater applications, the input and output states will be encoded as optical photons. Storage can be performed in any system that provides strong light-matter interaction for the mapping between the photonic field and the matter system, and sufficient coherence in order to be able to store, for example, matter qubits encoded between different atomic levels[6]. Several platforms have been investigated as quantum memories, these include single atoms or ions as the text-book examples of single quantum systems [15, 35–38], ensembles of neutral atoms in free space [16, 39–43], ensembles of ions in solid-state hosts [18, 19, 44, 45], and color center in diamonds coupled to long-lived nuclear spins [21, 46]. For a recent review on quantum memories, see [47].

So far, we have assumed "perfect memories" without defining what qualifies as such. We will now review the most important figures of merit, under the premise that it is to be used in a repeater [47, 48]. The references present only a small selection of the state-of-the-art, for the respective figure of merit and for different platforms. As for laser-cooled atomic ensembles, a more extensive review can be found in chapter 2.

Storage efficiencies η_{wr} and $\eta_{r|w}$ The total probability for storage and retrieval of an input signal, η_{wr} (defined for absorptive memories), or the conditional read-out probability heralded on a "write" click, $\eta_{r|w}$ (defined for emissive memories). According to [17], for a distance $L = 600$km, a reduction in the memory efficiency from 90% to 89% leads to an increase in the entanglement distribution time by 10-14% (depending on the protocol, and assuming a fixed number of links). This is because the memory efficiency intervenes at every swapping stage.

The efficiencies quoted here were measured for short storage times (compared to their memory coherence times). Wherever possible, the memory

[6] For synchronisation purposes, a delay line with on-demand read-out (e.g a cavity with a "switch" to couple light in and out) could also qualify as a memory. But this is not the type of memory that we are interested in for building a repeater, as storage times are low.

coherence times τ (usually given as a $1/e$ decay time) are also given.

Single atoms or ions in free space couple only weakly to electromagnetic modes, and the coupling is therefore irreversible. Collection efficiencies are limited to a few percent, even with high-numerical aperture objectives [49]. To achieve reversible coupling, emitters can be placed in cavities, which enhance light-matter interaction. For example, single-photon storage on a single ^{87}Rb atom in a fiber cavity was heralded by collecting a second Raman photon into a second cavity, with in-fiber heralding probability of 22% [50]. The photon could then be retrieved with $\eta_{r|w} = 56\%$ (measured in fiber, $\tau = 170\,\mu s$). Unheralded storage with $\eta_{wr} = 22\%$ (measured in free space) was also shown in a similar system [51]. Moving on to ensemble platforms, [52] holds the record for quantum storage in solid state hosts ($\eta_{wr} = 69\%$, $\tau = 3\,\mu s$) applying a gradient-echo protocol in Pr^{3+}:Y_2SiO_5. In our group, with the same host material Duranti et. al achieved high efficiencies via cavity-enhanced atomic frequency comb storage (AFC storage) with light at the single-photon level ($\eta_{wr} = 62\%$, $\tau = 89/4\mu s$)(unpublished). Storage of weak coherent light was shown via gradient-echo in hot vapor ($\eta_{wr} = 87\%$, $\tau = 22\,\mu s$) [53] and later-on in cold atoms with improved coherence ($\eta_{wr} = 87\%$, $\tau = 1\,ms$) [54]. In cold atoms, storage of single-photon qubits with close-to-unity efficiency and fidelity was demonstrated ($\eta_{wr} > 85\%$ (qubit storage), $\tau = 15\,\mu s$) [55, 56], implementing the electromagnetically induced transparency protocol (EIT storage). The highest efficiency across all platforms was achieved for classical light EIT storage ($\eta_{wr} = 92\%$, $\tau = 325\,\mu s$) [57].

In chapter 6, I experimentally investigate the possibility to increase the storage efficiency of our memory through cavity enhancement.

Memory lifetime τ How long an excitation can be stored is quantified by the memory lifetime. Heralded entanglement needs to be stored at least until entanglement is generated across the whole channel, i.e. the rate of entanglement generation between nodes has to exceed their decoherence rates [58]. As introduced in subsection 1.2.4, the entanglement heralding rate in each link $R = R_{gen}p_{her}$ is limited by the heralding probability $p_{her} \ll 1$

and the repetition rate R_{gen}. Taking into account also the entanglement swapping success probabilities across links, the storage time requirements easily reach 50 ms and more. This can be alleviated by multiplexing. The elementary communication time in fiber of $\tau_{\text{com}} \approx 500\,\mu\text{s}$ is the ultimate lower limit.

Wherever applicable, the storage efficiency for short storage times (compared to the memory coherence times) is quoted as well.

For a cryogenically cooled nitrogen-vacancy center coupled to nuclear spin pairs, [59] reported the longest dephasing time of any individually controllable quantum system ($T_2^* = 1.9\,\text{min}$). Coherence times exceeding one hour were shown for a single $^{171}\text{Yb}^+$ trapped ion [60] and 100ms for a single ^{87}Rb atom [51]. Longest optical storage for classical light was reported in a rare-earth-ion-doped solid ($^{151}\text{Eu}^{3+}$:Y_2SiO_5) ($\tau = 7\text{h}$ (1/e), $\eta_{wr} = 5.2\%$) [61]. In room-temperature atoms, which don't require vacuum or cryogenic support and might be field-deployed quickly [62], non-classical correlations could be maintained for $\tau = 0.68\,\text{ms}$ ($\eta_{r|w} \approx 5.5\%$) [63]. The longest light storage (with classical pulses) in cold atomic ensembles was achieved with a ^{87}Rb cloud ($\tau = 16\text{s}$, $\eta_{wr} = 14\%$) [64] using the EIT protocol. Memory-photon entanglement with the longest lifetime was shown on the same platform ($\tau = 458\text{ms}$, $\eta_{r|w} = 58\%$) [65].

Storage Fidelity Fidelity is a comparative measure of the output state to some second state. For an absorptive memory the fidelity could, for example, quantify how faithfully the output qubit state resembles the input qubit state. This is described by the conditional fidelity, which is conditioned on a photon emission by the memory. For an input state $|\phi_{\text{in}}\rangle$, the conditional fidelity is the state overlap

$$F = \langle\phi_{\text{in}}|\rho_{\text{out}}|\phi_{\text{in}}\rangle\,, \tag{1.3}$$

with ϕ_{out} being the reduced density matrix of the output state, and ϕ_{in} a pure input state. Noise introduced by the storage protocol, detector dark counts, or any other change to the input state, deteriorate the fidelity. For ensemble memories, the fidelity conditioned on the remission of the photon

(so-called conditional fidelity) and efficiency are decoupled, as decoherence only acts as a loss of efficiency [66]. A background-subtracted conditional fidelity of 99.5% for qubit storage was measured for EIT storage in cold atoms [67].

Multimode capacity Quantifies the number of independent excitations N that can be stored in one memory. As detailed in a seminal paper [34], the entanglement generation rate on the elementary link increases linearly with the mode number, if $Np_{\text{her}} \ll 1$. Given that the entanglement generation probability in repeater schemes is limited to the percent-regime, modal multiplexing is also the only feasible way to relax the storage time requirements, as the average time it needs to generate entanglement is reduced by the same factor.

Memories based on ensembles are naturally suited for multiplexing, because the number of excitations that can be stored is large. Multiplexing can be implemented in different degrees of freedom (such as frequency, space, angle or time) or any combination of those, as demonstrated for example in [68] for orbital-momentum states. In a solid-state ensemble, storage of heralded single photons in 1250 temporal modes at 970nm via the AFC-protocol was shown recently [69]. In laser-cooled ensembles, a multiplexed DLCZ-type memory with 225 individually accessible memory cells was realized [70]. The different memory cells (essentially different spatial regions within the same atomic cloud) are addressed with 2D acousto-optic deflectors. Bipartite entanglement across 550 photonic modes (encoded in 1100 wave-vector-multiplexed angular modes divided into H and V polarisation) was also demonstrated, imaged with a single-photon-resolving CMOS camera [71]. For memories based on single quantum systems, ten individually controllable nuclear-spin qubits coupled to an a nitrogen-vacancy center [72] where shown, although it is not clear if this a scalable approach.

In cold atoms, little attention was payed to the time degree of freedom. We will experimentally investigate this approach in chapter 4.

1.3.2 Wavelength & bandwidth conversion

The wavelength and bandwidth of the photon has to match the storage platform. This is particularly important in heterogeneous networks comprised of distinct matter systems. While the center wavelength is determined by atomic properties (and usually lies in the visible or NIR, except for memories based on Erbium [73, 74]), the bandwidth depends also on the storage protocol.

Passive pulse shaping with optical modulators [75] is possible, but lossy. A more efficient approach are storage protocols that allow for bandwidth-tunable writing and reading [76]. Atomic photon sources can emit photons with arbitrary waveshape [77], tunable over more than three orders of magnitude [78].

Modulators can also be used to shift light frequencies, but the shift is limited to a few GHz. Depending on the available transitions, four-wave mixing (FWM) in atomic ensembles can allow for wavelength conversion [79]. QFC can help to bride the gap between different platforms, as the input and output frequencies can be chosen freely. This was illustrated in our group by demonstrating photonic quantum state transfer of a photonic time-bin qubit, generated in a cold-atom DLCZ quantum node, to a solid-state based quantum memory in a neighboring laboratory via cascaded QFC [29]. The development of efficient conversion to and from the Telecom band is particularly interesting for long-distance, low-loss transmission [80, 81]. A polarisation-insensitive converter with very high external device efficiency of 57% (including filtering) was demonstrated [82].

In chapter 7, I am investigating efficient frequency conversion of light at an atomic resonance to the Telecom C-band.

1.3.3 Photon sources interfaced with memories

If the memory does not create light-matter correlations *internally* like in the original DLCZ proposal, *external* photon sources are needed.

Probabilistic two-photon sources can be based on FWM in cold or warm atomic ensembles, or spontaneous parametric down-conversion (SPDC) (see

[83] for a performance comparison). FWM in atoms natively provides wavelength & bandwidth - compatible photons for memories based on the same species [84, 85]. Narrow-band pair sources (bandwidth of 960kHz) of high spectral brightness (2.38x10^4 pairs/s/MHz/mW, $g^{(2)}_{SI}(\tau = 0) \approx 3.7$) [86] have been realized in hot vapour, and high-quality correlations of transform-limited photon pairs($g^{(2)}_{SI}(\tau = 0) \approx 5800$, [87]) at high rates ($5 \times 10^4\,\mathrm{s}^{-1}$[88]) were achieved in cold atoms. Combining FWM sources or DLCZ-type sources with suitable memories, entanglement between light (both in the telecom and visible range) and matter was shown [24, 79, 89, 90]. Alternatively, SPDC in non-linear crystals based on $\chi^{(2)}$- or $\chi^{(3)}$ optical non-linearities can be exploited [91]. The bandwidth of those photons is usually too large for most storage protocols, but if combined with an enhancement cavity, sub-MHz linewidth can be achieved as well [92]. The spectral brightness is better than for atomic sources (3.94x10^5 pairs/s/MHz/mW, 2.4MHz line width [93]). One big advantage is that the source can be designed such that it emits one photon in Telecom to generate entanglement at a distance and a memory-compatible photon to store entanglement locally [73, 94]. This development has lead to long-lived atom-photon entanglement in a rare-earth-ion-doped solid [95] or single-photon ground state storage in hot vapor [96].

Deterministic single-photon sources can be built from single emitters (see [97] for a performance comparison). To date, quantum dots (QDs) provide very pure single photons ($g^{(2)} \approx 10^{-3}$, [98]) at extremely high rates (above $23 \times 10^6\,\mathrm{s}^{-1}$, [99]). Deterministically created photons from a GaAs QD were slowed down in a hot vapour cell of ^{87}Rb atoms [100]. The storage of attenuated laser pulses that are comparable to the bandwidth and pulse intensity of photons from QDs was shown as well [101]. However, building a large number of memory-compatible dots with equal properties is difficult [20], and so far AFC and off-resonant cascaded absorption (ORCA) memories have been the only memory types which successfully stored quantum dot photons [102, 103], albeit with low efficiency and storage time. Although color centers in diamond can also serve photon sources [104], their main strength is to serve as a communication qubit mediating between a photonic

qubit and a nuclear spin qubit [21, 58]. Single ions or atoms can also provide memory-compatible photons. Photon rates of 2 kHz ($g^{(2)} \approx 10^{-2}$) [105] were measured with a cavity-coupled ^{87}Rb atom, and rates of 18 kHz ($g^{(2)} \approx 10^{-3}$) were measured with a free-space $^{174}Yb^{+}$ ion [106]. Interfacing of those photons with memories was achieved, demonstrating remote entanglement between a single ^{87}Rb atom in a high-finesse cavity and a ^{87}Rb BEC [107], and between two such atoms coupled to two cavities [26]. A narrowband single photon source based on fluorescence emission from a single organic dye molecule was also demonstrated [108].

Recently, ensembles of Rydberg atoms have received considerable attention [109]. Strong dipole-dipole interaction between Rydberg states prevents the promotion of more than one atom to the Rydberg state, as long as inter-atomic distance is small compared to the interaction length [110]. This excitation is then read out as a single photon. [111] realized this requirement by trapping cold atoms in an optical dipole trap, while [112] expanded this scheme to tiny glass cells filled with room-temperature vapors. Highly pure, indistinguishable photons ($g^{(2)} \approx 10^{-4}$) [97] at high generation efficiencies of up to 44% (in fiber) [113] have been generated. Quantum interference of those photons with photons emitted from a single ^{138}Ba ion was demonstrated [30].

We experimentally investigate such a source in chapter 5, motivated by the repeater protocol introduced in subsection 1.2.3.

1.3.4 Heralded entanglement between remote nodes

Eventually, remote heralded entanglement is the fundamental requirement for a quantum repeater, so it worth reviewing experimental advancements. To date, all experiments demonstrating useful heralded entanglement (i.e. to be used in long-distance communication) coupled *identical* quantum nodes. Heralded number-state entanglement generation between two DLCZ memories was demonstrated for the first time in 2005 [114]. A functional DLCZ quantum node implementing path entanglement for two pairs of ensembles was shown two years later by the same group [23]. In 2008, by using a two-photon detection scheme and local entanglement generation, entanglement

swapping with storage and retrieval of light was realized [115]. More recently, GHZ-type entanglement of three DLCZ nodes separated by a few meters [116] was demonstrated. By employing QFC to the telecom O-band, two of those DLCZ nodes in neighbouring labs were later-on entangled via up to 50km of metropolitan-scale fibers through telecom-heralding [117]. DLCZ-type entanglement between two quantum dots was demonstrated (albeit with low coherence times) [118], which is also the platform that demonstrated the largest entanglement generation rate for distant entanglement as of today (7.3 kcps [119]). Number-state entanglement between atoms in two hot vapor cells separated by a few centimeters was shown [24]. High-fidelity entanglement between single ^{87}Rb atoms [26] and, very recently, single trapped $^{40}Ca^{+}$ ions in cavities [28] proved the maturity of cavity-enhanced interfaces. By collecting atomic fluorescence with high-NA objectives, two free-space $^{88}Sr^{+}$ ion qubits [49] and ^{87}Rb atoms got entangled [120], as well. In the latter experiment, QFC of the 780nm photons (emitted by the atoms) to the telecom band facilitated heralded polarisation entanglement over 33km of fiber at an entanglement heralding rate of 0.05 cps (the atoms where located in different sites 400m apart). Entanglement between absorptive solid-state ensemble memories based on AFC storage has been demonstrated both for near-IR heralding [121] and telecom-heralding of up to 62 temporal modes [27]. Deterministic entanglement delivery, where the entanglement was generated at a higher rate than it decayed, was shown between two nuclear spins in diamonds, separated by two meters [58], and two trapped ions, separated by one meter [122]. That network was then extended to include a third node, and entanglement generation followed by entanglement swapping was demonstrated [25], which constitutes the first demonstration of a multi-node quantum network.

1.4 Summary & thesis outlook

Remote entanglement distribution will enable novel applications in quantum communication, computing and sensing. The quantum repeater offers a solution to improving distribution rates beyond what is achievable in direct

transmission. Quantum repeaters are based on heralded entanglement between remote quantum memories that form an elementary repeater link, and on entanglement swapping between the elementary links to extend the entanglement distance. Depending on the repeater architecture, the memories have to emit photons entangled with a matter-degree of freedom (emissive memory), or absorb and reemit an already entangled photon (absorptive memory). To that end, efficient, long-lived, multiplexed and low-noise quantum memories are being developed, together with memory-compatible photon sources. Wavelength and bandwidth conversion will ensure coupling between the systems, and enable transmission in the telecom regime. Some experiments have already shown a memory-assisted rate scaling advantage in entanglement generation by synchronising entanglement swapping between two nodes [81, 123–125]. The distribution of long-distance heralded entanglement was demonstrated [28, 117, 120].

A versatile and robust platform to implement long-lived entanglement are laser-cooled atomic ensembles [16]. Heralded entanglement was shown for the first time in this system [114]. Close-to-unity efficiencies [53–56] and second-long coherence times [64, 65] can be combined with spatial, angular or temporal multiplexing [70, 71, 126]. The implementation of deterministic photon sources based on Rydberg atoms [97, 127] and wavelength conversion [79] was also demonstrated, emphasising its potential. Those properties render this platform a more-than-promising candidate for versatile nodes in future quantum networks.

In this thesis, I will report on experiments addressing three of the challenges mentioned in this chapter. The first one, presented in chapter 4, is the development of a time-multiplexed emissive quantum memory. Multiplexing increases the entanglement distribution rates and at the same time relaxes storage time requirements. The second one, presented in chapter 5, discusses the implementation of a low-noise absorptive memory, which is interfaced with a deterministic single photon source based on Rydberg atoms. This experiment can serve as a steppingstone to build an improved repeater link based on on-demand single-photon sources. Finally, in chapter 6, it is shown that the limited storage efficiency of the ensemble memory can be enhanced by a cavity. Highly-efficient memories help to increases the distribution rates

in repeater architectures. As an outlook, in chapter 7, ongoing work towards a novel cavity-enhanced entanglement scheme is discussed. The chapter includes recent improvements of a frequency conversion setup that connects the memory photons with the telecom band. This combined scheme targets efficient light-matter entanglement between an atomic excitation and a telecom photon – a fundamental requirement for any repeater architecture.

Chapter 2

Laser-cooled ensemble memories

With the advent of laser-cooling in the 1980's, trapped clouds of very cold atomic matter have become available to experimentalists. Among other uses, they are also interesting for photon storage. Atomic ensembles allow for strong light-matter coupling because the light interacts with many emitters simultaneously. The atoms also move very little, preserving information stored in the form of collective excitations for longer times.

In this chapter, I will introduce the concept of collective enhancement and how it can be exploited for quantum light storage. The principle of two storage protocols will be investigated in more detail. I will also motivate the use of a low-finesse cavity to enhance light-atom coupling. The chapter concludes making a case for laser-cooled ensemble memories.

2.1 Absorption and emission of free-space emitters

Loosely following Tanji-Suzuki *et al.* [128] and Simon [129], we start by investigating the *absorption* of an incident light field by a single atom. For a Gaussian input beam, the input power $P_{\text{in}} = |\varepsilon|^2/2$ is a function of the square of the mode amplitude $\varepsilon = E_0\sqrt{\epsilon_0 c A}$, which relates to the field amplitude

E_0 at the focus position, the electric constant ϵ_0 and the effective mode area $A = \pi w^2/2$, where w is the mode waist. The absorption process can be modeled as destructive interference between the input light ε propagating forward, and the light scattered from the atom into the same mode M, ε_M:

$$\frac{P_{\text{abs}}}{P_{\text{in}}} \equiv \sigma_0/A = \frac{|\varepsilon|^2 - |\varepsilon + \varepsilon_M|^2}{|\varepsilon|^2} = -\frac{\varepsilon^*\varepsilon_M + \varepsilon_M^*\varepsilon + \varepsilon_M^*\varepsilon_M}{|\varepsilon|^2} \tag{2.1}$$

Here, we have also introduced the resonant absorption cross-section σ_0. To compute eq. 2.1, we need to know the fraction of forward-scattered light associated with mode M. From the radiation pattern of an electric dipole and the mode overlap with our Gaussian mode M one finds $\varepsilon_M = i(\frac{k}{\pi w^2 \epsilon_0}\alpha)\varepsilon \equiv i\beta\varepsilon$, assuming that the incident light is polarised along the oscillator axis. $k = 2\pi/\lambda$ is the wave vector, and α is the complex *polarisability* of the atom,

$$\alpha = 6\pi\epsilon_0 c^3 \frac{\Gamma/\omega_0^2}{\omega_0^2 - \omega^2 - i\Gamma(\omega^3/\omega_0^2)}. \tag{2.2}$$

$\omega(\omega_0)$ is the radial frequency of the probe light (atomic resonance), and Γ is the natural linewidth. The polarisability is an important quantity that relates not only with material absorption, but also with emission, dispersion or the potential energy in electromagnetic fields, for example for dipole trapping (chapter 7). As far as the dependency on ω is concerned, eq. 2.2 holds true for both the classical and quantum-mechanical description.

On resonance ($\omega = \omega_0$), $\alpha = i6\pi\epsilon_0 c^3/\omega_0^3$ is purely imaginary and ε_M acquires a π-phase shift with respect to ε. We now evaluate the ratio

$$\frac{P_{\text{abs}}}{P_{\text{in}}} \approx -\frac{\varepsilon^*\varepsilon_M + \varepsilon_M^*\varepsilon}{|\varepsilon|^2} = -\frac{i(\beta - \beta^*)\varepsilon^*\varepsilon}{\varepsilon^*\varepsilon} = 2\text{Im}(\beta). \tag{2.3}$$

This becomes $2\frac{6}{k_0^2 w_0^2} \equiv 2\chi_{\text{fs}}$, which is the single atom optical depth (OD). χ_{fs} is a purely geometric factor which depends only on the wave vector on resonance, k_0, and the waist w_0 of the Gaussian mode at the focus. A comparison with eq. 2.2 reveals that the absorption cross section is $\sigma_0 = 2A\chi_{\text{fs}} = 3/(2\pi)\lambda^2$. By integrating the dipole pattern over all angles,

one finds that χ_{fs} also links the power *emitted* (bidirectionally) into the mode M to the total radiated power,

$$\frac{2P_M}{P_{4\pi}} = \chi_{\mathrm{fs}}. \tag{2.4}$$

χ_{fs} has been identified as the *single-atom free-space cooperativity*. For standard values for $k_0 \approx 1 \times 10^7, w_0 \approx 1 \times 10^{-4}$, $\chi_{\mathrm{fs}} \ll 1$. This shows that a single emitter couples only weakly to a photonic mode. Strong light-matter coupling is, however, necessary for any kind of light-matter interaction involving the generation, storage and readout of photonic states [130]. Ensembles of emitters can enhance this interaction. For unordered ensembles, a simple counting argument reveals a linear scaling of absorption and scattering strength with the number of emitters N. The on-resonance optical depth equals $N2\chi_{\mathrm{fs}}$. Light scattering into a direction different than the propagation direction of the input light is N-times the single atom scattering eq. 2.4 [1]. The atoms also introduce a phase shift $\phi_N = \mathrm{Re}(N\beta)$.

It should be noted that for multi-level atoms χ_{fs}, as derived for the classical dipole radiation pattern, takes the above form only for the strongest transition (for example, $|5^2S_{1/2}, F = 2, m_F = 2\rangle \rightarrow |5^2P_{3/2}, F' = 3, m_{F'} = 3\rangle$ on the D2 line of Rubidium). In this case, a quantum-mechanical treatment reveals $\chi'_{\mathrm{fs}} = \chi_{\mathrm{fs}}\zeta$, where ζ is the branching ratio of the transition, computed from the reduced dipole matrix elements.

2.2 Storing quantum information as collective excitations

When a single emitter is used as memory, it is easy to pinpoint the one particle that has interacted with an incoming photon. However, atomic ensembles absorb and emit collectively: a single photonic excitation is stored delocalized in a collective state. Assuming that all the N atoms couple

[1] Light scattering in forward direction is collectively enhanced by N^2 due to interference of the atomic emitters, independent of their ordering [131].

equally to the optical mode, this state is an equally weighted superposition

$$|\Psi_a\rangle(t) = \frac{1}{\sqrt{N}} \sum_{j=1}^{N} c_j(t,x) \, |g_1 ... s_j ... g_N\rangle \tag{2.5}$$

of all possible excitation paths from the ground state $|g\rangle$ to the storage state $|s\rangle$. $c_j(t,x)$ is a complex phase factor. As long as c_j evolves equally for all emitters (or is restored at the time of readout) the state coherence is preserved, i.e. $|\langle\Psi_a(t)|\Psi_a(0)\rangle|^2 = 1$. In this case, the excitation can be retrieved in a coherent manner into a well-defined direction, as detailed below.

The maximum theoretical *retrieval efficiency* of the stored excitation can be determined from the ratio between the desired collective radiation $P_{\mathrm{M,N}}$, and the total radiation emitted by the atoms $P_{\mathrm{M,N}} + P_{4\pi,N}$. The power emitted into the phase matched direction scales quadratically with N, as the coherently scattered field of all the emitters adds up linearly and $P_{\mathrm{M,N}} \propto |\varepsilon_M|^2 \propto |i\beta\varepsilon N|^2$, while the power emitted into all 4π scales linearly with N as the phase pattern is random. The relation between power scattered into a particular mode M versus 4π is given by eq. 2.4, so

$$\eta_{\mathrm{ret}} = \frac{P_{\mathrm{M,N}}}{P_{\mathrm{M,N}} + P_{4\pi,N}} = \frac{P_{\mathrm{M,N}}/P_{4\pi,N}}{P_{\mathrm{M,N}}/P_{4\pi,N} + 1} = \frac{N\chi_{\mathrm{fs}}/2}{N\chi_{\mathrm{fs}}/2 + 1} = \frac{\mathrm{OD}/4}{\mathrm{OD}/4 + 1}. \tag{2.6}$$

This formula motivates the use of ensembles as quantum memories [2]. eq. 2.6 can also be written as $\eta_{\mathrm{ret}} = \Gamma_{\mathrm{M,N}}/\Gamma'$, where $\Gamma_{\mathrm{M,N}}$ is the decay rate into the mode M and Γ' is the total decay rate of the excited state population [132]. Indeed, experiments on collective decay in Dicke superradiance have shown that the decay rate of the collective state is enhanced, with $\Gamma' = \Gamma + \Gamma_{M,N} = (1 + b_0/12)\Gamma$, were b_0 is a parameter proportional to $N\chi_{\mathrm{fs}}$ [131, 134]. This leads to the same quantitative interpretation of the retrieval efficiency and highlights the close connection to superradiant emission.

[2] Different sources cite a slightly different scaling, depending on parameter definitions [132, 133]

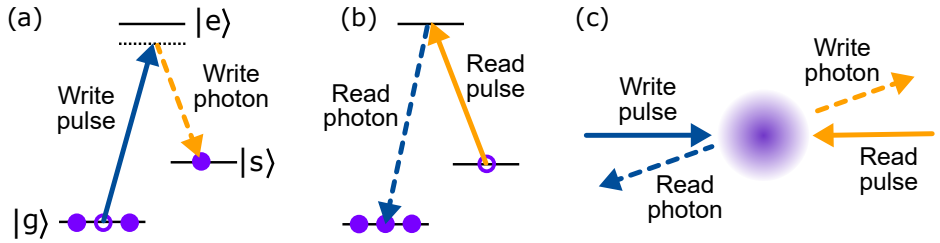

Figure 2.1: DLCZ scheme in cold atoms. (a) An off-resonant write pulse scatters on the atoms, generating a spin wave. (b) The spin wave is read-out by a resonant read pulse. (c) Counterpropagating control pulses are linked to counterpropagating photons.

2.2.1 The DLCZ scheme – Built-in atom-photon entanglement

One way to generate correlations and/or entanglement between a local excitation and a flying photon is the DLCZ protocol, proposed in a seminal paper by Duan, Lukin, Cirac and Zoller [16] and depicted in Fig. 2.1. First proof-of-principle experiments were carried out by Kuzmich *et al.* [40] and van der Wal *et al.* [41]. In an atomic Λ-scheme, two ground levels $|g\rangle$ and $|s\rangle$ are optically coupled via the excited state $|e\rangle$. The protocol is initialized by a write pulse, off-resonantly scattering on the $|g\rangle \rightarrow |e\rangle$ transition, see panel(a). Photons scattered into a particular mode M are detected and herald the generation of the aforementioned collective excitation

$$|\Psi_a(0)\rangle = \frac{1}{\sqrt{N}} \sum_{j=1}^{N} e^{i(\boldsymbol{k}_W - \boldsymbol{k}_w)\boldsymbol{x}_j} \, |g_1 ... s_j ... g_N\rangle \, . \tag{2.7}$$

In analogy to electromagnetic waves, the exponential term defines a spatial phase profile. The object in eq. 2.7 is therefore termed *spin wave*, and $\Delta\boldsymbol{k} = \boldsymbol{k}_W - \boldsymbol{k}_w$ is the spin wave vector, resulting from the absorption of a photon from the write pulse $\boldsymbol{k}_W$ and re-emission of the scattered photon $\boldsymbol{k}_w$. After a programmable time, the excitation is retrieved by an on-resonant read pulse, coupling $|s\rangle \rightarrow |e\rangle$, see panel (b). In analogy to Bragg reflection of light

from a periodical crystalline lattice of emitters, this operation is expected to scatter light into a well defined output mode. Indeed, owing to collective interference of the atoms constituting the spin wave, the corresponding photon is emitted back on the $|e\rangle \rightarrow |g\rangle$ transition into a phase-matched direction given by the cancellation of momentum, $\boldsymbol{k}_W - \boldsymbol{k}_w + \boldsymbol{k}_R - \boldsymbol{k}_r = 0$. If we choose $\boldsymbol{k}_W = -\boldsymbol{k}_R$, then it conveniently results that $\boldsymbol{k}_r = -\boldsymbol{k}_w$, as depicted in panel (c). The atom-photon correlation can be exploited to entangle neighbouring nodes in a repeater chain. Subsequently, the atom-atom entanglement can be read out to swap entanglement across nodes. The maximum theoretical retrieval efficiency of this process was derived in eq. 2.6. A more thorough analysis, considering the optimal spin wave shape, suggests a slightly worse scaling $\eta_{\mathrm{ret}} \approx 1 - 2.9/\mathrm{OD}$ (for $\mathrm{OD} \gg 1$) [132]. At high OD, the efficiency drops because of off-resonant interaction with neighbouring excited states [67, 130][3]. Several decoherence mechanisms limit the collective retrieval further, see section 2.4.

Not only the re-emission probability, but also the scattering probability into the mode M during the writing process is given by the cooperativity introduced before. As the write photon is the result of probabilistic scattering on independent emitters, the photon number fluctuates and it is not guaranteed that exactly one photon scatters in each attempt. The generated state is rather given by

$$|\Psi\rangle = \sqrt{1-p} \sum_{k=0}^{\infty} p^{k/2} \, |k_w, k_s\rangle \tag{2.8}$$

where $|k_w, k_s\rangle$ is the k's two-mode state of photonic (**w**rite) and atomic (**s**pin wave) mode. $|\Psi\rangle$ is called *two-mode squeezed state*. It is formally equivalent to the state generated in spontaneous parametric down-conversion, with the difference that here one mode is an atomic number state. p is the probability to generate at least one photon, as $|\langle 00|\Psi\rangle|^2 = (1-p)$. The probability to generate at least two photons is p^2. In practice, this multi-photon component

[3] [67] investigated EIT storage, but the dephasing mechanism (i.e. coupling of the control pulse to neighbouring excited state) stays valid.

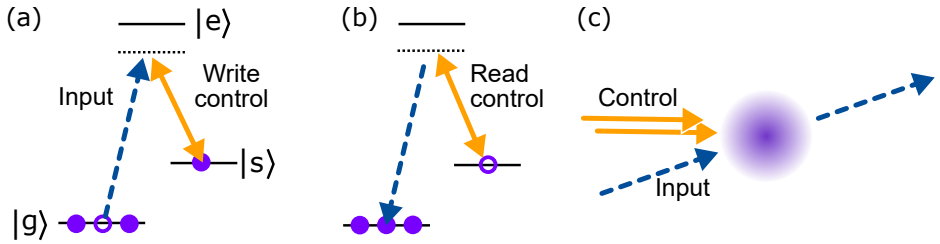

Figure 2.2: Raman scheme in cold atoms. (a) An off-resonant input is mapped into the memory by means of a control pulse in two-photon resonance with the storage state, generating a spin wave. (b) The spin wave is read out by an off-resonant read pulse. (c) Copropagating control pulses are linked to copropagating photons.

cannot be differentiated from the single-photon component (due to photon-number insensitive detectors and losses), so p has to be kept low to generate the desired state $|11\rangle$ with high fidelity.

2.2.2 The Raman scheme – Storage of external quantum states

In a similar fashion, an input quantum state can also be stored as a spin wave. Here, I will sketch the operation principle of the off-resonant Raman protocol, as it is implemented in chapter 5. This protocol was proposed in [135] and implemented for the first time in [136] with weak classical light pulses in hot vapor. It has since found application for cold atomic memories as well [137, 138].

The schematics of the Raman-type memory is illustrated in Fig. 2.2. We depart from the same Λ-scheme introduced previously. The input photon couples the $|g\rangle \rightarrow |e\rangle$ transition off-resonantly. However, analogous to stimulated Raman adiabatic passage (STIRAP) [139], this photon is now mapped to the second groundstate with the help of a strong coupling pulse $\boldsymbol{k}_{C,w}$. This generates a spin wave with wave vector $\Delta\boldsymbol{k} = \boldsymbol{k}_i - \boldsymbol{k}_{C,w}$, which is equal in magnitude to the vector in DLCZ configuration but with opposite

sign (the emitted photon on the $|e\rangle \rightarrow |s\rangle$ transition is *added* to the control field). The spin wave can be retrieved after a programmable delay via a second off-resonant coupling pulse $\boldsymbol{k}_{C,r}$ as an output light field $\boldsymbol{k}_i'$. Choosing $\boldsymbol{k}_{C,r} = \boldsymbol{k}_{C,w}$ leads to phase-matched re-emission into forward direction in the same mode, $\boldsymbol{k}_i' = \boldsymbol{k}_i$. In this case, [132] predicts a total storage and retrieval efficiency as a function of optical depth as $\eta_{wr} \approx 1 - 19/\mathrm{OD}$ (for $\mathrm{OD} \gg 1$). Again, at high OD, the efficiency is expected to drop because of interaction with neighbouring excited states, similar to the DLCZ case. In backward retrieval (i.e. engineering the second control pulse such that the excitation is retrieved backwards), the maximum achievable efficiency increases [132, 138]. The intuitive understanding for this behaviour is that the photon (which was mostly absorbed in the input layers of the atomic medium) does not have to travel through the entire medium and the chance of loosing it is reduced[4].

The first coupling pulse is off-resonant to the $|s\rangle \rightarrow |e\rangle$ transition, but in two-photon resonance with the input photon. Its role is to open a virtual state that the input light can couple to. This virtual state contains almost no contribution of the excited state, and the photon is therefore not absorbed into $|e\rangle$. From Maxwell-Bloch equations it can be seen that for appropriate time-dependent coupling Rabi frequency $\Omega_{C,w}(t)$, which depends on the temporal shape of the input, the excitated state of the Λ-scheme has zero contribution to absorption of the input light field [141]. Instead, the atomic population is directly transferred to $|s\rangle$.

As this is an off-resonant protocol, the bandwidth of the input photon is not limited to the acceptance bandwidth of the excited state, which is in the MHz-range for alkaline atoms. Instead, the bandwidth is limited by the proximity to the neighbouring ground- or excited state (depending on which is closer), and the control pulse duration. For ^{87}Rb, the ultimate limit is the hyperfine ground state splitting (6.8 GHz). Storage of photons with a bandwidth exceeding 1 GHz has been shown in hot vapours [136]. This

[4] Note that the DLCZ protocol, as introduced before, is already retrieving in backward direction, so to speak. Engineering the absorption profile a bit further can still improve the retrieval efficiency [140].

makes the Raman memory one of the memories with highest time-bandwidth product (i.e. the number of temporal modes that can be stored within its memory lifetime).

2.2.3 Further protocols

An entire "zoo" of protocols exists that allows the storage of quantum states in atomic or solid-state ensembles, including hybrid protocols combining different approaches. Although they are not a subject of this thesis, we will briefly review them for completeness. I would also like to refer the reader to the PhD thesis of Nunn [141], which contains an instructive overview over the different protocols available for photon storage in ensembles.

Electromagnetically-induced transparency (EIT) is an interference effect between different decay channels that allows the steering of on-resonance absorption & dispersion, mediated by a coupling beam on the $|e\rangle \rightarrow |e\rangle$ transition [142][5]. In the **EIT memory**, an on-resonant light pulse traveling through a medium under EIT condition can be absorbed to a spin level and re-emitted. If the coupling pulse Rabi frequency is high, the excited state $|e\rangle$ is split into two distinct levels. This strong-coupling limit is called the Autler-Townes regime, and is exploited in the **ATS memory** [143]. If the optical transition is inhomogeneously broadened (due to Doppler broadening in warm vapour or electronic crystal fields in solid-state memories), protocols based on photon echo can be implemented. These include the atomic frequency-comb **(AFC) memory** [18, 144] and the class of memories based on controlled reversal of inhomogeneous broadening **(CRIB)** [19, 145]. Long-lived spin storage is possible by mapping the optical excitation into a ground state by means of control pulses.

[5]The reason why the read photon in the DLCZ protocol is not re-absorbed by the highly dense medium is precisely because the read-out pulse renders the medium transparent by EIT.

2.3 Enhanced interaction of light with an optical cavity

The former sections should have convinced the reader that atomic ensembles provide both a versatile and easy-to-implement platform for quantum light-matter interaction. In this section, we motivate how light-matter interaction can be further enhanced with a low-finesse optical resonator, loosely following Tanji-Suzuki *et al.* and Simon [128, 129].

Single atom in a cavity We depart from the single-atom case and investigate absorption of light by this emitter in the cavity. Rate equations for fields inside cavities are detailed in appendix A. Expanding eq. (A.3), we can additionally introduce a radiating emitter into a (linear) cavity, with equal mirror transmittivities T. One can show that the absorption behaviour is governed by a cavity cooperativity χ. For a resonant cavity,

$$\frac{P_{\mathrm{abs}}}{P_{\mathrm{in}}} = \frac{2\chi}{(1+\chi)^2} \tag{2.9}$$

where χ

$$\chi = \frac{4\chi_{\mathrm{fs}}}{T} = \frac{24F/\pi}{k_0^2 w_0^2}. \tag{2.10}$$

We introduced the cavity finesse $F = 2\pi/(2T)$. For $\chi \ll 1$, eq. 2.9 resembles eq. 2.3, so 2χ is the cavity-aided optical depth. eq. 2.10 is called the Purcell factor. It can be understood as the free-space cooperativity times the average number of photon round trips $F/(2\pi)$ inside the cavity (plus a factor four accounting for the larger intensity at the antinode and an additional factor 2 from the fact that photons pass the atom twice per roundtrip).

For $\chi > 1$, the mode of the atom and the mode of the cavity strongly mix when the atomic resonance hits the cavity resonance. Both cavity transmission and atomic emission show a normal-mode splitting, known as the vacuum Rabi splitting $2g = \sqrt{\chi\Gamma\kappa}$, where Γ is the atomic transition line width and κ is the cavity linewidth. g is called the atom-cavity coupling coefficient. For $\chi \ll 1$, or if the cavity is far detuned from the atomic

resonance (where the atomic absorption reduces faster than the dispersion), the enhancement of light scattered into the cavity mode (compared to scattering in the absence of the cavity $P_M^{(0)}$) is simply [6]

$$\frac{P_C}{2P_M^{(0)}} = \frac{4F}{\pi}. \tag{2.11}$$

Atomic ensemble in a cavity It turns out that the ensemble cooperativity is again enhanced by a factor N, same as for the ensemble cooperativity without cavity. The scattering enhancement is

$$\frac{P_C}{2P_M^{(0)}} = \frac{4F}{\pi} N/2 \tag{2.12}$$

where the factor 1/2 arises from the spatial distribution in a standing wave cavity. The dispersive effect of the atom leads to a cavity frequency shift $\delta\omega_c$ in units of the cavity line width κ

$$\frac{\delta\omega_c}{\kappa} \approx HN\chi\frac{\Gamma}{4\Delta} \tag{2.13}$$

where $\Delta = \omega - \omega_0$ is the detuning from atomic resonance. H is a collective coupling parameter, which considers the distribution of atoms in the interference pattern of the standing-wave cavity.

For a single atom, $\chi > 1$ requires a high-finesse cavity with a small mode waist at the position of the atom, compare eq. 2.10. However, using an ensemble of emitters allows for much stronger cooperativities already at moderate finesse. We can again compute maximum retrieval efficiencies. For a single atom, the emission of light power scattered into the cavity mode vs. the power scattered into all directions is

$$\frac{P_c}{P_{4\pi}} = \chi\frac{\kappa^2}{\kappa^2 + 4\delta^2} \tag{2.14}$$

[6] In the case of a triangular ring cavity, which is the cavity design that will be used in this thesis, the scattering rate through one output port becomes $P_C/P_M^{(0)} = 2F/\pi$.

where κ is the cavity decay rate and δ the detuning of the cavity from the excitation light[7]. Following the argument of subsection 2.2.1, we compute the maximum retrieval efficiency in DLCZ, for a standing wave-cavity, as

$$\eta = \frac{P_{\mathrm{C,N}}}{P_{\mathrm{C,N}} + P_{4\pi,N}} = \frac{P_{\mathrm{C,N}}/P_{4\pi,N}}{P_{\mathrm{C,N}}/P_{4\pi,N} + 1} = \frac{N\chi}{N\chi + 1}. \tag{2.15}$$

This shows that even in low-finesse cavities, this efficiency can approach unity for moderate values of $\chi \propto F$.

2.4 Challenges for cold atomic memory experiments

Several effects limit the memory lifetime and efficiency, or introduce noise. Controlling those mechanisms is still subject of many investigations.

2.4.1 Dephasing mechanisms

As mentioned in section 2.2, eq. 2.5, the atomic phase c_j needs to be carefully controlled to ensure collective rephasing and highly efficient readout. Unfortunately, dephasing due to *atomic motion*, uncontrolled *inhomogeneous broadening* and *collisions* are irreversible and introduce decoherence. Such excitations will be retrieved into random directions and are lost. Additionally, in the case of the DLCZ protocol, only a fraction $\chi_{\mathrm{fs}}/2 \ll 1$ of the scattered write photons is collected, corresponding to $2/\chi_{\mathrm{fs}} \gg 1$ additional spin waves that go undetected (see eq. 2.4). When those spin waves dephase, their spurious retrieval also constitutes to noise.

Motional dephasing Random motion affects $e^{i\Delta\boldsymbol{k}\boldsymbol{x}_j} = e^{i\Delta\boldsymbol{k}\boldsymbol{v}_j t}$, scrambling the spin wave phase when atoms move along the wave vector by more than the wavelength $\lambda_s = 2\pi/|\Delta\boldsymbol{k}|$. Assuming a three-dimensional Maxwell-Boltzmann velocity distribution, the efficiency drops as a function of storage

[7] This formula is apparently independent of the detuning of the probe light from the atomic resonance, Δ.

time following a Gaussian decay [146]

$$\eta(t) \propto |\langle \Psi_a(t)|\Psi_a(0)\rangle|^2 = e^{-\frac{k_B T \Delta k^2 t^2}{m}}. \tag{2.16}$$

Here, T is the ensemble-average temperature, k_B is the Boltzmann constant and m the atomic mass. $|\boldsymbol{k}_W| \approx |\boldsymbol{k}_w| = 2\pi/\lambda$, so $|\boldsymbol{\Delta}k| = |\boldsymbol{k}_W - \boldsymbol{k}_w| \approx 2\pi/\lambda \sin(\theta)$. For small angle θ, $\sin(\theta) \approx \theta$. The direction of this vector is roughly perpendicular to both the write pulse and write photon mode. As an example, for an angle of 1°, $\Delta k = 140 \times 10^3\,\mathrm{m}^{-1}$ and $\lambda_s = 45\,\mu\mathrm{m}$.

We can identify the memory lifetime as the 1/e decay time $\tau_m = \sqrt{m/(k_B T)}\lambda/(\sin(\theta)2\pi)$. This shows that for long memory lifetime it is important to i) maintain a small angle between the control mode and the photon mode, and to ii) work with cold ensembles. Alternatively, atoms can be trapped in a longitudinal lattice, thereby inhibiting atomic diffusion along the direction of the wave vector [64, 147]. Another approach is to "zero" $\Delta\boldsymbol{k}$ by a pair of Raman pulses driving another Λ-transition [148]. Those Raman beams are arranged exactly such that their resulting wave vector cancels the wave vector during writing, $\Delta\boldsymbol{k}_{\mathrm{Raman}} = -\Delta\boldsymbol{k}$. The Raman beams are applied a second time before read-out. Memory lifetimes of the order of the cloud lifetime have been achieved.

Inhomogeneous level broadening & level shift The spin wave also possesses a time-dependent phase factor $e^{i\Delta\omega_j t}$, where $\Delta\omega_j = \Delta E_j/\hbar$ is the energy difference between $|g\rangle$ and $|s\rangle$ for the j's atom. The unperturbed level splitting (around 6.8 GHz for our system, see section 3.5) is a global phase factor and can be pulled out of the sum. However, magnetic or electronic fields can additionally shift the levels. For example, magnetic-field sensitive Zeeman levels experience a linear shift $\Delta E(F, m_F) = \mu_B g_F m_F B_z$ when subject to a small magnetic field, see eq. 3.1. Static or varying electric fields also introduce shifts, see for example the ac Stark shift in dipole trapping in subsection 7.3.1.

If those shifts are applied in a controlled fashion, storage protocols can exploit photon echo techniques. This class of memories is called controlled reversible inhomogeneous broadening (CRIB) memories or gradient echo

memories (GEM) [19], which can be used to store photons either in the excited state or on ground states (then, it would be called Λ-CRIB). We will make use of CRIB for the storage of multiple temporal modes in chapter 4.

If those shifts can not be controlled (stray fields, for example), this might lead to dephasing. We exemplarily calculate the decay due to an uncompensated linear magnetic *gradient*, $B(z) = B_0 z$, acting on the states $|g\rangle = |F, m_f\rangle$ and $|s\rangle = |F', m'_f\rangle$ which we assume are field-sensitive. The splitting becomes $\Delta\omega_j = \omega_0 + \mu_B B_0 z(g_F m_F - g'_F m'_F)/\hbar = \omega_0 + cz$, where we have identified $c = \mu_B B_0(g_F m_F - g'_F m'_F)/\hbar$. Consider the case of a three-dimensional ensemble with Gaussian spatial distribution, $\rho = \rho(x, y, z)$. As the cloud is usually much bigger than the photonic mode, we only have to consider the distribution along the propagation direction z, $\rho(z) = 2/(L\sqrt{\pi})e^{-4z^2/L^2}$. The retrieval efficiency is then proportional to

$$\eta_{\text{inh}} \propto \left| \frac{1}{N} \sum_{j=1}^{N} e^{i\Delta\omega_j t} \right|^2 \propto \left| \int_{-\infty}^{\infty} \rho(z) e^{i\Delta\omega_j(z)t} dz \right|^2 \propto \left| \int_{-\infty}^{\infty} e^{-4z^2/L^2} e^{iczt} dz \right|^2 . \tag{2.17}$$

This is the Fourier transform integral of a Gaussian, resulting in a Gaussian decay $\eta_{\text{inh}} \propto e^{-c^2 L^2 t^2/8}$ with the characteristic 1/e decay of $\tau_{\text{inh}} = \sqrt{8}/(cL)$. In general, an inhomogeneously broadened line, where the spin broadening follows a Gaussian distribution with spin line width γ_{inh} (in Hertz), results in a Gaussian decay [149]

$$\eta_{\text{inh}} \propto e^{-\frac{t^2 \gamma_{\text{inh}}^2 \pi^2}{2 \ln 2}} . \tag{2.18}$$

Different techniques can be applied to counteract inhomogeneous broadening. Magnetic fields can be shielded (μ-metal) or compensated with magnetic field coils, if the field at the atom position can be inferred somehow. Differential light shifts introduced by the spatially-varying field of dipole traps can be canceled by a combination of a dc 'magic' magnetic field with circularly-polarised trapping beams [150] or by laser-induced two-photon compensation through a second light field [147]. Drifts can also be counteracted by dynamical decoupling of the two ground states [64].

In the above example of spin (de)coherence between two well-defined sublevels $|F, m_f\rangle$ and $|F', m'_f\rangle$, a homogeneous field did not affect the coherence. If several excitation paths are possible (for example because of different decay channels in the DLCZ write process), and each one is represented with its normalized probability P_i, those different spin wave *classes* are allowed to interfere. This leads to an oscillating retrieval efficiency with periodic revivals

$$\eta_{\text{hom}} \propto \left| \frac{1}{N} \sum_{j=1}^{N} P_1 e^{i\Delta\omega_1 t} + P_2 e^{i\Delta\omega_2 t} + ... \right|^2 = \left| P_1 e^{i\Delta\omega_1 t} + P_2 e^{i\Delta\omega_2 t} + ... \right|^2 . \tag{2.19}$$

This effect is exploited in [151] to engineer atom-light entanglement in the time-bin basis. To suppress this interference, one possibility is to null the homogeneous field. Alternatively, one can optically pump the atomic spins to a single sublevel and apply a level scheme that allows for only one spin wave class. We follow the second strategy in the experiments conducted in this thesis.

Atomic collisions & light scattering The information stored in the spin state can get lost by spin flips. Those can be induced by atomic collisions or scattering of photons. The probability for a spin flip (associated with information loss) within a given unit of time is a function of the scattering rate and the atomic population in $|s\rangle$, leading to an exponentially decaying retrieval efficiency. If those effects are relevant depends on the probability to scatter within the storage time. In dilute clouds, like in this thesis, atomic collisions during the storage time are unlikely. However, if for example a dipole trap is employed, photon scattering can occur when the dipole trap light is close to a ground state transition.

2.4.2 Atom loss

Information can get lost as atoms leave the focus due to diffusion and fall in gravity. Assuming a temperature of 30 µK, the average velocity of atoms

in the cloud is $\overline{v} = \sqrt{\frac{8k_BT}{\pi m}} \approx 85\,\mathrm{mm\,s^{-1}}$. Similarly, the cloud experiences a translation in free fall equal to $s_{\mathrm{free}} = 1/2gt^2$. As the focus of the laser mode in the cloud is roughly 100 µm, the atoms would need around 1 ms to propagate out of the focus and around 4.5 ms to fall out of the focus. These effects can be neglected, as it is still one order of magnitude above the memory lifetime of $\approx 100\,\mu\mathrm{s}$ in our experiment. However, those two effects lead to a gradual loss of OD, making the retrapping of the cloud necessary. Trapping the atoms in a dipole trap or lattice allows for much longer interrogation times [64, 65]. A more ambitious approach is to operate a quantum memory, based on a Bose-Einstein-Condensate, in space [152]. The low temperature of the gas slows down expansion, and in the absence of gravity the cloud's center of mass is not moving.

2.4.3 Noise in the read-out

The memory should not add photon noise to the output. Noise can, for example, degrade the quality of the quantum correlations, or reduce the fidelity of the retrieved states. In general, noise is induced by the control pulses, either directly through scattering or indirectly through fluorescence and processes like four-wave mixing. The reduction of noise was vital to achieve the results reported in the two publications in this thesis (chapter 4 and chapter 5).

A definite comparison is difficult, as noise is strongly protocol-dependent. However, it should be noted that laser-cooled ensembles (of alkaline atoms) show some advantages for noise reduction over ensembles of rare-earth ions doped into solid-state hosts. Firstly, atomic ensembles are very pure systems, so control pulses do not resonantly couple to states or emitters that play no role in the storage process (as long as the state initialisation is executed correctly). Secondly, the atomic excited states are short-lived, so no long-lasting fluorescence is expected. Thirdly, the dipole moments are stronger, so control pulses can be less intense to produce the same Rabi frequencies.

Different protocol-dependent strategies exist to reduce noise in laser-cooled memories. If the noise is broadband, or at a different frequency

than the signal, narrowband filters like etalon filters, interference filters or Bragg gratings can be used [62, 82, 127]. If the memory operation is cavity-enhanced, the cavity interaction can be engineered such that the signal is enhanced while the noise is suppressed [116, 117, 153]. In the specific case of DLCZ, noise from dephased spin waves can also be reduced through asymmetrical photon-collection [154]. Four-wave mixing noise, which is generated at the signal frequency, is difficult to filter. However, it can be reduced for a specific choice of atomic levels and excitation pulse polarisation [63].

2.5 A case for laser-cooled ensemble memories

In light of the preceding sections, it now seems justified to highlight some important achievements in the field of laser-cooled memories.

Close-to-unity storage and retrieval efficiencies were demonstrated with optically thick clouds. This includes CRIB storage ($\eta_{wr} = 87\%$, $\tau = 1\,\mathrm{ms}$) [54] or single-photon qubit storage implementing the EIT protocol ($\eta_{wr} = 85\%$, $\tau = 15\,\mu\mathrm{s}$) [55]. The highest efficiency, across all platforms, was achieved for classical light EIT storage ($\eta_{wr} = 92\%$, $\tau = 325\,\mu\mathrm{s}$) [57]. However, due to a slightly different phasematching condition, those extended clouds cannot be used to generate DLCZ photon pairs efficiently (see also chapter 6). The largest retrieval efficiencies reported for DLCZ in free space are therefore comparably low, for example $\eta_{r|w} = 50\%$ in [155]. The solution is the combination of an optically thin, small ensemble with an enhancement cavity. With this approach, intra-cavity efficiencies of $\eta_{r|w} = 77 - 88\%$ have been achieved [65, 116, 130, 156], with extra-cavity efficiencies as high as 73% [116].

Long-lived memory operation is possible, if the dephasing mechanisms described in section 2.4 are well-controlled. The longest light storage in cold ensembles was achieved through the combination of various techniques, employing the EIT protocol ($\tau = 16\mathrm{s}$, $\eta_{wr} = 14\%$) [64]. In that work, an atomic clock transition was used, rendering the storage insensitive to homogeneous fields. The dephasing from gradient fields was counter-acted

by microwave dynamical decoupling. A 1D lattice held the atoms in place, at the same time inhibiting motional dephasing. The differential ac Stark shift of the 1D lattice was canceled by using an elliptically polarized lattice in combination with a "magic" magnetic field. Motional dephasing can also be switched off through spin vector "freezing" by means of a pair of Raman beams, which nulls the spin wave vector and renders the spin wave insensitive to motional dephasing [148, 157].

Eventually, long storage times and high retrieval efficiencies need to be combined with qubit or entanglement storage. In recent work, polarisation-encoded atom-photon entanglement was generated in a DLCZ type memory [65], and stored for $\tau = 458\,\mathrm{ms}$ (1/e) in a lattice trap. The long storage time was made possible through light shift compensation. The intra-cavity qubit retrieval efficiency was as high as $\eta_{r|w} = 58\%$. After 1s, the Bell inequality was still violated by more than 2 standard deviations.

Laser-cooled ensembles provide a superb platform for highly-efficient, long-lived, low-noise quantum memories. They also allow for multi-mode storage and can be interfaced with other platforms or sources (see also section 1.3). For those reasons, some of the most promising quantum link experiments were realized with this platform [116, 117, 157].

Chapter 3

The laser-cooled light-matter interface

The following chapter is dedicated to the implementation of the light-matter interface in the lab. The first section introduces the general experimental cycle of sample preparation and interrogation. The second and third sections recall the relevant properties of Rubidium-87, our storage medium, and the techniques of magneto-optical trapping & cooling. The fourth section describes the actual experimental setup. Finally, the interface is characterized, operated both as a DLCZ interface and a Raman-type memory.

3.1 Overview

The experiment cycles between sample preparation and interrogation, as illustrated in Fig. 3.1. Inside a glass vacuum chamber, atoms are loaded into a three-dimensional magneto-optical trap (MOT) directly from background gas pressure. This is followed by polarisation-gradient cooling (PG cooling), during which atoms are cooled below the Doppler limit. During cooling, the trapping potential is already switched off and atoms are released from the trap. In the subsequent optical pumping stage (OP), atoms are prepared in a specific sub-state $|F, m_F\rangle$ which depends on the experimental requirements.

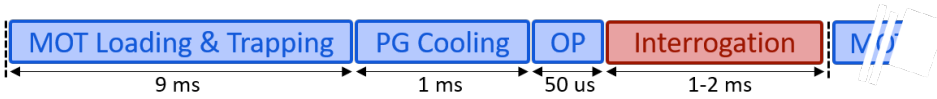

Figure 3.1: The experiment alternates between preparation & interrogation.

The atomic ensemble can then be interrogated for either DLCZ pair generation or Raman storage. After some time, atoms are lost due to diffusion and gravity, and have to be re-trapped. The whole cycle takes around 12 ms.

The experiment is controlled by an FPGA-based control system (HYDRA from Signadyne). It features digital and analogue outputs to control, for example, the magnetic field coils or acousto-optic modulators (AOMs) for optical beam preparation. Arbitrary wave forms can be generated with nanosecond-resolution. It also features a time-stamping module to log single photon detection events. Conditional logic can be implemented upon the detection of trigger events, such as photon detections or external triggers.

3.2 Properties of Rubidium-87

Information on ^{87}Rb in this section was gratefully adapted from [158]. Rubidium is an alkaline atom (atomic number 37) possessing one valence electron. Its most abundant isotope is ^{85}Rb (isotope signature of 82 %). The other stable isotope and our atom of choice is ^{87}Rb (28 %).

With an odd mass number of 87, and knowing that protons and neutrons are spin-1/2 particles, its nuclear spin I must be half-integer. From the nuclear shell model for the atomic nucleus, the nuclear quantum number is found to be $I = 3/2$. This isotope is bosonic, taking into account the spin-1/2 nature of the unpaired valence electron. This valence electron fully defines the orbital and spin momenta of the low energy states. Its electron spin is $S = 1/2$, while its orbital angular momentum L varies as $L = \{0, 1, 2, ...\}$, which are assigned orbital letters $\{S, P, D, ...\}$ for historic reasons. The electronic ground state is an S-state with $L = 0$. The spin-orbit coupling results in a total angular momentum of $\mathbf{J} = \mathbf{L} + \mathbf{S}$, with a magnitude in

the range of $|L-S| \leq J \leq L+S$. For the S-state, $J = \{1/2\}$. In Paschen notation $^{2S+1}L_J$, this state reads $^2S_{1/2}$.

The first excited states are P-states with angular momentum $L = 1$, and therefore $J = \{1/2, 3/2\}$. Those two states are denoted $^2P_{1/2}$ and $^2P_{3/2}$, and the corresponding fine structure transitions are the D1 line ($^2S_{1/2} \rightarrow^2 P_{1/2}$ at 794.98 nm) and D2 line ($^2S_{1/2} \rightarrow^2 P_{3/2}$ at 780.24 nm). We will use the D2 line for ensemble preparation and also for the storage protocols. Its natural line width is $\Gamma = 2\pi{\cdot}6.1$ MHz.

Coupling of the electron's momentum to the nuclear momentum leads to the much weaker hyperfine structure. Those spins pair to the total atomic angular momentum $\mathbf{F} = \mathbf{J} + \mathbf{I}$, with a magnitude in the range of $|J-I| \leq F \leq J+I$. For the ground state, $F = \{1, 2\}$. This splitting corresponds to around 6.8 GHz. The first excited levels split accordingly, with $F = \{1, 2\}$ for $^2P_{1/2}$ and $F = \{0, 1, 2, 3\}$ for $^2P_{3/2}$. Each hyperfine level F contains $(2F + 1)$ magnetic sublevels $m_F = \{-F, -F+1, ...F\}$, with $F_z = \hbar m_F$. Those are usually degenerate, but split up in the presence of an external magnetic field. If the energy shift due to the field is small compared to the hyperfine splittings, F and m_F are "good quantum numbers" (and not so J, m_J and I, m_I). In this case, the level splitting is given by

$$\Delta E(F, m_F) = \mu_B g_F m_F B_z. \tag{3.1}$$

Here, μ_B is Bohr magneton, g_F the total angular momentum g-factor[1] and B_Z the z-component of the magnetic field, which is chosen as the quantisation axis. The relevant level scheme of the D2 line is shown in Fig. 3.2.

3.3 Magneto-optic trapping & cooling

Magneto-optical trapping is a standard technique to prepare cold clouds of atoms. Here, I intent to give a brief summary and refer the reader to the excellent text book by Foot [159] for further information.

[1] g_F itself is a function of F, I and J, so it will be different for the ground and excited state (as can be seen in Fig. 3.2).

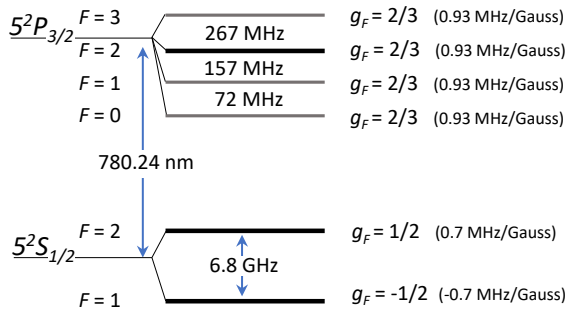

Figure 3.2: Schematics of the D2 line of Rubidium. Black: relevant levels for our storage protocols. Grey: Levels used for cloud preparation.

Optical molasses Trapping of hot, fast-moving atoms implies slowing them down first. Deceleration is achieved by interaction with a laser beam, counter-propagating to the atom's motion. For resonant light, the atom will absorb photons from the incoming light and experience a corresponding momentum transfer of $\hbar k = -m\delta v$ per photon. $k = 2\pi/\lambda_r$ is the wave vector of the photon, m the atomic mass, and δv the change in atom's velocity. The associated recoil velocity is $v_r = \hbar k/m$, which is around $6\,\mathrm{mm\,s^{-1}}$ for ^{87}Rb[2]. Photons are re-emitted spontaneously into all directions and do not on average change the atom's velocity. This results in a net force which slows the atoms down. As this technique relies on multiple scattering of the incoming light, one has to choose a cycling transition where the only dipole-allowed decay channel brings the atom back to the resonant level. For Rubidium, the $|F = 2\rangle \rightarrow |F' = 3\rangle$ transition on the D2 line fulfills this.

An atom that is moving at a velocity v experiences Doppler shift and will see the incoming light blue-shifted by $\delta\omega = kv$. Therefore, to address atoms that are moving towards the beam, the light has to be red detuned. The total detuning seen by the atom is $\delta = \omega - \omega_r + kv$, where ω_r is the resonance frequency. To slow down atoms moving in all directions, 3

[2]The recoil energy is defined as the kinetic energy of an atom moving at $v = v_r$, so $1/2mv_r^2 = \hbar w_{\mathrm{photon}}$.

pairs of counter-propagating lasers from all spatial directions are applied [3]. This light-induced damping is called *optical molasses*. For low velocities $vk \ll \Gamma$, this damping force is linear in velocity, and the force takes the form $F_{\text{molasses}} = -\alpha(\delta)v$. The velocity capture range is approximately given by $\pm\Gamma/k$. For the D2 line of ^{87}Rb, this amounts to $\approx \pm 5\,\text{m}\,\text{s}^{-1}$. For proper detuning, this force is able to cool atoms down to the *Doppler cooling limit*

$$T_D = \frac{\hbar\Gamma}{2k_B} \qquad (\,145\,\mu\text{K for } ^{87}\text{Rb}) \tag{3.2}$$

This is a result of the balance between directional absorption, steered by the Doppler effect, and heating due to random re-emission. To cool further, PG cooling can be applied, which relies on a delicate combination of a spatially-varying dipole potential (induced by a polarisation gradient of the trapping beams) and optical pumping [160]. The ultimate limit of cooling mechanisms involving spontaneous emission is the *recoil temperature*, which is the "temperature corresponding to an ensemble with a one-dimensional rms momentum of one photon recoil $\hbar k$." [158, p. 5]

$$T_r = \frac{\hbar^2 k^2}{m k_B} \qquad (361.9\,\text{nK for } ^{87}\text{Rb D2 line}) \tag{3.3}$$

Magneto-optical trapping The molasses force is *velocity-dependent* only. Exploiting the magnetic sub-structure of alkaline atoms, an additional *spatial dependence* can be introduced to trap them. To this end, the molasses is superimposed with a quadrupole magnetic field *gradient*, where the zero of the magnetic field coincides with the intersection of the light fields. Such a quadrupole field can be generated by a pair of round field coils in anti-Helmholtz configuration, for example Fig. 3.3(a). Atoms located off the center will see a magnetic field $B \neq 0$, leading to an energy splitting of their Zeeman sub-levels. For circularly polarised molasses beams and the correct choice of their helicities, this leads to a position-dependent force pushing the

[3] Conveniently, an atom moving away from a beam will see the co-propagating light further red-shifted, while the counter-propagating light is closer to resonance, leading to a net force that slows the atom down independent of its velocity vector.

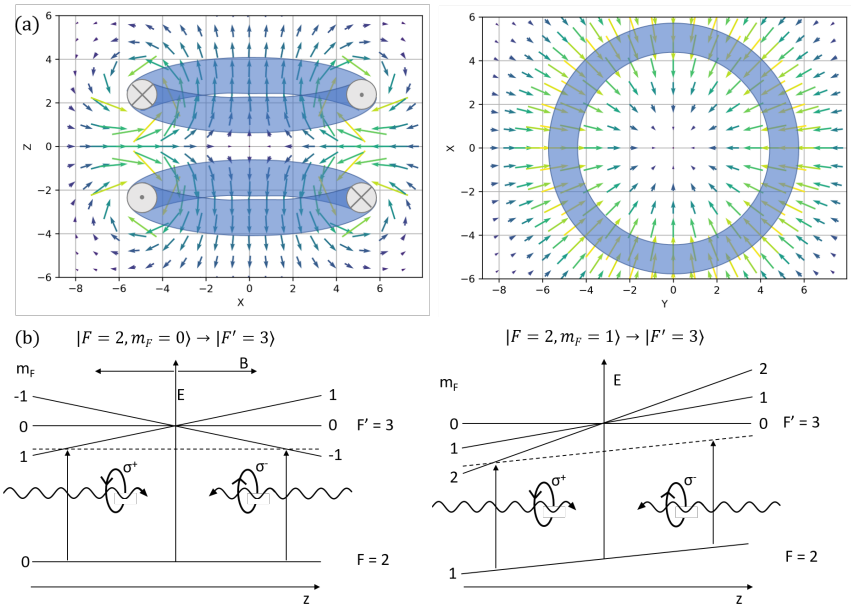

Figure 3.3: (a) B-field generated by a pair of circular coils in anti-Helmholtz configuration. Left panel: Slice along the (x,z) plane for y=0. Right panel: Slice along the (z,y) plane for z = 0. (b) Interaction of magnetic sublevels with circularly polarised light in the presence of a field gradient. Left panel: coupling of the magnetically insensitive $|F = 2, m_F = 0\rangle$ to the upper $|F' = 3\rangle$ manifold. Right panel: coupling of the field-sensitive $|F = 2, m_F = 1\rangle$. Note that ground and excited states shift with different magnitude. This means that for $m_F \neq 0$ the resonance condition for light incident from opposite directions is fullfilled at different distances from the trap center. Inspired by [159].

atoms towards the trap center. This can be illustrated, taking the cycling transition $|F = 2\rangle \rightarrow |F' = 3\rangle$ on the D2 line as an example. An atom with $m_F = 0$, located at $z < 0$, will see its $m_{F'} = 1$ level downshifted, see left panel of Fig. 3.3(b). It is then more likely to scatter σ^+-light incident from

the left then σ^--light incident from the right, pushing the atom towards the MOT center. This argument also holds true for atoms at $z > 0$ (inverting the role of the pumping beams and atomic levels), and for atoms initially prepared in any of the $(2F + 1) = 5$ Zeeman substates of $|F = 2\rangle$, as illustrated in the right panel of Fig. 3.3(b) for $m_F = 1$[4]. In summary, atoms are therefore slowed down when intersecting with the molasses beams and trapped in the zero of the magnetic field gradient.

3.4 Experimental apparatus

The setup was build in great parts by former PhD students Dr. Boris Albrecht and Dr. Pau Farrera, and by Dr. Matteo Cristiani, and described in their respective theses [161, 162]. Further developments that were implemented during my PhD, like improved noise filtering and the cavity enhancing light-matter interaction, are documented here.

3.4.1 Ensemble preparation

Laser system Two tunable diode lasers from Toptica (DL Pro & TA Pro) are employed to couple both the $|F = 1\rangle$ and $|F = 2\rangle$ states to the upper hyperfine manifold $|F' = \{0, 1, 2, 3\}\rangle$ of the D2 line. The DL Pro couples $|F = 1\rangle \to F'$ and outputs 50 mW. The stronger TA Pro used for trapping couples $|F = 2\rangle \to |F'\rangle$ and outputs 350 mW. The line width of both lasers is estimated to be around 200 kHz. The lasers are frequency-locked to an atomic reference via saturable absorption spectroscopy. To address the different $|F'\rangle$ transitions individually, AOM lines are used to shift the frequency. The light is then coupled into fibers and guided to the experimental chamber.

Experimental chamber The vacuum system consists of an octagonal quartz cell, anti-reflection coated for 700 to 1100 nm. The vacuum is main-

[4]While generally true, this argument cannot explain why some other species, for example Cesium with $|F = 4\rangle$, can be trapped with this technique. Optical Zeeman pumping also plays a role, as it induces a spatial distribution of the spin polarisation.

tained by an ion pump connected to the cell. ^{87}Rb is introduced directly to the experimental chamber via a dispenser unit. The pressure in the chamber is estimated to be around 10^{-9} mbar when the dispenser is running. The MOT is then loaded directly from background gas pressure.

Magneto-optical trap The circular MOT coils provide a field gradient of $20\,\mathrm{G\,cm^{-1}}$ along the coil axis and $10\,\mathrm{G\,cm^{-1}}$ in radial direction. The light intensity is $\approx 20\,\mathrm{mW\,cm^{-2}}$ per beam, which is 10 times the saturation intensity [158]. To re-trap atoms that decay to $|F = 1\rangle$, a weak repumping beam is present during trapping. The cloud size is on the order of 0.8x0.6x0.6 mm^3. The temperature reaches 30 µK after 1.5 ms of PG cooling. The maximum OD is between 5 and 10, depending on the transition.

3.4.2 Experiment layout & enhancement cavity

The general experimental layout is shown in Fig. 3.4. This setup was used throughout this thesis, with small modifications depending on the experiment. The main feature of the layout is a low-finesse ring cavity assembled around the vacuum chamber with the atomic cloud. It was designed to investigate the enhancement of the *writing* process in DLCZ, which lead to the experiment reported in [126], chapter 4. However, as we will see later, the design is more versatile: it also allows for enhanced Raman storage and the enhancement of DLCZ readout, see chapter 6.

We will review some important aspects of the design, starting with the cavity geometry. The cavity is a triangular ring cavity, consisting of two high-reflective mirrors and an outcoupling mirror with lower reflectivity. In this geometry, forward- and backward scattered write photons occupy different modes outside the cavity, whereas in a linear configuration write photons emitted into each of the two opposite directions occupy the same spatial mode [130]. The ring cavity therefore allows us to only collect forward-scattered photons with small spin wave vector, experiencing low motional decoherence [163].

The cavity is supposed to interact only with the write photon, for reasons detailed in chapter 4. As the read photon is emitted counterpropagating

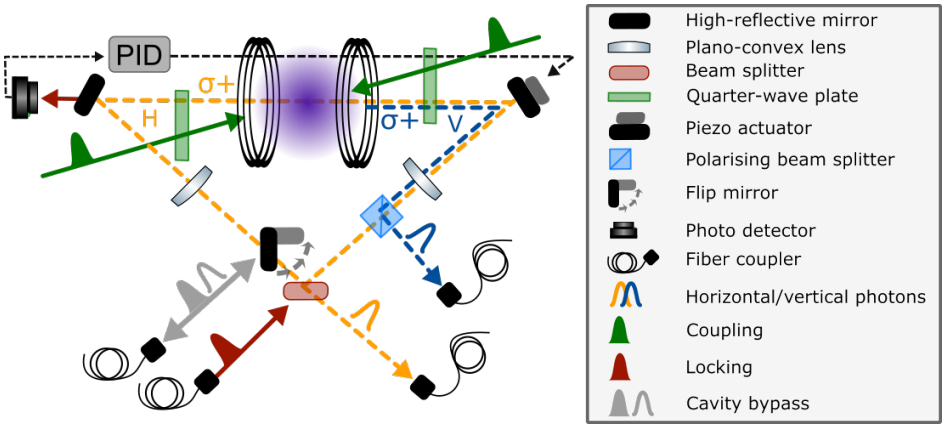

Figure 3.4: Layout of the experiment. The cavity is resonant only to horizontal light. Depending on the experiment, the cavity is active or blocked by a flip mirror. The Zeeman OP beam is not shown.

to the write photon, the only way to decouple it from the cavity is by polarisation. Therefore, the cavity is made to interact with the horizontal polarisation only, while the vertical polarisation is deflected on a PBS. The excitation scheme is then chosen such that the write and read photon polarisations fit. If the atoms shall be probed without cavity, the cavity can be bypassed by inserting a flip mirror into the beam path.

An important design parameter is the cavity finesse F. Finesse is defined as the ratio of free spectral range (FSR), $\Delta\nu_{\mathrm{FSR}} = c/(nl)$, by the cavity linewidth, $\Delta\nu_{\mathrm{c}}$. It is related to the cavity roundtrips of light inside the cavity, $F/(2\pi)$. For this cavity, with one outcoupling mirror of reflectivity $R = 1 - T$, and roundtrip losses L ($\approx 11\%$), the finesse reads

$$F = \frac{\Delta\nu_{\mathrm{FSR}}}{\Delta\nu_{\mathrm{c}}} \approx \pi \frac{(R(1-L))^{1/4}}{1-(R(1-L))^{1/2}} \tag{3.4}$$

A high reflectivity R increases the finesse of the cavity, at the expense of decreased photon escape efficiency $\eta_{cav} = T/(T+L)$. As a compromise, we chose a reflectivity of 86% (for H-polarisation), corresponding to a

measured cavity finesse of 22.2 and a calculated photon escape efficiency of 56%. Considering that Rubidium deposition on the MOT chamber windows already accounts for $\approx 70\%$ of these losses, implementing the cavity inside the vacuum chamber could greatly improve the memory performance.

Due to technical considerations such as the geometry of the vacuum chamber setup and spatial filtering of write and read pulses, we choose a cavity length of $L \approx 88\,\mathrm{cm}$. This leads to a FSR of 342 MHz, corresponding to a cavity transmission linewidth of 15.4 MHz.

Two plano-convex lenses ($f = 300\,\mathrm{mm}$) focus the mode onto the atomic cloud. The beam waist is 69 µm ($1/e^2$ beam radius) at the cloud position. Two coupling beams address the atomic cloud, intersecting at a small angle $< 3^\circ$ with the cavity mode (180 µm $1/e^2$ beam radius). Before interacting with the atoms, both coupling beams and the cavity mode are transformed to circular polarisation by means of quarter-wave plates. The light polarisation then corresponds to $\sigma^{\pm}$- transitions in the atomic reference frame defined by a homogeneous B-field applied in the direction of the cavity mode.

The cavity length is actively stabilized by injecting lock light and monitoring the leaked transmission through one of the cavity mirrors. A side-of-fringe lock maintains the resonance condition by feeding back to a piezo-electric actuator attached to the second cavity mirror. A chopped lock is used to iterate between locking (during MOT loading) and photon detection (during interrogation), thereby avoiding strong lock light from reaching the detector. During interrogation, when no locking feedback can be derived, the cavity is passively stable.

3.4.3 Noise filtering

In both protocols investigated in this thesis, strong coupling pulses are used to either generate correlated photon pairs or to map them in and out of the memory. The difference in frequency between photons and pulses equals the ground state splitting of 6.8 GHz. Additionally, in the case of the DLCZ memory, spontaneously scattered photons to the second hyperfine manifold introduce wrong heraldings, as those spin waves can not be retrieved later. To this end, a filter cavity had been implemented previously, following a

Parameter	**New design (measured)**	New design (theoretical)	Old design (mixed)
FSR (GHz)	–	16.2	13.4
Finesse	**232**	252	255
FWHM (MHz)	**70**	64.7	52.5
Transmission (Cavity only) (%)	**93.8**	93.4	50
Transmission (fiber-to-fiber) (%)	**58 (52.5)***	—	15-17
Suppression (@ 6.8 GHz detuning) (dB)	**-43.5 (-43)***	-44.15	-43.5
Tunability (GHz/K)	**2.6**	2.84	3.1
dT/FWHM (mK)	**26**	25	17
Birefringence (1/FWHM)	**0.1**	—	1.2

Table 3.1: Performance comparison of the old & new filter design. Quoted values are measured for the cavity with best performance. (*) values for the second cavity, in case they differ.

design reported in [164]. A high-reflection coating was applied to both sides of a plano-convex lens, which served as the cavity. The lens was fitted into a copper block. The resonance was temperature-tuned and the temperature was stabilized, avoiding the overhead of locking on an optical reference. The noise suppression at 6.8 GHz from resonance was −44 dB. But those filters had a limited fiber-to-fiber transmission of around 15 to 17 %, including a fiber mating sleeve, cavity transmission (55%), fiber incoupling (50%) and losses on optical surfaces. Improving this transmission was crucial, especially for correlation measurements where the coincidence rate depends on the multiplication of the individual photon detection probabilities. The filters were therefore redesigned.

Cavity transmission can be limited for various reasons: mode mismatch when coupling to the cavity, losses (scattering & absorption on mirror surfaces or in the host material), distortion of the wavefront (upon reflection on the mirror surfaces or in the medium) or mismatch in reflectivity for the

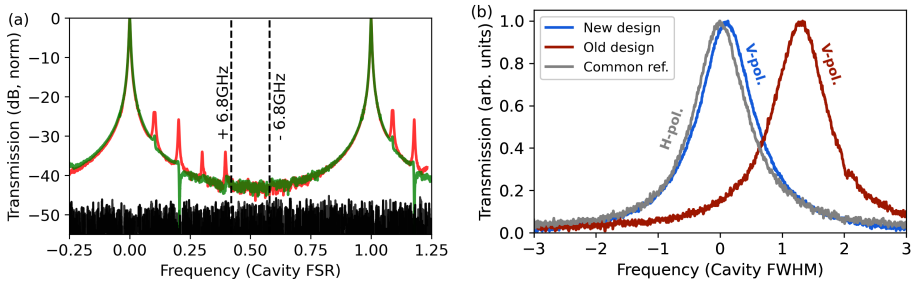

Figure 3.5: (a) Normalized transmission spectrum of the two filters, in green and red. Black: noise floor of the photo diode. Two vertical lines at ± 6.8 GHz indicate the frequency of the light that should be filtered out. (b) Polarisation birefringence, comparing the old and new design. Upon a change of input polarisation from horizontal to vertical, the spectrum of the new design is almost not affected. The common horizontal axis is re-scaled to units of the cavity FSR or FWHM, respectively.

incoupling & outcoupling path (so-called impedance mismatch). A more thorough study of the old cavities was performed to identify the limitations of the design, see appendix A.2. We concluded that a makeover of the design could considerably improve performance.

The main difference is the change of host material from BK-7 glass to a high-quality fused silica glass. Silica shows less material absorption. It can also be manufactured with higher optical purity, isotropy, homogeneity and lower material defects as compared to BK-7. Additionally, extra care was taken to achieve low surface roughness and surface form defects. The coating was optimized for internal reflection. Also, the holder was redesigned to improve thermal contact and stability.

The performance of the new design is listed in table Table 3.1. The measured values are in good agreement with the design values. A transmission spectrum of the write and read photon filter is displayed in Fig. 3.5(a). Other than improved transmission, this cavity shows almost no birefringence, see Fig. 3.5(b). Therefore, no polarisation control is needed. Given the

new fiber-to-fiber transmission of 52% and 58% (instead of 15% and 17%), the rate in an hypothetical cross-correlation measurement improves from $p_{12} \propto \eta^2_{\text{trans,old}} = 0.025$ to around $\eta^2_{\text{trans,new}} = 0.3$, representing a 10-fold increase.

3.5 Memory characterisation & optimisation

3.5.1 Assessing non-classical photon statistics through correlation functions

To measure the properties of photons from probabilistic pair photon sources like the DLCZ memory, normalized intensity correlation functions are useful. The cross-correlation between the write and read photon fields is defined as

$$g^{(2)}_{wr} := \frac{\langle a^+_w a^+_r a_w a_r \rangle}{\langle a^+_w a_w \rangle \langle a^+_r a_r \rangle} = \frac{p_{wr}}{p_w\, p_r}. \tag{3.5}$$

Here, we have introduced the creation and annihilation operators a^+ and a. p_w and p_r are the probabilities to detect a write or read photon within their respective detection window in each generation attempt. p_{wr} is the probability to detect a coincidence click between the two fields per attempt. For the two-mode squeezed state eq. 2.8, eq. 3.5 yields $g^{(2)}_{wr} = 1 + 1/p$. $g^{(2)}_{wr}$ is larger than 2 for any $p < 1$. High values of $g^{(2)}_{wr}$ are also related with a high fidelity of the entangled states in a QR architecture [165].

In a similar way, intensity auto-correlations are defined for a single photon mode (either the write or the read mode). They can be measured by splitting the mode on a beam splitter and correlating the two outputs 1 and 2, effectively performing a Hanbury Brown-Twiss (HBT) measurement. For the write field, this would be $g^{(2)}_{ww} = p_{w1,w2,}/(p_{w1}\, p_{w2})$. Those unconditional auto-correlations give $g^{(2)}_{ww} = g^{(2)}_{rr} = 2$, the same as for classical thermal light. Only when post-selecting on a heralding click from either the write or the read field, for example $g^{(2)}_{rr|w} = p_{rr|w}/(p_{r1|w}\, p_{r2|w})$ for heralding on the write field, the second field will show non-classical antibunching. For a true single

photon, we expect $g^{(2)}_{rr|w} = 0$. It can be shown that $g^{(2)}_{rr|w} = g^{(2)}_{ww|r} = 4p$ for $p \ll 1$, which tends to zero for $p \to 0$.

For two classical fields E_1 and E_2, the Cauchy-Schwarz inequality holds [166]

$$g^{(2)}_{12} < \sqrt{g^{(2)}_{11} g^{(2)}_{22}}. \tag{3.6}$$

In the case of DLCZ, this is violated for any $p < 1$, indicating that the two fields are non-classically correlated.

3.5.2 The DLCZ memory

In this study, the memory is studied with and without the above-mentioned filter cavities, by either not filtering at all, inserting a filtering cavity on the write photon path or inserting a filter cavity in both paths. The enhancement cavity was bypassed. This study is instructive to get an intuition of the memory operation and illustrates the performance of the new filters.

The relevant level scheme is sketched in Fig. 3.6(a). After loading the atoms in the MOT, the memory is prepared in $|g\rangle = |F = 2, m_F = 2\rangle$ by optical pumping in the presence of a homogeneous field in the direction of the photon mode. Subsequently, a write pulse is sent to the memory every 1.5 µs. If a write photon detection heralds the presence of an atomic excitation on $|s\rangle$, the excitation is stored for 1.5 µs before it is retrieved as a read photon by an on-resonant read pulse. If no write photon was detected, the optical pumping pulses reset the atomic population to $|g\rangle$, before a new trial is performed. Around 1000 write attempts are performed before the atoms are re-loaded. The collection efficiency of the read photon into fiber is estimated to be around 82%, by injecting laser light through the write photon coupler and measuring the fiber-coupling efficiency [5]. The angle between write pulse and forward-scattered collection mode is $\approx 2.5°$. Write and read photon detector efficiencies are 45% and 41%, respectively.

The circularly-polarised write pulse couples off-resonantly to the excited state $|e\rangle = |F' = 2, m_{F'} = 1\rangle$, driving a σ^- transition ($\Delta = -40$ MHz). We

[5] This is an upper bound for the single-photon collection efficiency, as the spatial mode of the emitted read photon might differ.

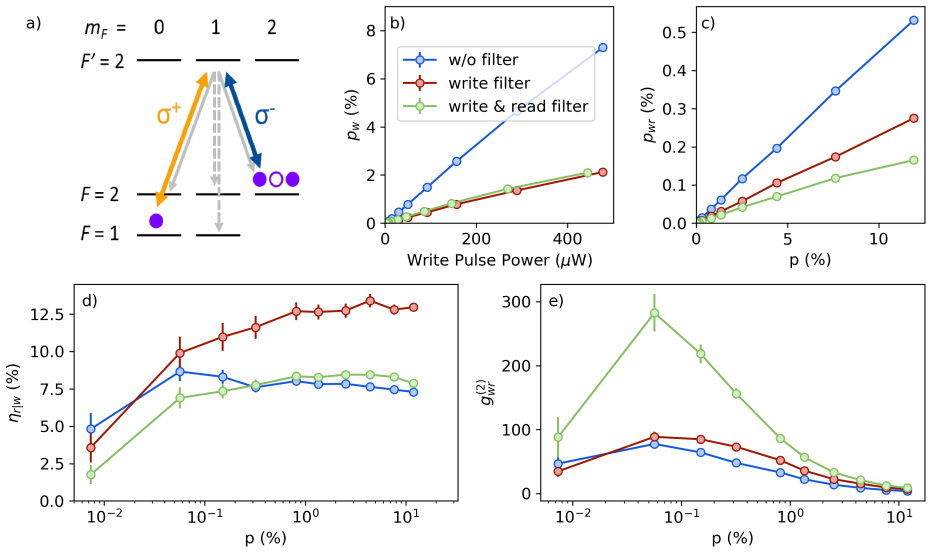

Figure 3.6: Level scheme and characterisation of the DLCZ memory as a function of excitation power and probability p. (a) Relevant Λ-level scheme (in blue and yellow) and additional decay channels (in gray). Only σ-transitions are allowed along the quantization axis. (b) Writing probability p_w versus write pulse power. (c), (d), (e) Unconditional coincidence probability p_{wr}, conditional coincidence probability $\eta_{r|w}$ and cross-correlation $g^{(2)}_{wr}$ versus generation probability p of a spin wave on $|s\rangle$. The writing pulse duration is 30 ns. All quantities are detected.

are interested in σ^+-light scattered on the $|e\rangle \rightarrow |s\rangle = |F = 1, m_F = 0\rangle$ transition, which heralds the spin wave creation upon detection of a write photon. There exist different decay paths for the spontaneously scattered write photons, as shown in Fig. 3.6(a). π-transitions are not driven along the quantisation axis, and a polarisation filter (PBS) eliminates light corresponding to σ^-- transitions. However, σ^+-decay to the hyperfine groundstate $|F = 2, m_F = 0\rangle$ occurs, heralding a false spin wave that can not be retrieved later on. The write filter cavity is inserted to filter those photons.

Panel (b) shows the write photon detection probability as a function of the excitation pulse power. This probability is linear in power. The probability for detection with filter is reduced by the filter transmission (55%). Additionally, it filters decay to the unwanted state $|F = 2, m_F = 0\rangle$, quantified by the branching ratio (50%). The overall detection is therefore reduced to around 28%, compared to the case without filter.

After writing, the memory is read out by the read pulse. The coincidence probability p_{wr} of detecting a write and read photon in the same trial increases linearly with p. This is shown in panel (c). With the filters, p_{wr} is reduced by the filter losses on both photon arms. However, the elimination of false heralds leads to an increase in conditional coincidence probability $\eta_{r|w} = p_{wr}/p_w$, as shown in panel (d)[6]. The filtering also improves the cross-correlation $g^{(2)}_{wr}$, as assessed by measuring $g^{(2)}_{wr} = p_{wr}/(p_w p_r)$ in panel (e). For small p, $g^{(2)}_{wr}$ and $\eta_{r|w}$ are limited by detector dark counts.

3.5.3 The Raman memory

The memory can also be operated as a write-in Raman memory. This is exemplarily demonstrated in Fig. 3.7(a) for weak light, but the protocol works the same for light on the single-photon level. For this data, the same setup and Λ-scheme as in the former subsection is used. The filter cavities is not needed, and the enhancement cavity is bypassed. The ensemble is prepared in $|g\rangle = |F = 2, m_F = 2\rangle$. An input probe couples off-resonantly to $|e\rangle = |F' = 2, m_{F'} = 1\rangle$ ($\Delta = -60\,\mathrm{MHz}$, 220 ns pulse duration (FWHM)) and is mapped to the second ground state $|s\rangle = |F = 1, m_F = 0\rangle$ by means of a strong coupling pulse in two-photon resonance with the probe (240 ns pulse duration). After a programmable delay, a rectangular co-propagating coupling pulse retrieves the stored excitation in forward direction. Under these conditions, the total storage and retrieval efficiency was measured to be around 21%.

[6] It is pure coincidence that the green and blue curves in panel (d) almost overlap. The increase in $\eta_{r|w}$ due to the filtering of false heralds by the write photon filter is compensated by the additional losses introduced by the read photon filter.

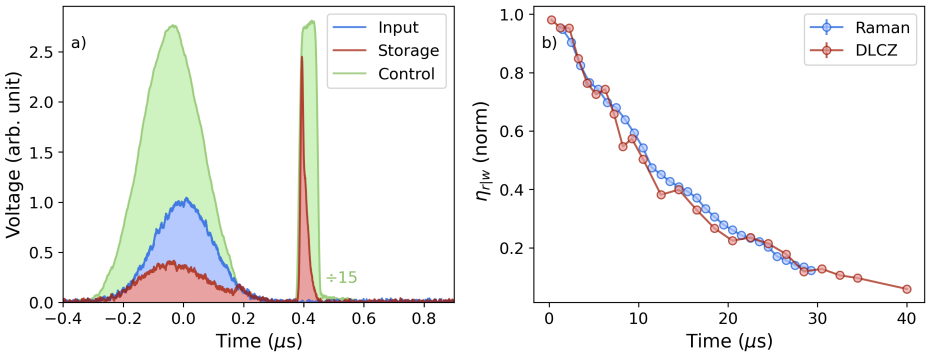

Figure 3.7: Characterisation of the Raman memory with weak classical light. (a) Storage and retrieval process. At $t = 0$, the input pulse (blue) is stored in the memory by simultaneously sending a coupling pulse tuned into two-photon resonance with the probe (green). After 400 ns, a second control pulse (green) retrieves the excitation (red). The second coupling pulse was scaled to aid visualisation. (b) Normalized retrieval efficiency as a function of storage time, for Raman and DLCZ storage under similar conditions.

As the memory absorbs a weak input pulse containing many photons, the trace in Fig. 3.7(a) can be recorded in a single shot on an avalanche photo diode. Raman storage of classical light is therefore a powerful tool for parameter optimisation which is otherwise very time consuming. This includes the alignment of beams, optimisation of optical pumping and optimisation of magnetic fields. Also, the wave vector of the spin wave generated in the Raman storage process has the same magnitude (although opposite direction) as the one in the DLCZ writing process. It is therefore expected that the de- and rephasing mechanisms equally affect both protocols. Fig. 3.7(b) demonstrates this. Here, the retrieval efficiency is measured as a function of storage time, for both Raman and DLCZ under similar conditions. Indeed, the decay is very similar for both. In this measurement the lifetime is comparably short, as no PG cooling is applied and the angle of 2.5° between probe mode and coupling mode makes it susceptible to motional dephasing.

Chapter 4

A cold atom temporally multiplexed quantum memory with cavity-enhanced noise suppression

This experiment is to be seen as an extension of [146], which demonstrated storage of two temporal modes on our setup. When I joined this experiment for my master's thesis, I integrated the enhancement cavity around the atoms, required for low-noise multimode storage. This also involved significant experimental effort towards improving the mechanical stability of the whole setup, which finally allowed me to perform this experiment during my subsequent PhD. Another major challenge was posed by magnetic-field fluctuations, requiring careful field compensation and calibration. The experimental results in this chapter are published in [126], and the text is adapted from the publication. The published manuscript was prepared by Dr. Pau Farrera and Prof. Hugues de Riedmatten, while I performed the experiment, contributed to the figures and prepared the supplemental material.

4.1 Introduction

As explained in chapter 1, subsection 1.2.4, for repeaters based on probabilistic sources, the generation probability p_{gen} is kept small in order to suppress the emission of multiphoton components. Additionally, the memory node has to wait for a heralding signal from the central station, indicating a successful heralding event with probability p_{her}, before executing the next trial. As p_{gen} is intrinsically limited, the only way to increase the heralding rate $R \propto p_{\text{gen}} \times 1/\tau_{\text{com}}$ is to perform more attempts within the communication time. For this, a resource-efficient way is the implementation of multi-mode memories, capable of holding many distinguishable entangled states simultaneously and reading them out selectively. The rate then scales linearly with the number of modes N stored in memory, as long as $Np_{\text{her}} \ll 1$.

Different degrees of freedom have been considered for the multiplexed modes, such as frequency, space or time. Ensemble-based platforms are well suited for demonstrating quantum information multiplexing. Current multimode atomic memories focus mainly on spatial multiplexing, e.g. addressing modes with different wave vectors or multiple memory cells in different parts of the cloud [70, 71, 137, 167–169]. Beyond spatial multiplexing, time multiplexing provides a practical way to store multiple distinguishable modes in the same ensemble of atoms. So far, time multiplexing has been mostly studied in solid-state quantum memories based on inhomogenesously broadened rare-earth doped crystals, using the atomic frequency comb scheme [18, 45, 170–178]. In contrast, very few experiments have investigated time multiplexing in atomic gases either by using a controlled and reversible broadening of the spin transition [53, 146, 151, 179] or more recently by mapping photons generated in different spatial modes to different temporal modes [180, 181].

In this work, we show a temporally multiplexed DLCZ-type quantum memory. Different temporal modes can be made distinguishable by combining the native DLCZ protocol with a rephasing protocol based on photon echo (DLCZ-CRIB, see below). However, previous attempts to generate nonclassically correlated pairs of photons and spin waves in multiple temporal modes in the same spatial mode have been plagued by a linear increase of

the noise as a function of number of modes due to dephased spin waves [146]. This effect prevents significant gain in photon pair generation rate, compared to the single-mode case.

Following a proposal by Simon *et al.* [182], and building on the work of [146], we demonstrate that by embedding the ensemble into a low-finesse cavity, one can substantially reduce noise from dephased spin waves. We experimentally show noise reduction by a factor 14. Subsequently, we demonstrate the generation of cavity-enhanced photons paired with spin waves in up to 10 temporal modes while preserving high quantum correlations between the photons and spin waves. This allows us to increase the spin wave - photon (photon pair) creation rate by a factor 10 (7.3), with respect to the single-mode case. The number of modes could be greatly improved by increasing the finesse of the cavity.

4.2 Operation principle & experimental setup

The operational principle of the memory is shown in Fig. 4.1. We cool an ensemble of ^{87}Rb atoms in a magneto-optical trap to a temperature of around 40 μK. The relevant atomic levels are shown in Fig. 4.1(a) and consist of two metastable ground states ($|g\rangle = |5^2S_{1/2}, F = 1, m_F = 1\rangle$ and $|s\rangle = |5^2S_{1/2}, F = 2, m_F = 1\rangle$) and one excited state ($|e\rangle = |5^2P_{3/2}, F = 2, m_F = 2\rangle$). After optically pumping the atoms to $|g\rangle$ in the presence of a homogeneous bias field, a write pulse drives the transition $|g\rangle \rightarrow |e\rangle$ red-detuned by $\Delta = -40$MHz. This process probabilistically generates write photons on the $|e\rangle \rightarrow |s\rangle$ transition through spontaneous Raman scattering that are paired with collective spin excitations (atoms in $|s\rangle$). The $|g\rangle \rightarrow |s\rangle$ transition is magnetic-field sensitive, with $\Delta\omega/\mathrm{B} = 0.7 - (-0.7)$ MHz/G $=$ 1.4 MHz/G. This field-sensitivity is exploited to engineer an inhomogeneous broadening of the ensemble. As we will see now, the **C**ontrolled **R**ephasing of this **I**nhomogeneous **B**roadening (CRIB) will allow for multi-mode storage.

During writing, a spatial gradient magnetic field is present. This causes a position dependent energy shift of the atomic levels through the Zeeman

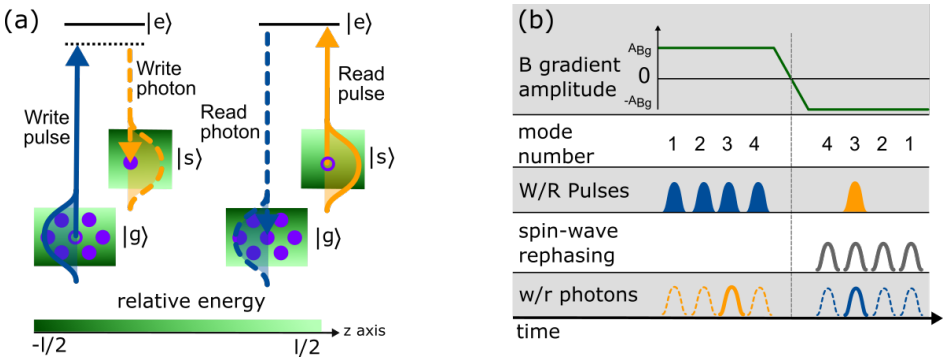

Figure 4.1: (a) Energy levels relevant for the photon generation process. The green color gradient bars illustrate the position dependent Zeeman level energy shift along the z-axis. (b) Time diagram of events occurring in the temporally multiplexed operation of the system. In this example, 4 write pulse modes are sent to the atomic cloud. A magnetic field gradient of amplitude A_{Bg} is present which is reversed to $-A_{Bg}$ after the last write pulse mode. If a write photon is detected in the 3rd mode, a feed forward instruction sends the read pulse at the time corresponding to the 3rd-mode spin wave rephasing time.

effect. The temporal evolution of the spin waves can be written as

$$|\Psi_a(t)\rangle = \frac{1}{\sqrt{N}} \sum_{j=1}^{N} e^{i\mathbf{x}_j(\mathbf{k}_W - \mathbf{k}_w) + i\int_0^t \Delta w_j(t')dt'} |g_1 ... s_j ... g_N\rangle \qquad (4.1)$$

where the two-photon detuning Δw_j is different for each atom. Here, N denotes the total number of atoms, $\mathbf{x}_j$ the initial atom position and $\mathbf{k}_{W(w)}$ the wavevector of the write pulse (photon). $\Delta w_j = \mu_B B(x_j)(g_{F(|s\rangle)} m_{F(|s\rangle)} - g_{F(|g\rangle)} m_{F(|g\rangle)})/\hbar$ where μ_B is the Bohr magneton, $B(x_j)$ is the magnetic field at the position of atom j, $g_{F(|s,g\rangle)}$ is the Landé g-factor, and $m_{F(|s,g\rangle)}$ the quantum number corresponding to the z-component of the total angular momentum. The gradient field is provided by the trapping coils.

The collective atomic excitation can be converted into a read photon by

means of a read pulse resonant to the $|s\rangle \rightarrow |e\rangle$ transition. In the absence of atomic dephasing the emission will be highly efficient into a particular spatio-temporal mode thanks to collective interference of all contributing atoms. In the case of spin wave dephasing, i.e. like the one induced by the magnetic field gradient, no collective interference occurs and the read-out process will not be efficient. However, inverting the amplitude of the magnetic field gradient (and thereby inverting the phase evolution of the spin wave) eventually leads to its rephasing and efficient photon retrieval. This technique can be used to write N_m different temporal modes and select a particular one to be read-out (see Fig. 4.1b).

Note that while we can trigger the phase reversal on demand, there will be a delay between this trigger and the actual read-out. If the time between mode storage and field reversal is τ, this mode rephases only after 2τ. In an actual repeater link, the gradient can only be reversed upon arrival of a herald from the intermediate measurement station. This delay does not prevent however the use of our memory in a quantum repeater architecture, as the retrieval is still on-demand. In order to minimize the rephasing delay, the magnetic field gradient can be nulled after the last mode was stored in the memory. Doing so, the dephasing will be stopped and the atomic phase frozen. Upon an heralding signal, the gradient can be reversed and the spin-wave modes will start to rephase immediately. Such a broadening could also be introduced with light, based on the AC Stark shift. In this case, a magnetic-field insensitive transition could be used.

When reading a particular temporal mode, noise arises from dephased spin waves generated in other temporal modes. During writing, spin waves are created which are paired with photons emitted into all possible modes, not only the write photon mode. Such spin waves, if in phase, emit read photons into the corresponding phase matched (uncollected) mode and therefore do not contribute to read-out noise. However, in CRIB, the $N_m - 1$ dephased spin waves will emit read photons into all directions and therefore generate noise in the read mode [182]. Non-perfect rephasing of the read-out mode adds additional noise proportional to $1 - p_{r|w}^{\text{int}}$, where $p_{r|w}^{\text{int}}$ is the intrinsic read-out efficiency. We obtain the following expression for the total probability to detect a noise photon from dephased spin waves (see

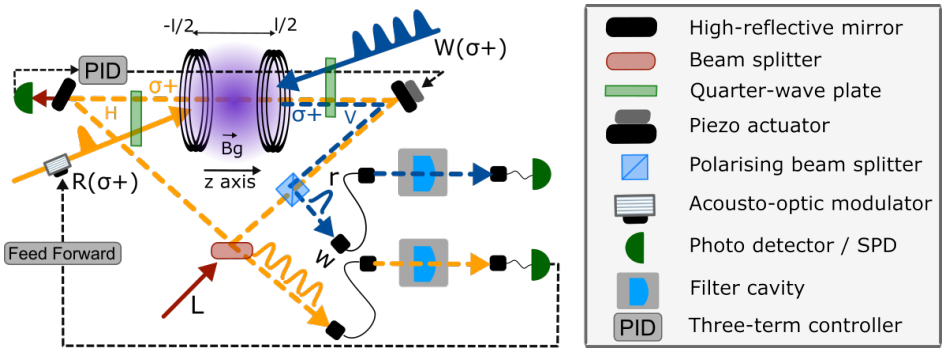

Figure 4.2: Schematic overview of the experimental setup. W, write pulse; R, read pulse; w, write photon; r, read photon; L, cavity locking laser beam. The polarizations indicated are in the atomic frame.

appendix B.2)

$$p_{r|w}^{\text{noise}} = p(N_{\text{m}} - p_{r|w}^{\text{int}})\frac{\beta_r}{\beta_w}\xi_{eg}\eta_r. \tag{4.2}$$

Here, p is the probability to generate a spin wave - write photon pair, $\beta_{w(r)}$ is the fraction of write (read) photons that are emitted into the collected spatial mode, ξ_{eg} is the branching ratio corresponding to the $|e\rangle - |g\rangle$ transition, and η_r is the detection efficiency of the read photons. In order to decrease this noise one can increase the ratio β_w of excitations paired with write photons over excitations paired with photons emitted into other spatial modes. This is achieved with an optical cavity enhancing the photon emission into the write photon spatial mode. Our cavity is schematically depicted in Fig. 4.2. In order to not simultaneously increase β_r while increasing β_w, the read photon has orthogonal polarization from the cavity mode and is decoupled from the cavity by a PBS.

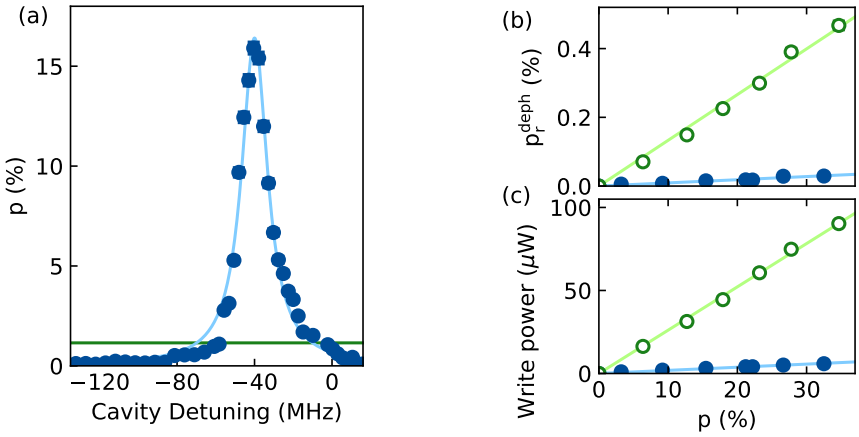

Figure 4.3: (a) Write photon emission probability as a function of the cavity resonance frequency. Frequency zero corresponds to the center of the $|e\rangle - |s\rangle$ transition. The green solid line represents the emission without cavity enhancement. (b) Read photon detection probability from dephased spin waves and (c) write pulse power as a function of the spin wave excitation probability. The spin wave is read out after 1.2μs of storage time. This time is much longer than the spin wave dephasing time set by the B field gradient [146]. Blue (green) data is taken with (without) cavity enhancement.

4.3 Results

First, we confirm that the cavity enhances the write photon emission into the cavity mode, Fig. 4.3(a). We use a write pulse with duration $\Delta t_W = 266\,\text{ns}$, which is a compromise between the finite cavity line width and the finite spin wave rephasing bandwidth. In appendix B.1, those two effects are described and analysed more in-depth.

The cavity resonance frequency is changed by moving one of the cavity mirrors with a piezo-electric device. When the cavity resonance matches the write photon transition, photon emission is enhanced. However, when the frequencies differ by more than the cavity linewidth, the emission is

suppressed. At resonance we observe enhancement of $p^c_{\mathrm{enh}}/p = 14.3(6)$. Here, p^c (p) is the write photon emission probability with (without) cavity. This is close to the expected value of $2F/\pi$ [183], while out of resonance inhibition is $p^c_{\mathrm{inh}}/p = 0.078(3)$. The spectral width of the emission is 16.6MHz, matching the cavity linewidth. Note that the effective enhancement of the write photon detection probability is reduced by the cavity escape efficiency, which for our implementation is 56%.

As mentioned before, the cavity enhancement of the write process allows for suppression of the read photon noise generated from dephased excitations. This is quantified in Fig. 4.3(b) and 4.3(c). In order to measure this dephased noise, a magnetic field gradient is applied during writing without field inversion before read-out. This causes a rapid dephasing of the generated spin waves and hence all the read-out photons are generated through interaction of the read pulse with dephased spin waves. In Fig. 4.3(b) (4.3(c)), the read photon detection probability (write pulse power) is shown as a function of the write photon generation probability p. We observe that for the same excitation probability, the noise (write pulse power) is 14.4(7) (13.9(3)) times lower in the cavity enhanced situation. This is compatible with the cavity enhancement observed in Fig. 4.3(a). The enhancement gives an approximate upper bound on the number of modes that can be multiplexed.

After characterizing cavity-enhanced emission and noise reduction, we now compare temporally multiplexed storage with and without enhancement, as depicted in Fig. 4.1(b). Fig. 4.4 shows a situation in which 6 write pulse modes are sent to the atomic cloud. In Fig. 4.4(a), after the 6-modes write process, the magnetic field gradient is reversed. Upon detection of a write photon, we use a feed forward instruction in order to scan the read-out around the expected rephasing time. We observe 6 peaks corresponding to the rephasing of each of the 6 spin wave modes. This figure shows 6 different data sets (separated through white and grey backgrounds) corresponding to write photon detection in different temporal modes. The ratio between the SNR achieved with/without cavity enhancement of ≈ 14 highlights the noise reduction achieved with cavity.

The 1/e memory lifetime in native DLCZ is measured to be $\tau \approx 72\mu s$, limited by atomic motion and small uncompensated gradient fields. The

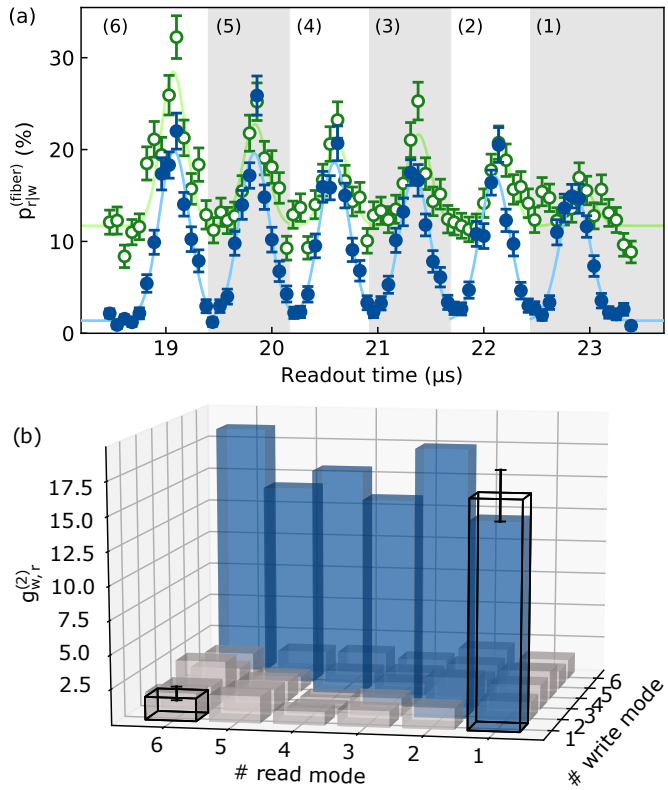

Figure 4.4: (a) Probability to collect an heralded read photon into the read fiber as a function of the read-out time for 6 different temporal modes. Time zero corresponds to time of writing of the last write mode (6). With cavity enhancement, intrinsic retrieval efficiency for the first mode is $p_{r|w}^{int} \approx 26\%$. Blue (green) data is taken with (without) cavity enhancement. For both, single-mode excitation probability is $p_{1m} \approx 0.04$. Solid lines are a Gaussian fit of each retrieval peak. (b) Individual cross-correlation function between the different 6 write and read modes with cavity. The two bars in solid black lines at positions (1,1) and (1,6) represent the average for the diagonal and the off-diagonal values, respectively.

retrieval efficiency in Fig. 4.4(a), however, decays quicker. This is because of additional (slowly varying) gradient fields present in the rephasing protocol which can not be compensated. This introduces decoherence according to eq. 2.17. Furthermore, the magnitude of the gradient applied by the MOT coils is subject to small jitters, leading to varying rephasing times across one experimental cycle. To counteract, we use a high voltage capacitor enabling a fast and stable field reversal. However, this does not allow for removing this gradient drift completely.

For the cavity case, Fig. 4.4(b) characterizes the cross-correlation function between the write and read photons (defined as $g^{(2)}_{w,r} = p_{w,r}/(p_w p_r)$, where $p_{w,r}$ is the probability to detect a coincidence between write and read photon, and $p_w(p_r)$ is the probability to detect a write (read) photon) in all the 36 possible combinations of six write and six read modes. The correlations are preserved when the read mode corresponds to the write mode (weighted average 16.6(1.8)). However, no crosstalk is observed when the read mode is different from the considered write mode (weighted average 1.7(0.5)).

Finally, we characterize the cavity enhanced temporally multiplexed operation of the system. After a train of N_m write pulses and the recording of a write photon, the magnetic field gradient is inverted. A read pulse is sent at the expected rephasing time of its paired spin excitation. In Fig. 4.5(a), scanning the number of modes, we observe that the write photon detection probability per write pulse train, and hence the probability to create a spin wave - photon pair, increases linearly with N_m, while the write-read photon coincidence detection probability has a slightly worse scaling. This can be explained by the reduced readout efficiency as a function of storage time, mainly induced by the above-mentioned magnetic field fluctuations.

Nevertheless, for 10 modes we obtain a total rate enhancement of 7.3. In Fig. 4.5(b), again scanning N_m, we show the averaged value of $g^{(2)}_{w,r}$ across N_m modes. We notice that the multiplexed operation degrades the correlations between the write and read photons much stronger in the absence of the cavity. The cavity significantly reduces the impact of the dephased spin waves on the quality of the correlations. It is also remarkable that $g^{(2)}_{w,r}$ is higher with cavity enhancement in the case of just 1 temporal mode. This is

predicted by Eq. 4.2 for read out efficiencies <1 ($\eta_{r|w} < 1$ implies imperfect rephasing of the spin wave which in turn leads to noise in the readout) and analysed in more detail appendix B.4. Moreover, the values $g^{(2)}_{w,r} > 2$ are an evidence of quantum correlation between the write and read photons, assuming thermal statistics for the individual write and read modes. For 10 modes, we also measured the averaged heralded autocorrelation of the generated single photon and found $g^{(2)}_{r,r|w}$=0.36(0.25)< 1, confirming the non-classical nature of the emitted photons.

4.4 Discussion

The maximal number of temporal modes is currently limited by the finesse of our cavity, which is in turn limited by the optical intra-cavity loss, mostly given by the windows of our vacuum chamber. This loss is also responsible for the low escape efficiency in our current experiment. This is however not a fundamental limitation. By implementing a cavity inside the vacuum chamber, a much higher cavity finesse could be achieved while keeping a high escape efficiency, such that $N_m > 100$ should be readily possible. For such a large number of modes, the next limitation is the spin wave storage time. With write modes separated by 800 ns as in our implementation, memory lifetimes of $2 * 80\mu s$ become necessary. However, DLCZ experiments with cold atoms in optical lattices have shown much longer storage times of up to 450 ms [65, 147, 184]. Reaching long storage times is facilitated by the use of magnetically insensitive transitions to minimize decoherence by magnetic fluctuations. These transitions are not directly compatible with the broadening using magnetic gradients as demonstrated in our current proof of principle experiment. However, several solutions could be applied, e.g. transferring the excitations to clock transitions after the write pulse train [148] or using light shifts for inducing and reversing the broadening [185, 186]. Finally, we note that the gain in coincidence count rate due to the multi-mode operation is only present for a fixed repetition rate of the experiment. This is for example the case for quantum repeater applications, where entanglement between distant quantum memories must be heralded.

In that situation, the repetition rate of the entanglement attempts is limited to $R = c/L_0$ where L_0 is the distance between the ensembles. For example, for L=100 km, R=2 kHz. In that case, temporal multiplexing would increase the entanglement rate by a factor N_m for low success probability [34].

In conclusion, we presented a temporally multiplexed quantum repeater node based on cold atomic ensembles. By implementing a controlled inhomogeneous broadening of the spin transition, we generated distinguishable spin waves. We significantly reduced noise due to dephased spin waves by embedding the ensemble inside a low finesse optical cavity. This allowed us to demonstrate multiplexed generation of non-classical spin wave - photon pairs in up to 10 temporal modes, enabling a corresponding increase in generation rate. These correlated pairs could also serve as a source of high-dimensional light-matter entanglement in time. The multiplexing capability can be further enhanced by using a higher finesse cavity or by combining temporal multiplexing with other techniques such as spatial multiplexing.

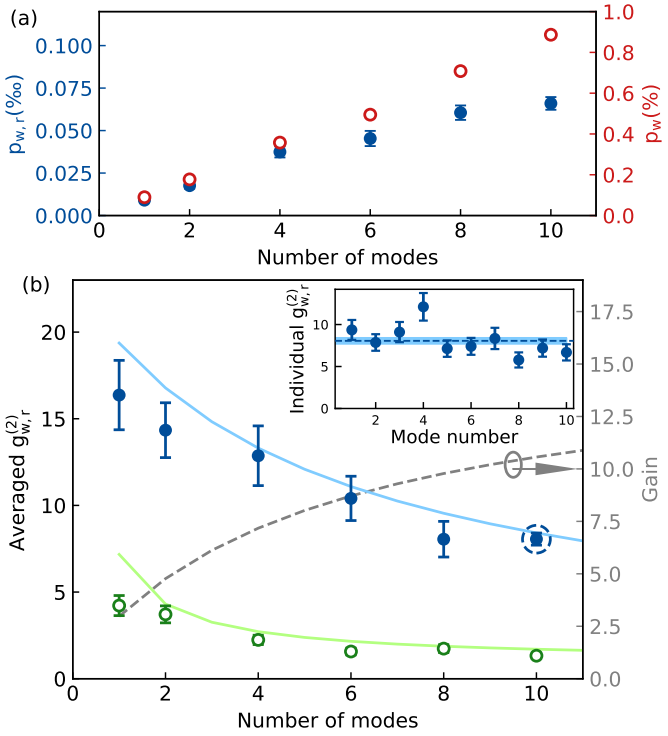

Figure 4.5: (a) Write and total write-read detection probability as a function of the number of temporal modes with cavity. (b) Averaged correlation function between write and read photons as a function of the number of modes. Average is computed based on the sum of coincidence and noise counts from all modes. Error bar is one stdev, again based on the sum of counts in all modes. Blue (green) data is taken with (without) cavity enhancement. Grey dashed line shows the gain $(g^{(2),\,c}_{w,r} - 1)/(g^{(2)}_{w,r} - 1)$ in cross-correlation enabled by the cavity, as a function of the number of modes. Here, $g^{(2),\,c}_{w,r}$ ($g^{(2)}_{w,r}$) is the cross-correlation value with (without) cavity. Inset shows $g^{(2)}_{w,r}$ of each mode for the 10-mode data point. Single-mode excitation probability is $p_{1m} \approx 0.045$ for all measurements.

Chapter 5

Raman storage of quasideterministic single photons generated by Rydberg collective excitations in a low-noise quantum memory

This experiment was a joint effort involving a single-photon source and an absorptive quantum memory. While fellow PhD student Jan Lowinski was responsible for the source, the optimisation and operation of the memory was my task. The connection and synchronisation of the two setups was worked-out by the whole team. The main experimental challenges were low data-taking rates (making it necessary to acquire data for up to 60 hours per data point), long-term experimental drifts and technical noise introduced by control beams. Our experimental results are published in [127], and the text in this chapter is adapted from this publication. The published manuscript was written jointly by the whole team, Jan Lowinski prepared the figures.

5.1 Introduction

To date, most of the early demonstrations of quantum repeater links are based on probabilistic light-matter entanglement sources. This includes emissive quantum memories using spontaneous Raman scattering in atomic ensembles [23, 24, 114, 115, 117], following the DLCZ proposal, and absorptive quantum memories combined with spontaneous parametric down-conversion sources [27, 121]. These types of probabilistic sources bear intrinsic limitations due to a trade-off between excitation probability and fidelity of the generated state, as explained in subsection 1.2.2. To keep the errors due to the generation of multiple pairs low, and therefore the fidelity high, the generation probability must remain low.

A quantum repeater architecture based on deterministic single photons and absorptive quantum memories was proposed to overcome this limitation [33]. In this scheme, each node consists of a deterministic single-photon source, a beam splitter (BS) and a quantum memory. The transmitted modes of the BS in each node are overlapped on the remote BSM and a photon click heralds entanglement stored in the memories. Each deterministic source emits at most one photon. Therefore, as discussed in subsection 1.2.3, only one photon can be stored per link, while the second photon is consumed in the heralding. This suppresses the aforementioned errors in the subsequent swapping stage. The main challenge of this scheme is to generate memory-compatible indistinguishable single photons on demand with high efficiency. In addition, the quantum memory should feature very low noise in order not to degrade the single photon properties.

It has been shown that heralded single photons, generated from probabilistic sources, can be stored in quantum memories [95, 187] with up to 87 % storage and retrieval efficiency [55, 56]. In principle, such a heralded source can be used to emulate a true single photon source. The heralding rate is, however, again limited by the above-mentioned multi-photon emissions. Several approaches have been demonstrated to generate on-demand single photons using single emitters such as quantum dots, single molecules and color centers in diamond, as discussed in detail in subsection 1.3.3. However, most of these photons are not resonant with quantum memories and have

a bandwidth much larger than the one of long-lived quantum memories. While progress has been made recently to interface photons from quantum dots and molecules to atomic vapors or rare-earth doped solids [100, 102, 103, 108, 188], so far high efficiency and long-lived storage of these photons has not been demonstrated. Single trapped atoms can be used to generate directly resonant and memory-compatible photons that have been interfaced with a BEC quantum memory [107], however, the efficient photon generation in a single mode requires placing the atom in a high-finesse cavity, which is an experimentally complex task.

In recent years, several experiments have shown that ensembles of Rydberg atoms could serve as a source of on-demand narrow-band [111, 189–191] indistinguishable single photons [97, 192, 193]. Rydberg atoms are atoms where at least one electron was promoted to a highly excited state. In such a system, the number of generated Rydberg excitations is strongly limited due to the dipole blockade [110]. The blockade is a result of the strong dipole-dipole interaction between Rydberg states, which prevents a simultaneous excitation of two Rydberg atoms, if they are closer than a distance called the blockade radius. Then, if the interaction region is smaller than the volume given by the blockade radius, only one atomic excitation will be created in state $|r\rangle$ - this is called the fully blockaded regime. The Rydberg excitation is shared between all the atoms in the blockade region, forming a collective quantum superposition, termed Rydberg spin wave. This spin wave can be retrieved as an on-demand single photon after a programmable delay by means of a second coupling pulse. Constructive atomic emission ensures the emission into a well-defined spatial mode. This approach has the advantage that no high-finesse cavity is required, due to the collective nature of the single photon generation.

In this experiment, we demonstrate the storage and retrieval of an on-demand single photon generated by a collective Rydberg excitation on a low-noise Raman quantum memory located in a different cold atomic ensemble. We show that the single photons can be stored and retrieved with a signal-to-noise ratio (SNR) up to 26, preserving strong antibunching. In addition, we showcase some important properties of Raman storage as a versatile protocol for quantum networks. The results are an important

step towards the implementation of efficient quantum-repeater links using single-photon sources.

While finalizing our experiment, we learned about a recent experiment where a photon generated by Rydberg atoms was stored in an atomic ensemble using EIT [194]. While our experiment targets efficient quantum repeater links, Yu et al. verify that their memory is entanglement-preserving via a measurement-device-independent scheme.

5.2 Experimental setup

Our experimental setup comprises of two ensembles of cold ^{87}Rb atoms located in the same laboratory connected via 12 m of optical fiber cable. One of them is used to generate single photons by exploiting dipole-dipole interaction between Rydberg states (the source). Another is used to store and retrieve the generated photons in the Raman memory described earlier.

In the first step of the generation protocol we excite the source ensemble from its ground state $|g_s\rangle = |5S_{1/2}, F = 2\rangle$ to a Rydberg state $|r\rangle = |90S_{1/2}\rangle$, see Fig. 5.1(d), via a two-photon excitation. We send a weak coherent probe pulse Ω_p and a strong counter-propagating coupling pulse $\Omega_c \approx 6$ MHz, see Fig. 5.1(a). The $1/e^2$ beam radius is 6.5 µm for the probe and 13 µm for the coupling mode. The probe light at a wavelength of 780 nm is red-detuned by -40 MHz from the transition to the excited state $|e_s\rangle = |5P_{3/2}, F = 3\rangle$. The coupling light is tuned such that the two-photon transition is resonant with the transition $|g_s\rangle \rightarrow |r\rangle$.

With a delay of 1 µs, a second coupling pulse is sent resonantly to the $|r\rangle \rightarrow |e_s\rangle$ transition, mapping the Rydberg spin wave onto the excited state $|e_s\rangle$ and triggering the collective emission of a single photon at 780 nm. The photon is emitted in the input mode and in forward direction thanks to collective atomic interference. It is then separated from the coupling light by a dichroic mirror and a band-pass filter, before being collected into a polarization-maintaining single-mode fiber. An electronic trigger is sent to the memory to signal each photon generation attempt.

The generated photon is guided to the second atomic ensemble, the

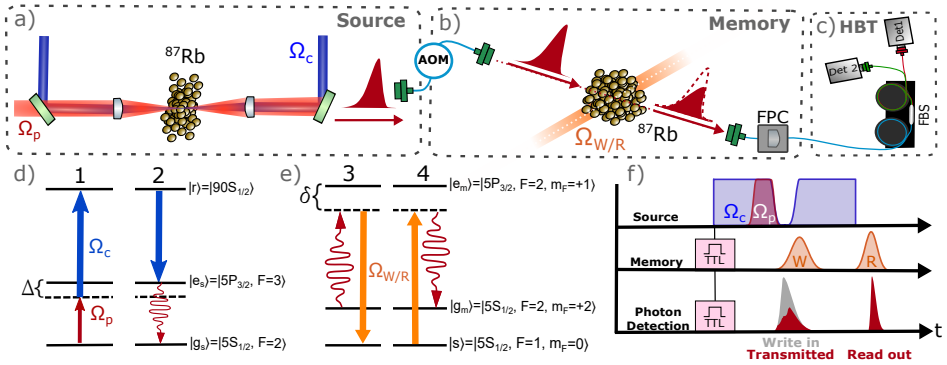

Figure 5.1: A scheme of the experimental setup, the relevant atomic levels and the experimental sequence. (a) The source. The probe Ω_p and the counter-propagating coupling beam Ω_c are tightly focused in a cold cloud of Rubidium atoms to generate the input photon. (b) The memory. A write-in control beam pulse Ω_W maps the incoming photon to an atomic excitation in another cold cloud of Rubidium atoms. The excitation is retrieved with a read-out control beam pulse Ω_R and filtered with a Fabry-Perot cavity (FPC). (c) The retrieved photon is split in a fiber-based beam-splitter (FBS) and detected with SNSPD 1 and 2 performing, effectively, an HBT measurement. The relevant atomic levels for the photon generation (d) and for the photon storage (e) are also shown. (f) The pulse sequence. The setups are synchronized with TTLs sent by the source in each trial.

memory. The frequency of the photon is not compatible with the transitions used in the memory, so it is shifted by $-320\,\mathrm{MHz}$ with an AOM. As a result, the photon is now red-detuned with respect to the $|g_m\rangle \to |e_m\rangle$ transition.

The Raman memory relies on coherent, adiabatic absorption of the incoming single photon [135], as explained in detail in subsection 2.2.2. A storage attempt starts with sending a control write-in pulse Ω_W coupling states $|s\rangle = |5S_{1/2}, F = 1, m_F = 0\rangle$ and $|e_m\rangle = |5P_{3/2}, F = 2, m_F = +1\rangle$ off-resonantly by $\delta = -52\,\mathrm{MHz}$, see Fig. 5.1(e). Assuming that the $|g_m\rangle \to |e_m\rangle$

transition is lifetime-limited, the excited state coherence lifetime is $2\tau_{eg}$, with $\tau_{eg} = 26\,\text{ns}$ the excited state population lifetime. Since the write-in pulse is in two-photon resonance with the input photon, the incoming photon field is transferred to a collective atomic spin excitation on $|s\rangle$. Careful tuning of the control write-in pulse shape, power and timing with respect to the input photon is required to optimize the writing efficiency into the memory. Experimentally, we find that the optimum control write-in pulse closely resembles the input photon wave shape and impinges on the cloud shortly before the photon, with $\Omega_W \approx 48\,\text{MHz}$.

To retrieve the stored excitation, after a programmable delay we send a read-out pulse Ω_R. The read-out pulse is in the same spatial mode as the write-in pulse with the same frequency detuning δ. Owing to collective atomic interference, the photon is emitted in the input mode in the forward direction and collected into a single-mode fiber. The bandwidth and the shape of the output photon are governed by the temporal profile and the power of the read-out pulse and can be tuned (see subsection 5.3.2).

The collected photons are guided to the detection setup. Depending on the measurement it is either a superconducting nanowire single-photon detector (SNSPD) or a Hanbury Brown-Twiss (HBT) setup comprised of a fiber-based beam splitter and two SNSPDs, see Fig. 5.1(c).

For the source to produce single photons it is necessary to be in the fully blockaded regime or close to it. Moreover, the coherence time of the Rydberg transition should be much longer than the excitation pulse duration to keep the photon generation probability high. In our case, this means that the ensemble needs to be cold to limit the motional dephasing. Both requirements are achieved in the preparation stage when we first load the atoms into a MOT, later compress them and subsequently apply 7 ms of PG cooling. Finally the ensemble is prepared by optical pumping to its initial ground state $|g_s\rangle = |5S_{1/2}, F = 2\rangle$. A one-dimensional dipole trap is kept on during the whole process (with a beam waist of 34 µm at an angle of 22° with respect to the probe beam and a trap depth of 0.3 mK). The whole process results in a cloud with OD of 6 and a temperature of 40 µK. Thanks to the dipole trap, the effective interaction region given by the overlap between the probe beam and the atomic ensemble, is still larger

but comparable to the $\sim 13\,\mu m$ of the blockade radius. The ensemble can be interrogated for 200 ms, limited by the population lifetime of the dipole trap (400 ms), before another MOT reloading cycle has to be performed. During its interrogation time, the source attempts to generate a single photon every $4\,\mu s$ with generation probability $p_{\mathrm{gen}} = 5$ to 15 %. The photon generation and the characterization of their indistinguishability is described in more detail in [193].

For the memory, the OD of the ensemble and the cloud temperature are the main parameters governing the storage and retrieval efficiency and the storage time. The atoms are first loaded into a MOT for 10 ms followed by 1.5 ms of PG cooling. Later the memory is optically pumped to its initial ground state $|g_m\rangle = |5S_{1/2}, F = 2, m_F = +2\rangle$, in the presence of a homogeneous magnetic bias field oriented along the photon mode. Optical pumping is helpful to avoid beating between spin waves at different Zeeman sublevels. This provides us with a cloud of OD of 5 and a temperature of $30\,\mu K$. OD starts dropping after 1.2 ms of interrogation time and the trapping cycle has to be repeated.

A main challenge of this study was long integration times, which required good stability of both setups. This results mainly from two technical limitations. The first one are the different trapping cycles of the source and the memory, making the overall duty cycle low. The resulting repetition rate of the whole experiment is 5 kHz. The second one is photon transmission losses which affect quadratically the coincidence probability in HBT. The total transmission from the output of the source to the detection setup is 10(1) %, limited by the fiber coupling after the source (0.4), the frequency-shifter AOM (0.62), the fiber coupling after the memory (0.83), the frequency-filtering cavity setup (0.65) and miscellaneous optical and polarisation-dependent losses (0.75). The transmission from the output of the source to the input of the quantum memory is 22 %. The SNSPDs have quantum efficiency $\sim 85\,\%$ and 3 Hz dark counts. The limiting factor for the quality of the single photon retrieved from the memory is photon noise. The main source of noise is the leakage of the memory control pulses which couple to the photon mode. An angle of 3 degrees between the photon mode and the coupling beam minimizes the spatial overlap and noise introduced

by directional, forward scattering. The noise is further removed with the narrow-band Fabry-Perot filter cavity of 43.4 dB suppression described in subsection 3.4.3. The remaining noise is composed of light leaking through the filter, inelastically scattered control light at the photon frequency and the detectors' dark counts.

5.3 Results

In this section we study the single photon properties of the source photons which, further on, are used as the memory input photon. We also discuss the performance of this Raman memory as a versatile protocol for hybrid quantum networks.

5.3.1 Photon Generation

The HBT setup is used to characterize the photons generated by the source. Photon arrival times at each SNSPD are recorded together with trigger times for each trial. We compute the second-order autocorrelation as:

$$g^{(2)}(k) = \frac{c_{1,2}(k)}{p_1 p_2}, \tag{5.1}$$

where p_1 (p_2) is the probability of detection per trial with SNSPD 1 (2) and $c_{1,2}(k)$ is the probability of a coincidence between detections separated by k trials. All the probabilities are calculated within a detection time window at fixed delay after each trial trigger. We choose a 300 ns detection window which includes more than 95 % of the photon. For perfect single photons, $g^{(2)}(0) = 0$. In practice, background noise or multi-photon components increase the $g^{(2)}(0)$. Emitted light remains non classical for $g^{(2)}(0) < 1$ and $g^{(2)}(0) = 0.5$ marks the limit between single and multi-photon states.

In our source we can change the emitted photon $g^{(2)}(0)$ within a range of 0.16 to 1 by varying the mean probe photon number, see Fig. 5.2. For smaller probe photon number the increase of $g^{(2)}(0)$ is accompanied by an increase of the photon generation probability p_{gen}, which is defined as $p_{\text{gen}} = (p_1 + p_2)/\alpha$

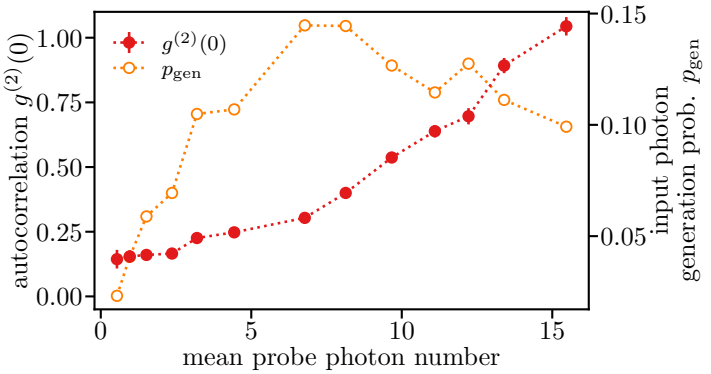

Figure 5.2: Dependence of $g^{(2)}(0)$ and p_{gen} on mean probe photon number. p_{gen} follows the Rabi cycle decreasing for the largest values of the probe power while $g^{(2)}(0)$ grows monotonically up to 1.

where $\alpha = 0.21$ is the combined transmission and detection efficiency (of the source only - in this characterisation we detected photons right after the source). However, for larger probe photon number p_{gen} decreases in accordance with the Rabi cycle. Yet, this is not accompanied by the $g^{(2)}(0)$ which continues to grow up to 1, indicating the presence of multiphoton components. The reason for this behaviour is still under investigation and goes beyond the scope of this paper.

If not stated otherwise, for the following measurements we fix $g^{(2)}(0) \approx 0.23$ and $p_{\mathrm{gen}} \approx 12\,\%$. The emitted photon has a steep leading edge followed by a slower exponential decay, with a full width at half maximum (FWHM) of the entire photon of $\sim 90\,\mathrm{ns}$, see Fig. 5.3(a) at time zero.

5.3.2 Photon Storage

To characterize the memory performance, we first measure the temporal histogram of photon counts in 3 different situations, as shown in Fig. 5.3(a). We first detect the input single photon (orange histogram) when no storage attempt is performed, i.e. with no atoms in the memory but with control

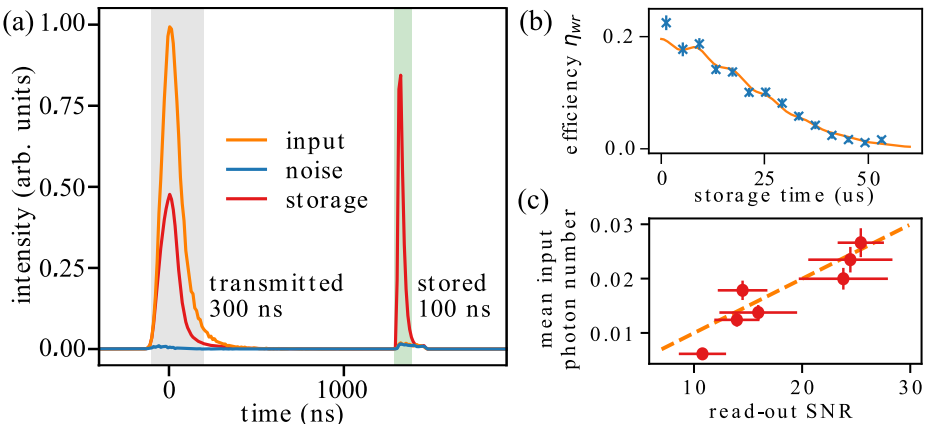

Figure 5.3: (a) Photon histogram observed at the SNSPDs after the memory. The orange histogram is the input photon without storage. The red histogram presents a storage attempt. The blue histogram shows the noise without input photon. The shaded areas are the respective detection windows. (b) Storage and retrieval efficiency as a function of storage time with a corresponding Gaussian fit e^{-t^2/τ^2}, where τ is the memory lifetime. The fit includes an oscillatory term accounting for spin wave interference coming from residual population in $|5S_{1/2}, F = 2, m_F = 1\rangle$, a consequence of imperfect Zeeman optical pumping [146]. (c) Mean number of single photons at the input of the memory as a function of the read-out SNR. Orange dashed line: linear fit that passes through zero. The slope of this line corresponds to μ_1.

pulses. Then, a storage attempt is performed (red histogram) leading to two peaks - the transmitted pulse, which is the part of the input that is not absorbed in the storage attempt (counts in the 300 ns grey shaded window), and the stored pulse, which is the excitation retrieved from a successful storage attempt (counts in the 100 ns green shaded window). Finally, we measure the noise (blue histogram) by blocking the input photon while keeping the atoms in the memory and all the control pulses on. We measure a corrected noise probability per trial at the output of the quantum memory, within the storage window, of $p_{\text{noise}} = 2.3(3) \times 10^{-4}$, which is derived

from the detected noise probability as $p_{\text{noise}} = p_{\text{noise}}^{\text{det}}/\beta$, where $\beta = 0.34$ is the combined transmission and detection efficiency after the memory (at the photon frequency). To our knowledge, this value is among the lowest reported in ground state spin wave memories and is comparable to other quantum memories based on cold atoms or BECs [56, 143, 187, 195, 196]. We attribute this noise to the control pulse light leaking through the filter and scattering resulting from residual population on the storage transition. Four-wave mixing (4WM), which is an important source of noise in hot vapour memories, is not observed: The noise floor remains constant as a function of storage time, which would not be the case if 4WM introduced additional spin waves. The control beam does not couple the atomic ground state $|g_m\rangle$ to any excited state, a necessary requirement for 4WM to occur. Furthermore, the angle of 3° between control and photon mode is prohibitively large for the phase-matching condition to be satisfied [196]. 4WM does not occur in the photon source because of the ladder scheme.

The input and the noise histograms serve as a reference to calculate the storage and retrieval efficiency $\eta_{wr} = p_s/p_{\text{in}}$, where p_s and p_{in} are background-subtracted probabilities of detecting a stored photon and an input photon, respectively. We also calculate the write-in efficiency defined as $\eta_w = (p_{\text{in}} - p_t)/p_{\text{in}}$, where p_t is the background-subtracted detection probability of a transmitted photon. From these two quantities we infer the read-out efficiency $\eta_r = \eta_{wr}/\eta_w$. For this connection experiment, we obtain a maximum storage and retrieval efficiency $\eta_{wr} \approx 21\,\%$ at a storage time of 1.2 µs. For longer storage times the motional decoherence and the decoherence due to the stray magnetic field gradients limits the efficiency with a characteristic $1/e$ decay time of 30 µs, see Fig. 5.3(b). Higher efficiencies can be achieved for longer MOT loading and correspondingly higher OD, see appendix C.1.

For the measurement shown in Fig. 5.3(a), the SNR of the retrieved photon is 24(4). An interesting figure of merit is the μ_1 parameter, defined as $\mu_1 = p_{\text{noise}}/\eta_{wr}$, which expresses the input number of photons required to have SNR = 1 at the output. By varying the Rydberg probe power, we find $\mu_1 = 1.00(7) \times 10^{-3}$, see Fig. 5.3(c). This is more than two orders of magnitude lower than similar ground state quantum memories based on

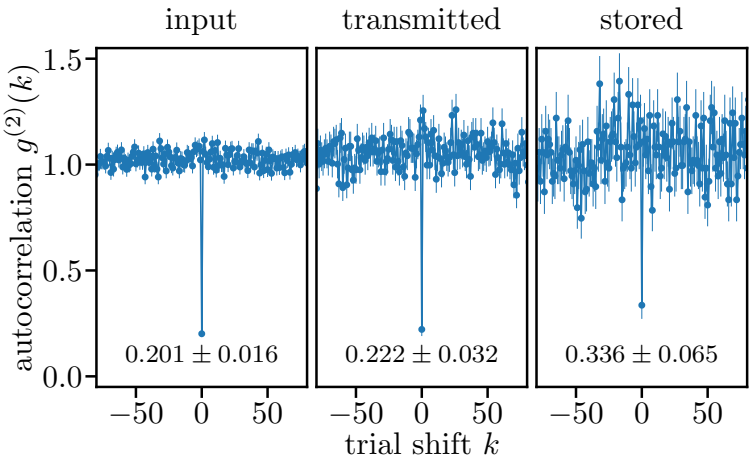

Figure 5.4: Autocorrelation $g^{(2)}$ as a function of shift between trials k for the input, transmitted and stored photons. For trials separated by a shift $k \geq 1$ the clicks are uncorrelated yielding $g^{(2)}(k) = 1$. Coincidences clicks in the same trial, $k = 0$, are much less frequent asserting the photons anti-bunching.

warm atomic vapors [101, 197, 198], more than one order of magnitude lower than solid-state QMs based on rare-earth doped solids [175, 177] and similar to other quantum memories based on cold atoms [56, 143, 187, 195, 196].

A crucial requirement for a quantum memory is that it preserves the statistical properties of the stored photons. To show this, we first adjust the mean probe photon number of the source to low values, resulting in a photon generation probability of $p_{\text{gen}} \approx 3.0(3)\,\%$ (see Fig. 5.2). With this setting, we expect the emitted photons to be strongly non-classical. To reduce the effect of experimental fluctuations, we collect data for 63 hours. We measure $g^{(2)}(0)$ of the input (0.20(2)), transmitted (0.22(3)) and stored photons (0.34(7)) and obtain values well below 0.5, see Fig. 5.4. It shows that the memory preserves the single photon nature of the input photon. One can see, however, that $g^{(2)}(0)$ of the stored photon is significantly larger than the $g^{(2)}(0)$ of the input photon. We expect that the main source of

degradation of $g^{(2)}(0)$ is the uncorrelated noise introduced by the memory control pulses. We developed a simple model, discussed in appendix C.2, to quantify the effect of uncorrelated noise on $g^{(2)}(0)$. The model predicts a $g_m^{(2)}(0) = 0.33(4)$ for stored photon taking into account a measured SNR of 11(2) and the measured input $g^{(2)}(0)$. For this data set, the model is in agreement with the measured data, within the error bars. We also performed several other measurements (see appendix C.2, with integration times of around 10-16 hours per data point) for different input $g^{(2)}(0)$. While the model reproduces qualitatively the trend, there is a large point to point fluctuation that we attribute to low statistics and experimental fluctuations.

5.4 Raman storage as a versatile protocol for hybrid quantum networks

Our memory offers significant tunability in the write-in process that may prove useful in future hybrid quantum networks [29]. We start by showing that the memory can adapt to the input photon frequency. For that, we set the input photon detuning to $\delta = -52\,\text{MHz}$ and we vary the frequency of the control beam pulse. The maximum efficiency is observed for the two-photon resonance, see Fig. 5.5(a).

The width of the curve depends on the spectral properties of the input photon. Bandwidth-limited photons (i.e. photons that exhibit the minimum bandwidth for a given temporal duration) are desirable because one can achieve with them a high Hong-Ou-Mandel interference visibility over the whole duration of the pulse [199, 200]. In order to benchmark the spectral properties of the input photon, we repeat the measurement with a weak coherent state (WCS) with the same waveshape, center frequency and mean number of photons. This WCS is derived from a laser exhibiting a linewidth much smaller than the bandwidth of the pulse. As can be seen in Fig. 5.5(a), both spectra overlap very well suggesting that the input photon is close to bandwidth-limited. Using classical light pulses, we also performed storage at detunings $\delta = -32\,\text{MHz}$ and $\delta = -72\,\text{MHz}$ (not shown here). No significant change of η_{wr} was observed, suggesting that the input photon detuning can

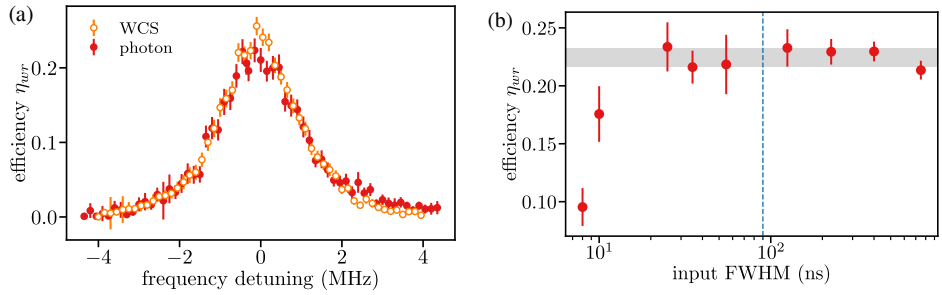

Figure 5.5: (a) Storage and retrieval efficiency versus frequency detuning of the control write-in pulse for the single photon input (red) and WCS (orange). The frequency detuning is measured from the two-photon resonance of the input and the control beam. (b) Storage and retrieval efficiency η_{wr} as a function of the temporal duration (FWHM) of WCS input pulses with Gaussian shape. Grey horizontal shaded area represents the mean efficiency (0.225(8)) for input pulse durations above 25 ns. Blue dashed vertical line represents the minimum duration of the single photon generated by the Rydberg-based source (∼90 ns FWHM). For each data point, write-in control pulse power, shape and delay are optimized.

be varied within this range.

Eventually, the detuning will be limited by the proximity to other atomic levels. To understand whether the memory efficiency is limited by this input bandwidth, we measure η_{wr} for Gaussian-shaped WCS pulses with variable duration[1]. The duration of the WCS pulses is controlled by an AOM, achieving pulses as short as 8ns. The results are shown in Fig. 5.5(b). For pulse durations between 25 ns and 750 ns, η_{wr} remains constant and is in agreement with the efficiencies measured for the single-photon input.

[1]The maximum duration of the single photons generated at the source is limited to approximately 1 μs by the dephasing rate of the collective Rydberg excitations. The minimum duration is limited by the coupling beam power, leading to FWHM greater than ∼90 ns. To achieve a larger tuning range, we instead send WCS pulses with mean number of photons well below 1.

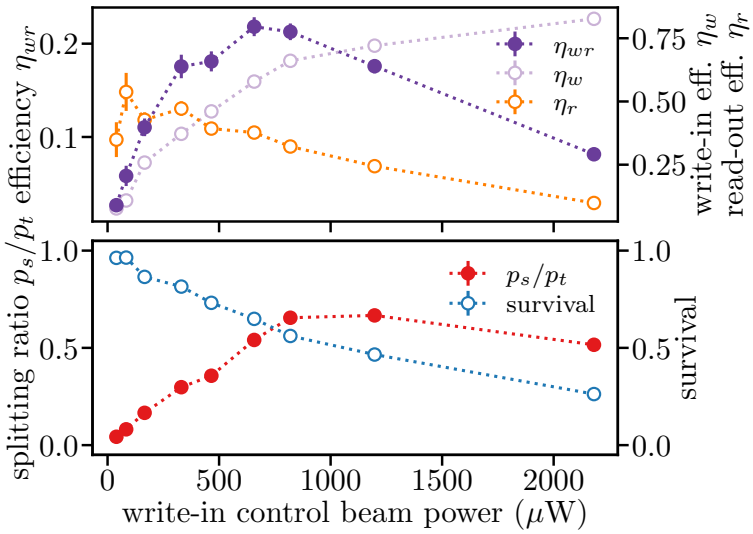

Figure 5.6: Storage efficiencies, survival probability and splitting ratio as a function of the write-in control beam power.

Only for pulse durations below 25 ns, corresponding to a bandwidth of about ≈17.6 MHz (assuming transform-limited Gaussian pulses), the storage and retrieval efficiency drops. We attribute this drop to limited control power and finite AOM rise time, resulting in an insufficient pulse area. For input pulses much longer than 750 ns (not characterised here), the efficiency is expected to be eventually limited by the lifetime of the memory [80]. We estimate the bandwidth of the single photon to be approximately 4 MHz, assuming bandwidth-limited Gaussian pulses.

Another interesting feature of the memory is that one can control how much of the input photon is absorbed and how much is transmitted. By varying the write-in control beam power one can change η_w as shown in Fig. 5.6 (top). This changes effectively the splitting ratio p_s/p_t between the stored and the transmitted photon pulse. Our memory can therefore be used as a temporal beam splitter [201] with a tunable splitting ratio. Substituting

the BS + QM in the proposed repeater architecture [33] with only the QM and guiding the transmitted light directly to the intermediate station, relaxes the requirements for storage efficiencies to approach unity. To investigate this possibility, we plot p_s/p_t, see Fig. 5.6 (bottom). It peaks for intermediate values of the write-in control beam powers and decays for higher values. This stands in contrast with the monotonically growing η_w and is a result of η_r decreasing with the control power. We attribute this behaviour of η_r to the asymmetrical distribution of the spin wave in the ensemble, when large write-in control powers are used [135, 202]. With increasing write power, the spin wave starts having more asymmetric shape, being mostly created at the beginning of the ensemble. This effect is known to limit the retrieval efficiency, especially in the forward retrieval configuration [138, 203, 204]. In Fig. 5.6 (bottom), we also plot the survival efficiency $(p_s + p_t)/p_{\text{in}}$, the normalized probability of detecting a transmitted or stored photon per trial. We observe that it decreases with increasing control power due to the decrease of the read-out efficiency.

With current conditions, the tunability range of p_s/p_t is limited, but we expect that backward retrieval should considerably improve the read-out efficiency at high write power [202]. As a first application of the single photon temporal beam splitter, we used the two temporal output modes of the memory to measure the antibunching parameter. For the measurement presented in Fig. 5.4, we obtain a $g^{(2)}(0) = 0.28(2)$ with a significantly increased count rate with respect to the case where we split each output mode with a standard BS.

Our memory can also tune the wave shape of the stored photon [80]. In particular, one can retrieve photons with very different lengths (with FWHM of 25 to 900 ns) by changing the read-out control beam power, see Fig. 5.7(a, b). We read out the memory with a square-shaped pulse resulting in a steep leading edge of the retrieved photon and slower decaying trailing edge. We fit the former with a Gaussian function and the latter with an exponential and obtain the total FWHM of the photon. One can also use more complex waveforms for the read-out control pulse to shape the read-out photon, e.g. reproducing the input photon or a time-bin qubit, see Fig. 5.7(c, d). This capability would allow for matching differently shaped photons emitted by

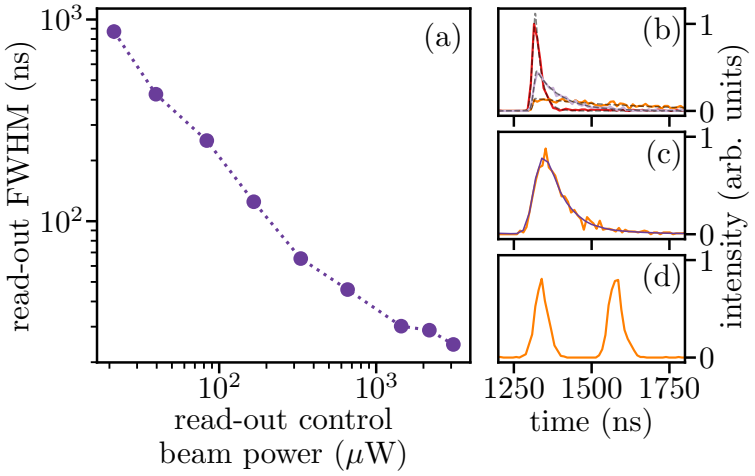

Figure 5.7: Stored photon waveshape tunability. (a) Dependence of the stored photon duration on the read-out control beam power. (b) Selected waveshapes of the stored photons from (a) and their corresponding fits. (c) Stored photon waveshape (solid orange) matching exactly the input photon waveshape (dashed blue). (d) Stored photon shaped as a time-bin qubit.

different sources. We do not observe significant reduction of η_{wr} for different read-out pulse shapes, in agreement with theory [141].

5.5 Discussion

We demonstrated storage and retrieval of an on-demand single photon generated in a Rydberg-based atomic ensemble in another cold atomic ensemble through a Raman memory protocol. We achieved a 21 % memory efficiency and a signal-to-noise ratio up to 26 for the retrieved photon, leading to μ_1 of $1.00(7) \times 10^{-3}$. We observed only a moderate degradation of the single photon statistics, in agreement with a theoretical model taking into account photon noise. We showed the adaptability of our memory in frequency and bandwidth. Moreover, we evaluated the performances of the

built-in temporal beam splitter offered by the Raman memory. Lastly, we showed that we can shape the temporal waveform of the retrieved photon by shaping the read-out pulse power and waveform. These results are a step forward in the implementation of efficient quantum-repeater links using single-photon sources. In that context, one interesting advantage of having the source and the memory residing in different ensembles is that they can be optimized independently. This allows for an efficient single-photon generation and storage and facilitates the use of multiplexed quantum memories [70, 126], which would significantly improve repeater entanglement generation rates.

Several improvements should be applied to our experiment before it can become a practical alternative. The generation efficiency of the single photon from the Rydberg ensemble could be increased by increasing the OD of the ensemble and/or by embedding the ensemble in a low finesse cavity [205]. The quality of the single photon (as measured by the autocorrelation function $g^{(2)}(0)$) could also be improved by addressing a slightly smaller ensemble and by reaching higher principal quantum number level to increase the Rydberg blockade radius, as was shown in [97], where $g^{(2)}(0)$ values smaller than 10^{-3} have been measured. Regarding the Raman quantum memory, higher storage and retrieval efficiencies could also be reached by increasing the OD of the ensemble [56] and using backward retrieval [138], or with an impedance matched cavity. Backward retrieval will also improve the survival probability and the performances of the temporal beam-splitter. Finally, longer storage time up to 1 s could be achieved by using magnetic insensitive transitions and by loading the ensemble into an optical lattice to suppress motional induced dephasing [65].

Chapter 6

Cavity-enhanced spin-wave storage

Efficient photon storage and retrieval is a necessary requirement for any quantum memory. The theory introduced in chapter 2 suggests that the underlying light-matter interaction can be enhanced by interfacing the atomic spin wave memory with a low-finesse cavity. This chapter investigates the possibility to improve the storage efficiencies of the two protocols used in this thesis: DLCZ and Raman storage. To this end, the already existing cavity installed around the atoms is employed (chapter 3 and chapter 4). In DLCZ storage, write and read photon have different frequencies, and the two processes can be investigated independently. Here, we focus on read-out enhancement, as the write process had been studied in chapter 4. In Raman storage, the two photons can be engineered to have equal frequency (and polarisation), such that a cavity naturally supports both processes.

6.1 Cavity-enhanced DLCZ read-out

Laser-cooled ensembles offer a way to implement highly efficient light-matter entanglement via the DLCZ protocol [16, 65, 79]. To reach close-to-unity efficiencies, high light-matter interaction is required [155, 206]. This can

be implemented with large clouds of high OD, as shown for EIT memories [55, 56, 67]. However, the spin wave vector in the DLCZ memory has opposite sign (compared to both Raman or EIT memories) due to a slightly different phase matching condition. The atomic remission therefore interferes destructively when $|\mathbf{\Delta}k|L \gg 1$, where $\mathbf{\Delta}k$ is the spin wave vector and L the length of the cloud. This holds true even when the pulse and photon modes are all colinear, in which case the spin wave vector is minimal. The reason is that the two ground states $|g\rangle$ and $|s\rangle$ are non-degenerate. When taking into account this ground state splitting, for the DLCZ protocol momentum- and energy conservation are never full-filled simultaneously. Larger clouds do not tolerate this residual momentum mismatch, similar to the reduced phase matching bandwidth in longer periodically-poled crystals for parametric conversion. This is explained in more detail in appendix D.1. For Rubidium, the minimum spin wave period is given by the ground state splitting of 6.8 GHz, $\Lambda = 2\pi/|\Delta k| \approx 45\,\text{mm}$ [140, 207]. The cloud length in the above-mentioned publications was between 20 to 30 mm [55, 67]. The largest free-space efficiency reported for a DLCZ-type memory is therefore only around 50% [155]. One solution is to combine a smaller cloud of moderate OD with a low-finesse optical cavity enhancing the light-matter interaction. DLCZ in cavity has already been demonstrated and exploited in several publications [65, 88, 156, 208]. Here, we test this idea in our system and provide a detailed characterisation, involving aspects which have not been investigated before.

For this study, $|5^2S_{1/2}, F = 2\rangle$ is chosen as the DLCZ ground state and $|5^2S_{1/2}, F = 1\rangle$ as the storage state. No Zeeman optical pumping is applied, and a small bias field perpendicular to the photon mode is applied. No filter cavities were used. The excitation scheme is chosen such that the read photon is horizontally polarised and resonates with the cavity, while the write photon is vertically polarised and decouples from the cavity on the PBS. For details on the setup and level scheme, see appendix D.2.

First, the enhancement cavity is tuned into resonance with the read photon transition $|5^2P_{3/2}, F = 2\rangle \rightarrow |5^2S_{1/2}, F = 2\rangle$. Then, DLCZ storage is performed, and the read pulse frequency is scanned. The intra-cavity retrieval efficiency as a function of the read pulse detuning is shown in Fig. 6.1(a).

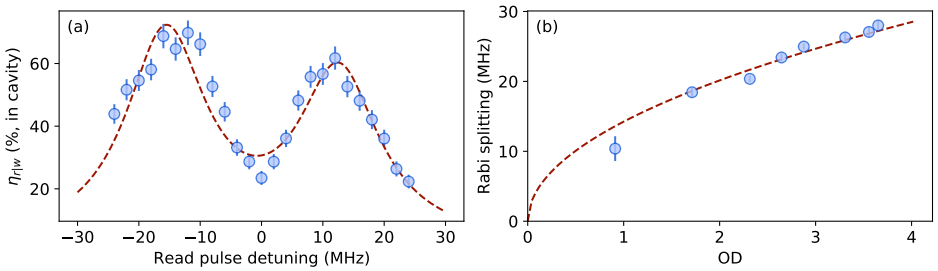

Figure 6.1: (a) Cavity-enhanced DLCZ read-out efficiency as a function of the read pulse detuning, for an OD of 3.8. Zero detuning corresponds to the resonance of the read photon transition. Red dotted line is a fitted VRS absorption profile (see appendix D.3), yielding a cavity detuning of $-3\,\mathrm{MHz}$ and a Rabi splitting of 28 MHz in this particular case. (b) Rabi splitting as a function of OD on the read photon transition. Red dotted line is fitted with $f(\mathrm{OD}) \propto \sqrt{\mathrm{OD}}$.

Two distinct peaks of enhanced efficiency are present, a consequence of the vacuum Rabi splitting (VRS) originating from the coupling between the atomic transition and the cavity resonance [209–211]. If the cavity was in perfect resonance with the transition, this feature would be symmetric.

The retrieval efficiency shown in Fig. 6.1(a) is calculated from the detected efficiency through back-propagation, taking into account the cavity escape efficiency (55%), fiber coupling (85%), transmission through the chopped lock (54%) and detector efficiency (45%). It is also corrected for false heraldings, as the write photons are not filtered[1]. Intra-cavity retrieval efficiencies of up to 70% are achieved.

VRS is described in the context of absorption or spontaneous emission of light. The splitting between the two peaks is then equal to the Rabi frequency $\Omega = 2g\sqrt{N} \propto \sqrt{\mathrm{OD}}$, a function of the atom number $N \propto \mathrm{OD}$ and the atom-cavity coupling $g = \mu\sqrt{w_0/(2\epsilon_0\hbar V)}$. Here, w_0 is the mode

[1]As the precise branching ratio will depend on the distribution of atomic population on the Zeeman sublevels, a branching ratio of 50% was assumed here.

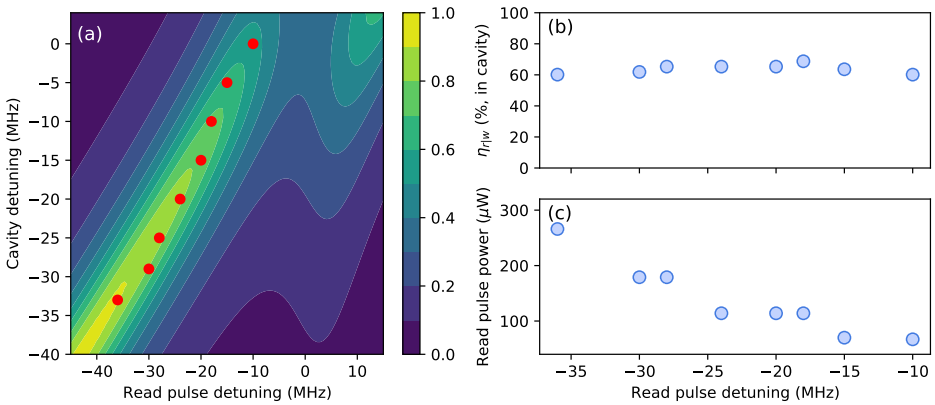

Figure 6.2: (a) Measured points of highest retrieval efficiency as a function of cavity and read pulse detuning, superimposed with the expected VRS absorption spectrum (in arbitrary units). (b), (c) In-fiber retrieval efficiency and required read pulse power for the set of red data points in (a).

waist at the focus, V is the cavity mode volume and ϵ_0 and $\hbar$ are constants. The linewidth of the distinct peaks is a function of cavity and transition linewidth. Here, we indirectly access this splitting by measuring the DLCZ read-out efficiency. Nevertheless, when scanning OD as shown in Fig. 6.1(b), the splitting follows the expected square-root trendline. The splitting is independent of the cavity finesse (measurement not shown here), which is expected, as g depends only on the cavity geometry.

When instead scanning the cavity resonance, the joint atom-cavity resonance is also expected to shift. Such an VRS absorption spectrum is depicted in Fig. 6.2(a) as a function of cavity detuning and read pulse detuning. The red points mark measured data points of highest retrieval efficiency for a given cavity detuning, nicely highlighting the correspondence between maximum absorption and maximum retrieval efficiency. Fig. 6.2(b) shows the corresponding efficiency of emitting a heralded read photon into the cavity mode, and (c) the read pulse power necessary to retrieve the stored excitation. We observe that the maximum efficiency stays almost constant,

while the power required to retrieve the excitation grows with detuning.

This study shows that the read-out process can be enhanced with the low-finesse cavity. The intrinsic (i.e. intra-cavity) retrieval efficiency in the presented measurements could be enhanced from $\approx 25\%$ without cavity to up to 70% with cavity. If one, however, includes the limited escape efficiency of the emitted photons from the cavity (55%) and the chopped lock setup (46% transmission), the count rate could not be improved. To increase the escape efficiency, the losses on the vacuum cell windows would have to be reduced, which constitute the major intra-cavity loss term in our system.

6.2 Cavity-enhanced Raman storage

After having investigated the emissive DLCZ memory, we now move to the absorptive Raman storage. Raman and EIT storage in hot vapors with cavity-enhanced noise suppression [153, 212] as well as Faraday-rotation and memory operation [213] was shown with light at the single photon level. However, cavity-enhanced Raman storage in cold atoms was not reported so far, to my knowledge.

The layout for this experiment is shown in Fig. 6.3. For this data, Zeeman optical pumping in the presence of a magnetic bias field was applied. The filter cavity is not used. First, the ensemble is prepared in $|g\rangle = |F = 2, m_F = 2\rangle$. An input probe couples off-resonantly to $|e\rangle = |F' = 2, m_{F'} = 1\rangle$ ($\Delta = -54\,\mathrm{MHz}$, 220 ns pulse duration (FWHM)) and is mapped to the second ground state $|s\rangle = |F = 1, m_F = 0\rangle$ by means of a strong coupling pulse in two-photon resonance with the probe (240 ns pulse duration). After a programmable delay, a rectangular co-propagating coupling pulse retrieves the stored excitation in forward direction. As opposed to the DLCZ scheme, input and output photons have equal polarisation and frequency. Therefore, the cavity naturally facilitates both the writing and reading stage. Horizontally-polarised probe light containing a few photons is injected into the cavity and stored in the cloud. To facilitate locking during the MOT loading phase, this weak probe is overlapped with lock light of horizontal polarisation on a 90:10 beam splitter. A chopper wheel (not

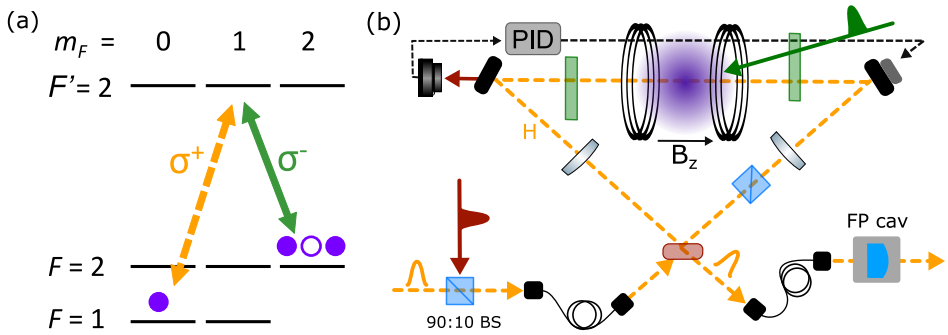

Figure 6.3: (a) Level scheme used for Raman storage. (b) Simplified setup layout for the cavity-enhanced Raman storage. For a complete legend of all the elements, please refer to Fig. 3.4.

shown here) ensures that the strong lock light does not reach the detector.

The memory was optimised in the following way. First, the probe light was set to a a detuning of $\Delta = -54\,\mathrm{MHz}$. Then, the reflection of this probe light from the empty cavity, i.e without atoms loaded in the MOT, was recorded while scanning the cavity resonance. This is displayed in Fig. 6.4(a), blue trace. As the cavity is almost impedance-matched (i.e. total passive round trip losses of 11% are comparable to the incoupling-mirror transmission of 13%), most of the light enters the cavity. When the atoms are then loaded into the trap (green trace), the cavity resonance shifts because the vacuum Rabi splitting induced by the atom-cavity coupling introduces a phase shift[2]. Storage is now performed by running the complete Raman sequence introduced before (with the cavity lock shifted to match the new reflection minima), and the coupling pulse detuning, power and wave shape are optimized for maximum storage efficiency. Fig. 6.4(b) shows the photon

[2]At the given detuning of $\Delta = -54\,\mathrm{MHz}$, residual absorption of $\approx 2\%$ (corresponding to an on-resonance OD of 5) should completely impedance-match the cavity and bring the reflection to zero. However, the probe light contained a small fraction of vertically polarised light which is almost completely reflected off the cavity, leading to a small offset. This was not known when recording this data.

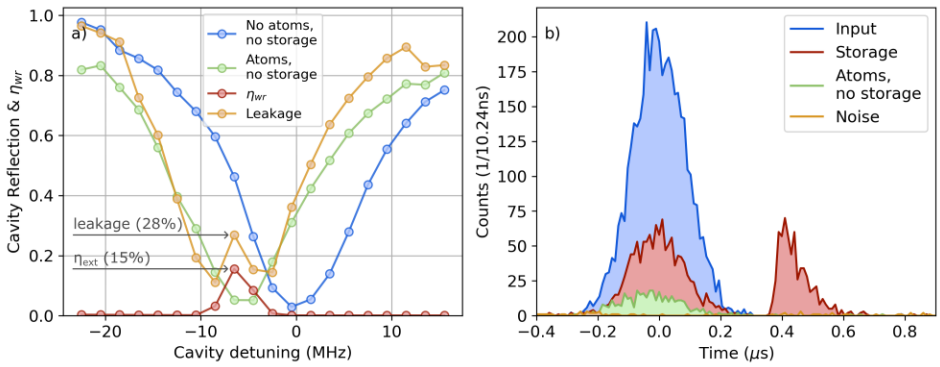

Figure 6.4: Cavity-enhanced Raman storage. (a) Reflection spectrum off the empty cavity (blue) and with atoms (green), and combined extra-cavity storage and retrieval efficiency η_{ext} (red) and leakage (yellow) as a function of cavity detuning from the probe frequency. (b) Typical histogram for optimized storage, corresponding to a detuning of $-6.5\,\mathrm{MHz}$ in panel (a).

histogram for storage under optimal conditions.

The maximum extra-cavity storage and retrieval efficiency amounts to $\eta_{\mathrm{ext}}^{\mathrm{max}} \approx 15\%$ (Fig. 6.4(a), red trace at $-6.5\,\mathrm{MHz}$). Here, η_{ext} is calculated as the ratio of re-emitted photons collected after the cavity vs. the number of input photons impinging on the cavity. The leakage (i.e. the part of the input light which is not absorbed and therefore reflected, yellow trace) should be minimal at this point and tend to zero. However, a local maxima arises, because the coupling beam facilitates the absorption of probe light, introducing additional absorption and effectively driving the cavity away from the impedance-matched condition. The measured residual leakage of $\approx$ 28% corresponds to a an atomic absorption of 25% per round trip (induced by the coupling beam).

As of now, $\eta_{ext}^{\mathrm{max}}$ is similar to the case without cavity enhancement. To estimate, however, the actual storage and retrieval efficiency into and out of the atom cloud, we need to consider the i) residual reflection from the cavity and ii) passive intra-cavity losses. To fully absorb the light, the

passive losses and the induced absorption need to match the outcoupling transmission. As explained in the former paragraph, the cavity is already impedance-matched without introducing a control beam. Any additional induced absorption can only push the cavity away from perfect matching. Furthermore, light circulating inside the cavity will be subject to passive round-trip losses (11%). Out of all the light that enters the cavity (1 - 0.28 = 72%), only a fraction $l_{\mathrm{in}} = 25\%/(25\% + 11\%) = 69\%$ will be absorbed in the memory. During re-emission, the fraction $l_{\mathrm{out}} = 13\%/(13\% + 11\%) = 54\%$ is outcoupled from the cavity. In effect, the intra-cavity memory efficiency amounts to $\eta_{int}^{\mathrm{max}} = \eta_{ext}^{\mathrm{max}}/l_{\mathrm{in}}/l_{\mathrm{out}} \approx 39\%$. This is already a factor two higher than η_{wr} without cavity enhancement.

To both absorb the full pulse and improve the escape efficiency l_{out}, a feasible way is to increase the in/out-coupling mirror transmission, at the expense of reduced cavity enhancement. Preferably, losses should simultaneously be reduced, which is however a more challenging task.

6.3 Discussion

In this chapter, cavity-enhanced DLCZ read out and Raman storage was shown. As the DLCZ memory is read-out on resonance, the coupling between the cavity mode and read-out transition results in vacuum Rabi splitting. Intra-cavity retrieval efficiencies of up to 70% were measured. For the Raman memory, perfect cavity impedance-matching is crucial to absorb as much light as possible into the memory. Intra-cavity storage and retrieval efficiencies of around 39% were measured. In both cases, the intra-cavity efficiencies could be increased by at least a factor two, compared to the heralded retrieval efficiency $\eta_{r|w}$ in DLCZ or total storage and retrieval efficiency η_{wr} for Raman storage without cavity, respectively. To translate this enhancement into an improved device efficiency, passive cavity losses need to be reduced. Additionally, the Raman memory can benefit from improved impedance-matching, by lowering the cavity finesse. In the future, it would be interesting to corroborate those phenomenological results by a more rigourous theory.

Chapter 7

Towards efficient atom-photon entanglement

The efficient generation of light-atom entanglement will be an enabling technology for a functional quantum network. This requires both efficient entanglement generation and low-loss photon transmission. In this chapter, I am proposing a toolbox for the implementation of efficient entanglement between a long-lived spin wave and a telecom photon. Photons would be generated via the DLCZ protocol and quantum frequency conversion would ensure low-loss transmission in the telecom C-band. Those capabilities could then be exploited in an experiment demonstrating hybrid matter-matter entanglement between the atomic cloud and a solid-state quantum memory based on a rare-earth doped crystal [27], which is operated by other members of the group. While I already implemented techniques to generate DLCZ photons at higher rates, and improved an existing conversion setup, a proposal to generate efficient light-matter entanglement is still under testing.

7.1 Proposed setup

Laser-cooled ensembles offer a way to implement highly efficient and long-lived light-matter entanglement via the DLCZ protocol [16, 65, 79]. As

explained and demonstrated in chapter 6, highly efficient storage can by achieved by combining an ensemble of moderate OD with a low-finesse enhancement cavity [130, 182, 208]. This cavity should enhance both the writing and reading process, and can at the same time suppress pulse noise which is not resonant with the cavity [65, 116]. To achieve long storage times, a lattice is needed to contain the atoms and prevent motional dephasing [64, 65]. Additionally, the storage system needs to be prepared for qubit storage. This could be two different intra-atomic sublevels as in polarisation entanglement [116], or two spin waves with different temporal evolution as in temporal multiplexing [151], for example. A special case is [157] which combines polarisation and time entanglement. However, there is no feasible way to engineer two co-existing spin waves on magnetic-field insensitive transitions, required for long-lived storage. Therefore, one has to either choose two distinct spin wave vectors, linked to two different emission directions [65], or address two different sub-ensembles within the same cloud [70, 71].

I am proposing a cavity-enhanced DLCZ memory, engineered for simultaneous resonance of both write and read photons, and simultaneous enhancement of two spatially separate cavity modes. The individual enhancement of the writing and reading stage for a single mode have already been successfully demonstrated, see chapter 4 and chapter 6. The path-entangled photons can then be retrieved from the cavity, converted to time-bin entangled photons in an imbalanced Mach-Zehnder interferometer, and frequency-converted to the Telecom C-Band. In order to synchronize this setup with other experiments, a one-dimensional dipole trap prolongs the atom lifetime.

I will first review the new cavity scheme, whose feasibility has been successfully tested (separately from the atomic cloud). Then, I explain the implementation of the dipole trap and finally, I describe the improved frequency-conversion setup [161, 214].

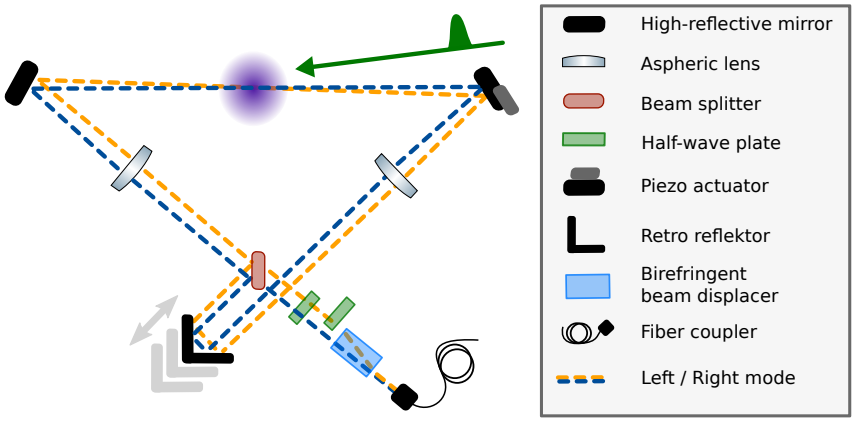

Figure 7.1: Simplified scheme of the two-mode cavity, exemplarily shown for the write photon modes. Locking beam and read photon modes are not shown for clarity. Initially, the two modes propagate parallel to each other and are focused onto the atoms to overlap in the MOT center. Length adjustment for simultaneous enhancement of write and read photon is achieved by a translation retroreflector.

7.2 The enhancement cavity

The setup described in the following was built on a testing breadboard and is not yet interfaced with atoms. The scheme is depicted in Fig. 7.1. The cavity has very similar length (80 cm) and therefore FSR ($\approx$ 375 MHz) as the old design, presented in chapter 3 or chapter 4. The novel aspect as compared to the cavity employed earlier is that it supports two distinct spatial modes (termed left and right mode) that are jointly focused onto the atoms. Those two modes can be used to path-entangle write photons emitted in the DCLZ process. In principle, the polarisation of the two modes inside the cavity can be set independently. In this example, they are both chosen horizontally. When exiting the cavity, the modes are parallel. They are then overlapped by flipping the polarisation of one of the modes and guiding them through a birefringent beam displacer (see appendix E for

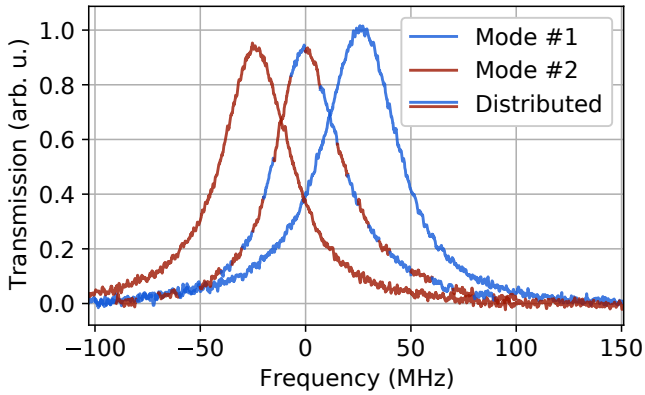

Figure 7.2: Cavity scan when sending light in either of the two modes, or distributed between both modes, demonstrating simultaneous spatial and frequency resonance.

details), after which they will occupy the same spatial mode. To avoid the use of a chopped lock setup, locking on a higher-order Laguerre-Gaussian mode was implemented (see again appendix E).

In order to enhance both writing and reading, the cavity needs to support both write and read photon frequencies. Those photons differ by approximately the ground state splitting of $\Delta \approx 6.8\,\mathrm{GHz}$, which corresponds to about $6.8\,\mathrm{GHz}/375\,\mathrm{MHz} \approx 18$ FSRs. The two frequencies reach resonance simultaneously for $\Delta \equiv n\mathrm{FSR}$. To find a common resonance, the cavity needs to be tunable in length by approximately an $1/18$th fraction of its lengths, so around 4.5 cm. This is achieved by a corner retroreflector mounted on a custom mount, allowing for course and fine translational adjustment (see appendix E for details).

To test the scheme, linearly polarised light at a variable polarisation angle is injected into the beam displacer. By tuning the polarisation angle, light can be injected into either the left or the right mode (or a combination of both). Fig. 7.2 shows the cavity transmission when the cavity is scanned in this situation. Sending light in either of the two modes demonstrates that

both of them can be tuned into spatial resonance simultaneously, by careful alignment of the lens positions and angle with respect to the beams (red or blue trace). When sending the same amount of light split between the two modes, they can be spectrally overlapped by moving the retroreflector (red-blue trace), demonstrating also simultaneous frequency resonance.

This proof-of-principle setup shows that two spatial modes can be addressed with a single cavity. Fig. 7.2 was measured for horizontally polarised input light in both modes, where the in-coupling mirror reflectivity is lower, leading to a Finesse of 9. For vertical light, the finesse increases to 35. In that case, it was more difficult to achieve simultaneous spatial resonance due to beam deviations, limiting the achievable finesse.

A similar setup for angular entanglement combining beam displacers and a low-finesse cavity was investigated recently [208]. However, in that scheme, the beam displacers together with polarisation optics and additional beam shapers were installed inside the cavity, which introduces large round-trip losses.

7.3 Implementation of a dipole trap

Having, so far, focused on the efficient generation of entanglement, we now tackle the experimental interrogation time. Due to gravity and residual motion, atoms are lost within 2-3ms after the MOT trapping potential has been switched off. When linking different setups, the data collection rates would greatly benefit from a prolonged interrogation time, which could allow for duty cycle synchronisation with the aforementioned Rydberg experiment (experimental time 200 ms), but also with other light sources and memories in the group. This shall be achieved with an optical dipole trap.

7.3.1 Theory of dipole trapping

This introduction follows the review article by Grimm *et al.* [215], pp. 1-10.

A dipole trap generates an attractive potential by exploiting the interaction of a strong light field with the induced atomic dipole moment. In a classical picture, the amplitude p of the dipole moment is related to the

electric field amplitude E by $p = \alpha E$, where α is the complex polarisability of the atom introduced in chapter 2. This creates an interaction potential given by the time-averaged product of $\mathbf{p}$ and $\mathbf{E}$

$$U_{\text{dip}} = -\frac{1}{2}\langle \mathbf{pE} \rangle = -\frac{1}{2\epsilon_0 c}\,\text{Re}(\alpha) I. \tag{7.1}$$

The force acting on the atom is derived from the potential gradient as

$$\text{F}_{\text{dip}}(r) = -\nabla U_{\text{dip}}(r) = -\frac{1}{2\epsilon_0 c}\,\text{Re}(\alpha)\nabla I(r). \tag{7.2}$$

This is a conservative force (as opposed to the dissipative force in MOT). As the light interacts with the atom, creating a dipole potential, it can also be absorbed and scattered. The scattering rate is given by

$$\Gamma_{\text{sc}}(r) = \frac{P_{\text{abs}}}{\hbar\omega} = \frac{1}{\hbar\epsilon_0 c}\,\text{Im}(\alpha) I(r). \tag{7.3}$$

Inserting α into eq. (7.1) and eq. (7.3) and assuming not too large detuning (i.e the driving field is still close to the atomic resonance, $\omega/\omega_0 \approx 1$) gives the following comprehensive formulas

$$U_{\text{dip}} = \frac{3\pi c^2}{2\omega_0^3}\frac{\Gamma}{\Delta} I(r) \tag{7.4}$$

$$\Gamma_{\text{sc}}(r) = \frac{3\pi c^2}{2\hbar\omega_0^3}\left(\frac{\Gamma}{\Delta}\right)^2 I(r). \tag{7.5}$$

The above formulism is valid only for the simple two-level atom. For multilevel atoms, possibly with sublevels, the picture becomes more complex. For alkaline atoms, and for a detuning much greater than the excited-state hyperfine potential ($\Delta'_{\text{HFS}} = 2\pi \times 496\,\text{MHz}$) the following formulas describe the ground state dipole potential & scatter rate for coupling of $|F, m_F\rangle$ with light of a given polarisation P ($P = 0, \pm 1$ for linearly and circularly $\sigma^{\pm}$

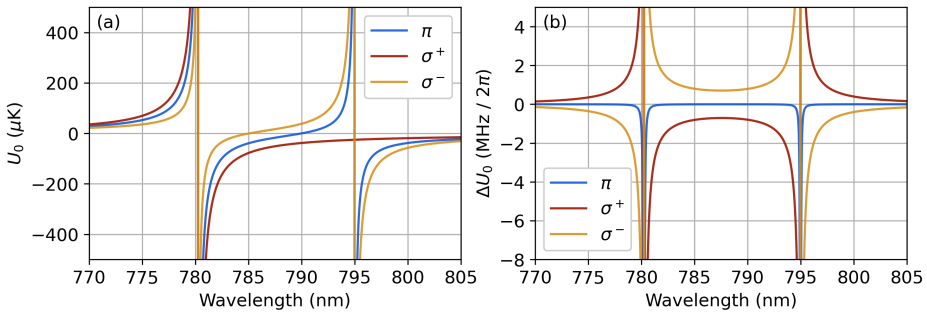

Figure 7.3: (a) Dipole potential for the $|F = 2, m_F = 2\rangle$ ground state, for different polarisations of the dipole trap light. (b) Relative ac Stark shift between the $|F = 2, m_F = 2\rangle$ and $|F = 1, m_F = 0\rangle$ ground states, which are the states employed in chapter 5, for different trapping light polarisations. Plotted for an atom sitting in the intensity maximum of a single trapping beam with 110 µm beam waist and a power of 250 mW.

polarized light)

$$U_{\text{dip}} = \frac{\pi c^2 \Gamma}{2\omega_0^3} \left(\frac{2 + P g_F m_F}{\Delta_{\text{D2},F}} + \frac{1 - P g_F m_F}{\Delta_{\text{D1},F}} \right) I(r). \tag{7.6}$$

$$\Gamma_{\text{sc}} = \frac{\pi c^2 \Gamma^2}{2\hbar\omega_0^3} \left(\frac{2 + P g_F m_F}{\Delta^2_{\text{D2},F}} + \frac{1 - P g_F m_F}{\Delta^2_{\text{D1},F}} \right) I(r). \tag{7.7}$$

$\Delta_{\text{D2},F}$ and $\Delta_{\text{D1},F}$ are detunings measured with respect to the energy splitting between a particular $F = \{1, 2\}$-level of the $^2S_{1/2}$ groundstate and the center of the excited state hyperfine manifold of either the D2 or D1 line, respectively. In Fig. 7.3(a), those potentials are mapped out for different trap light polarisations interacting with the $|F = 2, m_F = 2\rangle$ ground state, in the vicinity of the D2 and D1 lines of Rubidium. It is important to note that the dipole potential equals the energy shift of a state in the presence of the light field. If the light shifts differ for the ground and storage state, this leads to a relative level split. This is exemplarily shown in Fig. 7.3(b). Close to resonance and depending on the trap light polarisation, the differential

light shift can amount to many MHz, compared to an atom that does not see the trapping light at all. As atoms in a trap are spatially distributed, this inhomogeneous splitting leads to decoherence of the spin wave.

The scattering of the trap light induces heating. The heating power depends on the average scattering rate and the recoil energy as

$$P_{\text{heat}} = 2E_{\text{rec}}\bar{\Gamma}_{\text{sc}} = k_B T_{\text{rec}}\bar{\Gamma}_{\text{sc}}. \tag{7.8}$$

For harmonic potentials, this connects with the temperature increase as

$$\dot{T} = \frac{1}{3}T_{\text{rec}}\bar{\Gamma}_{\text{sc}}. \tag{7.9}$$

This formula also describes near-resonant scattering from, for example, optical pumping or DLCZ write attempts.

7.3.2 Optical setup

The dipole trap consists of a light beam of linear polarisation at 796.5 nm. It is derived from a Titanium-Sapphire laser (M-Squared SolsTiS), providing up to 1.5 W of output power at 795 nm. The light is switched with a single-pass AOM. Subsequently, 250 mW of power is coupled into a polarisation-maintaining fiber and delivered to the experiment. There, it is out-coupled and focused down to a beam waist of 110 µm at the position of the cloud. The light is retro-reflected, forming a one-dimensional pancake lattice. The dipole trap is incident at an angle of $\approx 10°$ with the photon mode[1]. All the beams (control beams, OP beam, dipole trap) are in-plane with the photon mode. As the trap light is close to resonance with the D1 line, the potential strongly depends on the $|F, m_F\rangle$-sublevel and light polarisation (subsection 7.3.1). For $|F = 2, m_F = 2\rangle$ and linearly polarised light, 250 mW of power forms a potential depth of $U_0 \approx 400\,\mu\text{K}$ according to eq. 7.6. For this estimate, it was assumed that the maximum intensity is four times

[1] In order to suppress atomic motion smearing out the spin wave profile, it would be beneficial to have a pancake lattice with a lattice vector parallel to the spin wave vector, i.e. roughly perpendicular to the control and photon modes [64, 147]. This is not the case in our experiment, but might be implemented in the future.

larger than the single-pass intensity due to constructive interference in the lattice. The theoretical trap frequencies are $\omega_r = 3.5\,\mathrm{kHz}$ in radial direction and $\omega_r = 540\,\mathrm{kHz}$ in axial direction.

7.3.3 Dipole trap performance

The performance of the trap is now tested, measuring atom lifetime and optical depth. For this, atoms are loaded in the MOT for 800 ms. To transfer the atoms more efficiently into the small dipole trap, the standard MOT loading is followed by a compressed-MOT phase (CMOT, 8 ms), a technique to temporarily enhance the atomic density. This is done by increasing the trap magnetic field gradient, leading to a smaller trap size and a compressed ensemble. The compressed ensemble is then loaded into the dipole trap, which spatially overlaps with the CMOT. Fig. 7.4(a) shows the decay of OD as a function of holding time. Within 30 ms, the fraction of the CMOT which is not loaded into the dipole trap dissipates. Afterwards, a 1/e atom lifetime of 480 ms and an OD of 5 at 200 ms is measured, sufficient to synchronise with other experiments in the group. A temperature of around 40 to 50 µK is measured by time-of-flight (TOF) absorption imaging, as shown in Fig. 7.4(b). We now investigate the effect of photon scattering of the near-resonant trap light. For an atom sitting in the intensity maximum of the dipole trap light, eq. 7.7 gives $390\,\mathrm{s}^{-1}$, so one event every 2.6 ms. This means that after a couple of milliseconds the spin polarisation of the ensemble will be mixed, as demonstrated in Fig. 7.5(a). For that measurement, the ensemble is prepared in $|F = 2\rangle$ (after CMOT, molasses and an extra offset of 10 ms to allow for the un-trapped parts of the cloud to disperse). This defines time zero on the x-axis. Then, the OD on this transition is measured for different holding times. If a small amount of optical pumping power is kept on constantly, the OD decays slowly (blue curve). However, if no optical pumping is applied after the initial reset, the OD decays quickly within $\approx 25\,\mathrm{ms}$, followed by a slower decay (green curve). Those atoms are not lost from the trap, as the OD can be restored by a short pumping pulse right before the OD measurement (red curve). This indicates that those atoms decayed to $|F = 1\rangle$ due to photon scattering of the dipole trap

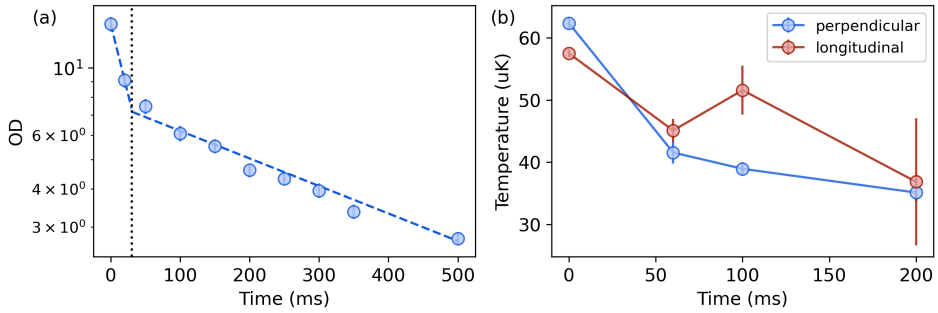

Figure 7.4: (a) OD and (b) Temperature as a function of holding time in the dipole trap. Time count starts after release from CMOT, molasses and state preparation. In (b), the temperature is measured by time-of-flight absorption imaging. A temperature is extracted both from the expansion in longitudinal and perpendicular direction.

light. Atoms on $|F = 1\rangle$ are invisible to the OD probe light. For holding times above 30 ms, a constant OD ratio of around 0.6 between those two curves is preserved. This seems to be the steady-state situation, as atoms are also allowed to scatter from $|F = 1\rangle$ and repopulate $|F = 2\rangle$. For this measurement, the OD was artificially lowered by reducing the dispenser current to resolve the effect better, but it seems to be a universal scaling independent of the initial OD.

While this scattering rate is large compared to far-resonant dipole traps, it is negligible when comparing it to the scattering induced by the writing attempts in DLCZ. In DLCZ, a portion of the atomic population undergoes constant Raman scattering at high rates (possibly in the mega-Hertz range), counting the writing, reading and re-pumping processes. This introduces heating and rapid atom loss, as experimentally observed in Fig. 7.5(b). Here, a DLCZ experiment is performed, and the write detection probability is recorded as a function of holding time. The first write attempt is sent right after CMOT, molasses and state preparation, without additional time delay, and at maximum dispenser current. For the blue trace, 1400 write pulses are

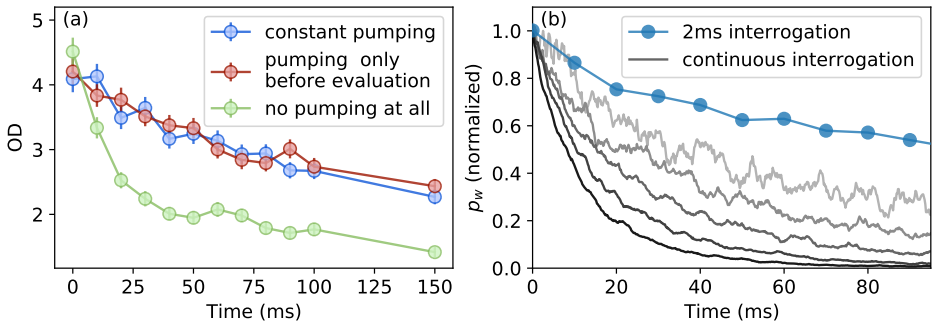

Figure 7.5: (a) OD as a function of holding time, for three different scenarios of optical pumping to $|F = 2\rangle$. Time count starts after release from CMOT, molasses, state preparation and an extra offset of 10 ms. (b) Normalized write photon detection probability p_w as a function of holding time, for 2 ms of interrogation and continuous interrogation. For 2 ms of interrogation, the write pulse energy was 2.3×10^{-12} J. For continuous probing, traces with different write pulse energy ranging from 1.4×10^{-13} J (light grey) to 2.3×10^{-12} J (dark grey) are shown. Time count starts after CMOT, molasses and state preparation.

sent at the usual repetition rate every 1.4 µs and at large write power, but only for 2 ms consecutively. The time of the first write pulse is scanned in steps of 10 ms. In this case, a high p_w is maintained, in agreement with the decay time of the OD. However, when probed continuously, p_w decays much quicker (grey traces). In contrast to the former measurement, those atoms cannot be pumped back anymore, they are lost from the trap due to heating. The effect is more pronounced for stronger write pulse energies (dark grey lines). In fact, the characteristic decay times of the traces in Fig. 7.5(b) are nearly inversely proportional to their respective write pulse power.

This limits the usage of dipole traps in protocols like DLCZ, when photons are to be generated at high rates for a prolonged period of time. The trap is still useful for single-photon storage protocols, for example the Raman or EIT protocols. It can also be successfully employed in DLCZ

when limiting the total amount of photon scattering per MOT cycle. This would be the case for a quantum repeater link with distant notes, where the rate is limited by the communication time. This scenario is similar to a recent experiment performed by Wang *et al.* [65]. In that experiment, the writing stage contained at most 400 trials, sent during 1.25 ms. If a write photon was detected, the excitation was stored for up to 1 s in a lattice trap, after which the atoms were re-trapped. If no write photon was detected in 400 trials, the atoms were re-trapped immediately.

The dipole trap can help to improve the holding time in the usual DLCZ sequence on shorter time scales, were the interrogation time could be improved from 1.5 ms to 4 ms. This led to a 3-fold gain in write counts. In this case, the CMOT stage would be skipped.

It is worth mentioning that it is possible to perform Zeeman optical pumping in conjunction with the dipole trap, and that the differential light shift broadening the transition is sufficiently small to perform storage under the presence of dipole trapping (as the coherence time is still limited by atomic motion). It is, however, very sensitive to the dipole trap polarisation. I experimentally verified that the dipole trap polarisation needs to be perfectly linearly polarised. If this is not the case, atoms are still trapped, but the spin wave decays rapidly and atoms are not pumped to the desired Zeeman state. This could be because of polarisation-dependent optical pumping effects of the trap light, redistributing the population.

7.4 Improved quantum frequency converter

The DLCZ-generated photons have a wavelength of 780.24nm, resonant with the D2 line of ^{87}Rb. This is non-optimal, as losses in fiber cables are as large as $4\,\mathrm{dB\,km^{-1}}$ at this wavelength. They reduce the transmission probability to only 40% after just 1 km.

For long-distance communication, the photons need to be converted to the telecom range. Quantum frequency conversion (QFC) combines established non-linear parametric conversion techniques [216] with strong noise filtering, such that the single-photon signal can be resolved with high SNR after

conversion. To that end, a conversion setup connecting to the telecom-C band at 1552nm had been developed by former PhD students Boris Albrecht and Nicola Maring [161, 214]. The non-linear frequency intermodulation was facilitated by a periodically-poled lithium niobate (PPLN) crystal and the light modes were travelling inside a waveguide engineered into the PPLN. The system performed well and produced remarkable results [29, 80]. However, the maximum fiber-to-fiber device efficiency was limited to $\eta_{\mathrm{dev}}^{\mathrm{max}} \approx 10\%$ in that system [80], whereas device efficiencies of up to 57% have been reported recently [82]. Additionally, the converted photons had a duration of only 20 ns [80]. For the envisioned hybrid experiment, combining the DLCZ source with a cavity-enhanced SPDC photon source, the photon duration will be given by the SPDC photons, which are around 10 times longer. Assuming a constant, broad-band noise background introduced by the pump field, this translates to a SNR which is 10 times lower. Therefore, the noise added by the converter needs to be reduced.

The target of this project was to increase the device efficiency and decrease the noise of the current converter. As for the efficiency, bottlenecks are the limited probe coupling efficiency into the waveguide (74%), transmission of the 780nm photons through the waveguide (70%), internal conversion efficiency ($\eta_{\mathrm{int}}{}^{\mathrm{max}} \approx 60\%$) and the filtering stage transmission (55%). As for the noise, the narrowest filter element was 220 MHz broad, still around 40 times wider than the photons we want to convert. Therefore, a new conversion crystal was implemented, and the filtering stage was re-designed.

7.4.1 A glimpse of non-linear frequency conversion theory

In non-linear frequency conversion, optical non-linearities are exploited to intermodulate the frequencies of input light to generate new frequencies at the output. A very good resource to achieve a deeper understanding of nonlinear optics is the text book by Boyd [216].

In general, light fields traveling in an optical medium induce electric dipole moments. This time-varying polarisation density P can be decomposed into

a Taylor series

$$\boldsymbol{P}(t) = \epsilon_0 \left(\chi^{(1)} \boldsymbol{E}(t) + \chi^{(2)} \boldsymbol{E}(2)^2 + \chi^{(3)} \boldsymbol{E}(t)^3 + ... \right) \tag{7.10}$$

where $\boldsymbol{P}$ has been assumed to be aligned and in phase with $\boldsymbol{E}$, as $\chi^{(n)}$ are scalar, which is true for an isotropic dielectric medium. The polarisation coefficients $\chi^{(n)}$ for $n > 1$ in turn act as a source term for electric fields, such that electric fields are generated at frequencies that correspond to the sum, difference or multiple of the input frequencies. Which process is the dominant one depends on the material susceptibilities (i.e. which non-linear coefficient is strongest) and on the phase-matching (i.e. momentum conservation). Our system performs difference frequency generation (DFG) of a probe photon at 780.24nm, which is converted to a telecom photon at 1552nm with the help of a strong pump at 1569nm, satisfying energy conservation. The phase matching condition for this process reads $\boldsymbol{k}_{\text{tel}} = \boldsymbol{k}_{\text{probe}} - \boldsymbol{k}_{\text{pump}}$. We exploit the $\chi^{(2)}$-nonlinearity in a lithium niobate ridge waveguide to mix those frequencies. The crystal is periodically poled (PPLN) to ensure quasi-phase matching in a co-linear configuration, which is then fine-tuned with temperature.

Based on the wave equation for electromagnetic propagation in materials and the above-mentioned Taylor expansion of the material polarisation density, the fraction of converted light compared to the input light can be calculated as a function of pump power P and length L

$$\eta_{\text{int}} = \eta_{\max} \sin^2(L\sqrt{\eta_n P}). \tag{7.11}$$

The parameter η_n is called normalized efficiency, and is usually given in units of $\text{W}^{-1}\,\text{cm}^{-2}$. The coefficient $\eta_{\max}$ takes into account experimental imperfections like losses or imperfect mode matching in the waveguide.

7.4.2 Noise processes

Noise generated by the strong pump can wash out any signature of the converted single photon. The noise processes of interest for our application are depicted in Fig. 7.6. The transmitted pump itself is the strongest source

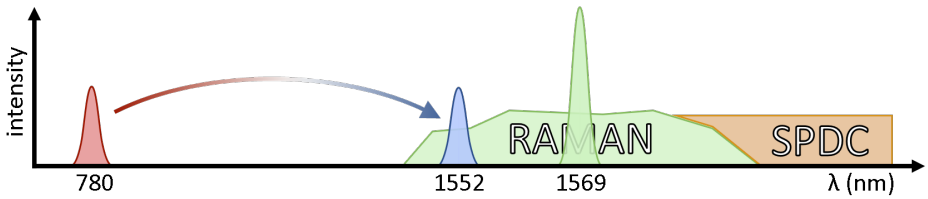

Figure 7.6: Dominant noise processes in our QFC implementation, where light at 780nm is converted to 1552nm by means of a pump at 1569nm. Spontaneous Raman noise is generated around the pump center frequency, while SPDC noise appears only for longer wavelengths.

of noise. However, as it is not spectrally overlapping with the converted photon, it can be filtered out by interference filters. Inside the waveguide, a pump photon can spontaneously split into photons of longer wavelengths, called SPDC noise. This is not of concern here, as the pump wavelength is yet longer than the converted wavelength and can easily be filtered. However, broadband Raman noise that originates from inelastic interaction with the phonon modes in the $LiNbO_3$ is generated to both sides of the pump center frequency[2]. The strength of this Raman noise is linked to material properties of the $LiNbO_3$ and can extend up to 21 THz from the central frequency [217], while our converted photon is only 2.1 THz away. In order to suppress this noise, narrow-band filtering based on Bragg gratings or optical resonators needs to be applied.

7.4.3 Implementation of the new non-linear crystal & improved noise filtering

After an introduction to optical conversion and the particular noise processes in our system, we now explain which changes were made to improve photon yield and noise suppression.

[2]Such Raman noise is already generated in the laser amplifier and optical fiber connecting to the experiment. It is filtered out before the waveguide by interference filters.

Improved photon conversion The conversion chip which implements the waveguide is at the heart of the setup. As mentioned in the introduction, a new chip from NTT (WH-0780-000-A-C-C-TEC) was introduced to improve coupling losses and internal conversion efficiency. This chip was originally designed for sum-frequency generation from 1560nm to 780nm, but can be tuned with temperature to satisfy the phase-matching condition for our wavelengths. The 34 mm long chip carries six ridge waveguides with slightly different geometries and poling period to be able to optimize mode- and phase matching. It is anti-reflection coated for all wavelengths involved in the process, and is cut at an angle of 6 ° to avoid internal reflections. It is mounted onto a Peltier element for temperature stabilisation (controlled by a PTC10 from SRS).

The probe light is coupled out from a single-mode PM fiber, directed to the waveguide and incoupled with an aspheric, achromatic lens (M15-37 from S&K). A combined incoupling and transmission efficiency of 89% is achieved for the 780nm probe, which is a factor two larger than for the previous implementation (44% [29]).

The pump light is overlapped with the probe light on a dichroic mirror, before it is also guided to the waveguide. After coupling also the pump beam to the waveguide (around 70% coupling efficiency), the phase-matching needs to be tuned to ensure optimal conversion. For this, around 1.4 mW of probe at 780nm is injected, together with ≈ 100 mW of pump light. The probe light at the output of the waveguide is then measured as a function of waveguide temperature, see Fig. 7.7(a). A dip in the power of the transmitted probe indicates efficient conversion of this light to the target wavelength. The pump light is filtered with a bandpass filter centered at 780nm (3nm FWHM), and a shortpass filter with 1000nm cut-off. A depletion of the probe is found for around 28 °C, indicating conversion to the telecom frequency (blue trace). For lower temperatures, an increase of the probe signal strength is observed beyond the injection level, which is also present at the output when the probe light is blocked (red trace). This is attributed to weakly phase-matched SHG light at around 785 nm. Such light can be filtered out. However, inside the waveguide it might decay into two SPDC photons of longer wavelength, generating broadband noise at telecom. This hypothesis

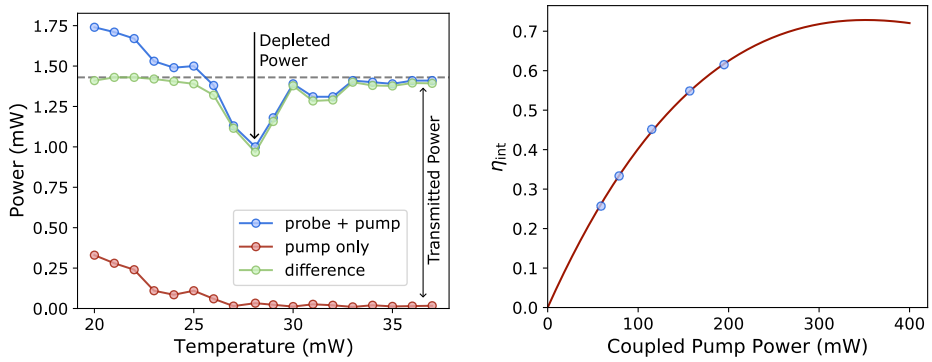

Figure 7.7: (a) NIR power measured after WG #6 as a function of waveguide temperature. Around 1.4 mW of probe at 780nm is injected. For the correct temperature, a depletion of the probe is observed. Pump power is ≈ 100 mW. (b) Internal conversion efficiency of waveguide #4 as a function of coupled pump power, measured after the waveguide.

has not been confirmed yet.

Next, the conversion efficiency was measured as a function of pump power, see Fig. 7.7(b) [3]. This internal conversion efficiency η_{int} is calculated as the depleted power (depth of the dip in panel (a)) compared to the transmitted power when the pump light is blocked. Independent direct measurements of the converted light at 1552nm are in good agreement with this data. The data was fitted with eq. 7.11, yielding $\eta_{\text{max}} = 73\,(1.7)\,\%$ and $\eta_n = 61\,(2.2)\,\%/\text{W}/\text{cm}^2$. This performance is very similar to the previous waveguide [80], so η_{int} could not be improved. However, the device efficiency is almost a factor two larger due to the reduction of incoupling- and transmission losses mentioned above.

[3]The waveguide is multimode for 780nm, such that optimal mode overlap (for optimal conversion) between the pump at 1569nm and the probe at 780nm requires some fine-tuning.

Improved noise filtering The former setup provided sufficient filtering to demonstrate non-classical correlations between a converted DLCZ write photon of 20 ns duration and a stored spin wave [80]. However, the overall transmission of the filtering stage is limited to 55%, and the noise floor is yet too high to convert the 200 ns-long photons from a cavity-enhanced SPDC source [27] Therefore, both the transmission and noise suppression of the filtering stage needs improvement.

Formerly, the filtering consisted of bandpass filters centered around 1550nm (9nm FWHM) to filter the strong pump, combined with an etalon to filter broadband Raman noise (220MHz FWHM, 4 GHz FSR) [214]. A fiber Bragg grating (FBG, 2.5GHz FWHM) was used to cut out exactly one transmission peak of the etalon. First, it is necessary to quantify the noise with the new waveguide, and compare to the former waveguide. The relevant figure-of-merit is $\mu_1 = \mu_{\text{in}}/\text{SNR}$, which specifies the number of input photons (to the waveguide), μ_{in}, required to achieve a signal-to-noise ratio (of the converted photon), SNR, of 1. This number should be as small as possible. It was measured to be $\mu_1 \approx 2.2 \times 10^{-3}$ [80], for a specific value of the pump power corresponding to around 50% of internal conversion, and for a photon with duration 20 ns (FWHM). With the new waveguide (but sticking to the above-mentioned parameters of conversion efficiency and detection window, and with the same filtering in place) I achieve a very similar $\mu_1 \approx 2.4 \times 10^{-3}$. I conclude that the new waveguide is slightly more noisy than the old one, given that the improvements in passive losses should have increased the SNR, and correspondingly μ_1, for the same noise floor. This underlines the need for an improved filtering stage.

The residual noise leaking through the filters is given by the linewidth of the narrowest filter element, which used to be the etalon filter (220MHz FWHM). Given that the photon linewidth is below 10 MHz, the noise filtering can be improved by replacing the etalon with a more narrowband cavity filter. A new monolithic Fabry-Perot filter was built, following the filter design described in chapter 3 for photons at 780nm. The linewidth is estimated to be $\approx$ 23.5 MHz, at a finesse of 680 and FSR of 16.2 GHz. The filter transmission reaches 96% on resonance (80% fiber-to-fiber device efficiency including fiber coupling and a mating sleeve). This filter is around nine-times

narrower in linewidth than the etalon filter used before, so a noise reduction of the same factor is expected. Indeed, when experimentally comparing the noise counts that leak through the etalon filter with the leakage through the new Fabry-Perot filter, the noise supression is eight-times larger, which is in good agreement with the theoretical value. Exchanging the lossy fiber Bragg grating by a device with larger transmission could further improve performance, both in terms of overall transmission and SNR.

7.5 Summary & conclusion

In summary, I showed the feasibility of a novel cavity design, which simultaneously addresses two distinct angular modes in a low-finesse cavity. This might allow for the generation of efficient path-entanglement between a photon and a stationary spin wave. Subsequently, I installed a dipole trap to prolong the interrogation time of the DLCZ memory. At high repetition rates, this proved difficult due to the heating induced by the DLCZ write beam. This is nevertheless a feasible pathway, as the repetition rate in future quantum repeaters is limited by the communication time. Finally, I showed that improvements to an already existing QFC setup could increase its device efficiency by a factor two, while reducing pump noise by a factor eight. Combining those results will, in a next step, allow to experiments towards hybrid matter-matter entanglement between the atomic cloud and a solid-state quantum memory based on a rare-earth doped crystal.

Chapter 8

Conclusion & Outlook

The goal of this thesis was to investigate several approaches for an improved repeater. The initially proposed quantum repeater architecture outperforms direct transmission of quantum information, but the predicted rates are still too low for practical purposes.

The scheme proposed by Duan, Lukin Cirac and Zoller (DLCZ) [16] builds on probabilistic light-matter entanglement stored as single collective excitations in cold atomic ensembles. Only one atomic excitation can be stored at a time. This results in some intrinsic limitations. First, the repetition rate at which connection attempts are performed in the network is limited, as only one excitation can be stored at a time. Second, the probabilistic nature of entanglement generation in the DLCZ protocol limits the generation probability. This is because the probability to create multiple excitations increases with generation probability. Third, strong light-matter interaction for efficient storage requires large clouds with high optical depth, whereas the spin wave retrieval from a DLCZ memory requires the atomic cloud to be short due to a phase mismatch.

In this thesis, different proposals to improve the original scheme were tested. A cold atomic cloud of Rubidium-87 serves as the light-matter interface. In chapter 4, a time-multiplexed DLCZ quantum memory was developed. Storing a large number of individual modes is important, as

the rates at which entanglement is created in the elementary repeater link scales linearly with the number of modes. By combining the interface with a low-finesse cavity and manipulating the phase evolution of the collective excitation through controlled inhomogeneous broadening, ten temporal modes were stored while maintaining strong quantum correlations. In chapter 5, a scheme that combines a quasi-deterministic photon source with a quantum memory was investigated. Deterministic photon creation prevents the generation of multi-photon states even at high generation probabilities, allowing for larger entanglement rates. However, photons generated by most deterministic sources such as quantum dots or molecules cannot be stored efficiently in atomic quantum memories, as the bandwidths are large and the emission lines do not naturally correspond to atomic absorption lines. In our approach, atoms in a second cloud of Rubidium-87 were excited to a Rydberg level. Strong dipole-dipole interactions prevent the excitation of more than one atom to the Rydberg level, leading to the creation of a single collective Rydberg excitation. The excitation was later retrieved as a single narrow-band photon resonant with the D2 line of Rubidium. This photon was then stored in the light-matter interface, which was operated as an absorptive memory based on Raman storage. The non-classical statistics of the single photon were well-maintained after storage. In chapter 6, cavity-enhanced memory read-out was investigated. This is relevant, as the entanglement rates in quantum repeaters scale strongly with memory efficiency. Using a cavity to enhance light-matter interaction allows for high retrieval efficiencies even with smaller ensembles. This is particularly important in the DLCZ scheme, where a phase mismatch prevents the efficient retrieval of a spin wave from large ensembles. The intrinsic retrieval efficiency could be enhanced from 25 to around 70% by the cavity, and vacuum Rabi splitting was observed. The same cavity also improved the storage efficiency of the Raman protocol, which to our knowledge constitutes the first demonstration of cavity-enhanced Raman storage in cold atoms. Finally, in chapter 7, ongoing work towards the efficient creation of entanglement between a spin wave and a telecom photon was documented. Creating entanglement between disparate systems will aid the development of functional, hybrid quantum infrastructure in the future. In this work, a novel approach to cavity-enhanced DLCZ storage is

combined with an optical dipole trap and quantum frequency conversion to the telecom C-band at 1550nm, where much higher rates can be achieved as transmission losses are reduced.

While this thesis was being written, another experiment was conducted which is not included here. In the experiment, the interface was used to generate non-classical states of light with the DLCZ scheme. Depending on the pump power in the *writing* stage, the *read* field contained a variable amount of multi-photon components. This light was used to investigate the response of the blockaded Rydberg medium to non-classical light, constituting the first experiment probing the interaction between non-classical light and a strongly non-linear Rydberg system. A manuscript is under review.

These results present substantial steps towards memory-based quantum repeaters. Yet, the system needs further improvements. The memory lifetime in our system is not yet sufficient to connect quantum nodes at a distance. The longest lifetime measured by us was around 120 µs, limited by motional dephasing. Incidentally, the short storage time did not prevent the demonstration of capabilities such as multiplexing [126] or efficient storage. An optical lattice in combination with ac Stark shift cancellation allows for storage times of seconds [64, 65].

The intrinsic DLCZ memory efficiency of up to 70%, albeit not yet unity, is not too far from the record values reported in the literature for atomic memories [53–57]. An interesting research direction to pursue further could be cavity-enhanced Raman storage, which promises broadband and long-lived photon storage. To extract photons from the cavity more efficiently, intra-cavity losses need to be reduced.

Another crucial feature is multi-mode storage. Multiplexing in the temporal domain, as demonstrated in chapter 4, is important for cold atomic memories, as frequency multiplexing is difficult to engineer due to the absence of inhomogeneous broadening. The number of stored modes was limited by the memory lifetime and the noise introduced by dephased spin waves. To increase the mode number, the noise could be further reduced by increasing the finesse of the enhancement cavity [126]. This approach is also compatible with spatial or angular multiplexing [70, 71].

In the near future, our goal is to prepare the interface for integration with

diverse quantum systems. For this, a necessary condition is indistinguishability of photons originating from those systems. This enables photon-photon interference, which is at the heart of Bell-state measurements for entanglement creation and -swapping. When combining photons from different systems, indistinguishability becomes a challenge, as is the case in a hybrid network. Currently, we are probing the indistinguishability of photons generated by the DLCZ memory and the Rydberg photon source, two promising candidates for quantum repeater nodes and quantum processing notes. The indistinguishability is asserted in a Hong Ou-Mandel (HOM) interference experiment [199]. A similar experiment was formerly performed in our group, performing HOM between Rydberg-generated photons and a weak coherent state [193]. First results with two single photons have been obtained while finalizing the thesis manuscript, showing an indistinguishability of more than 90% for the two photons. The manuscript is in preparation. In a next step, we would like to extend this idea and show HOM interference between photons from the DLCZ memory and an SPDC source. In the SPDC source, operated by another member of the group, the spontaneous decay of a photon at 426nm produces a non-degenerate pair of photons at longer wavelengths. One photon is at 606nm, a wavelength compatible with a solid-state memory based on Praseodymium, and the second photon is at 1550nm, allowing for long-distance transmission [27]. The *write* photon of the DLCZ source will be frequency-converted to 1550nm to interfere with the telecom photon. This will require frequency-stabilised lasers, and Fourier-limited single photons with identical wave shape and wavelength. One could imagine an extension of this experiment where the visible photon is stored in another memory to show correlations and eventually matter-matter entanglement between the laser-cooled cloud and a solid-state system.

Compiling the literature review for this thesis, I became aware of the remarkable advancements in the field of quantum light-matter interfaces since I started working on my PhD. These advancements owe their success to the work and dedication of many great minds, and also the investment of a significant amount of resources. I hope that my modest contributions to the field of laser-cooled quantum memories and quantum frequency conversion devices, which were summarized in this chapter, have expanded

the understanding of these promising platforms for long-distance quantum communication.

Appendix A

Additional information on chapter 3

A.1 Physics of optical resonators

Both our noise filters and enhancement cavity rely on constructive and desctructive interference of light in an optical resonator. The following description is based on the text book *Lasers* by Siegman [218].

The round trip optical path length of the resonator is l_{eff}. For example, a linear resonator filled with a medium of refractive index n and length l has $l_{eff} = 2ln$. A fraction R_i of the intensity of an incident light is reflected on each mirror. We rewrite this in "delta-notation" as $\delta R_i = \ln(1/R_i)$, such that $R_i = e^{(-\delta R_i)}$. This notation has the advantage that losses can be summed up in the exponent, instead of being multiplied. Additionally, light can undergo extra dissipative losses L_j on the mirror surfaces, or absorption & scattering in the medium (as a function of distance travelled). This is quantified by intensity loss coefficients α_k, often given in 1/cm. The total net round trip loss term is $g_{\mathrm{rt}} = e^{(-\delta c)}$, with δc

$$\delta c = \delta R + \delta L = \sum_i \delta R_i + \sum_j \delta L_j + \sum_k \alpha_k l_k. \tag{A.1}$$

A light field with intensity I_{inc} and amplitude $|E_{inc}| = \sqrt{I_{inc}}$ is incident on an optical resonator. A fraction $\sqrt{1 - R_{\mathrm{in}}}$ of the incident field enters the resonator. It then travels one round trip and interferes with itself. The relative phase shift acquired by the light inside the resonator is

$$g(\omega) = e^{-j\omega l_{eff}/c} \tag{A.2}$$

In the steady-state case, the total field building up inside the resonator is composed of the light entering the resonator, interfering with the circulating field from one round trip ago

$$E_{\mathrm{circ}} = j\sqrt{1 - R_{\mathrm{in}}}E_{\mathrm{inc}} + \sqrt{g_{\mathrm{rt}}}g(\omega)E_{\mathrm{circ}}. \tag{A.3}$$

Here, the transmitted field acquires a phase given by the imaginary unit j, while the circulating field does not. The circulating field acquires a phase $g(\omega)$ and undergoes the round trip loss $\sqrt{g_{\mathrm{rt}}}$ before interfering with the injected light again. E_{circ} is defined right after the incoupling mirror.

Similar formulas can be found for the reflected and transmitted fields. The transmitted field is simply the circulating field (again, at the position of the incoupling mirror), propagated all the way to the outcoupling mirror and being transmitted

$$E_{\mathrm{trans}} = j\sqrt{1 - R_{\mathrm{out}}}\sqrt{g_{\mathrm{rt},0}}g(\omega)_0 E_{\mathrm{circ}}, \tag{A.4}$$

where $g_{\mathrm{rt},0}$ ($g(\omega)_0$) are the losses (phase evolution) from incoupling to outcoupling (as opposed to the net round trip losses).

The reflected field is composed of the incident field initially reflected off the cavity, interfering with the circulating light leaking out of the cavity backwards.

$$E_{\mathrm{refl}} = \sqrt{R_{\mathrm{in}}}E_{\mathrm{inc}} + j\sqrt{1 - R_{\mathrm{out}}}(\sqrt{g_{\mathrm{rt}}}g(\omega)/\sqrt{R_{\mathrm{in}}})E_{\mathrm{circ}}. \tag{A.5}$$

Again, the circulating light undergoes losses $\sqrt{g_{\mathrm{rt}}}$ on its round trip, corrected for the final reflection off the incoupling mirror. Instead, it is transmitted,

acquiring a phase j. In conclusion, the formulas used in the following to predict the cavity performances are

$$E_{\mathrm{circ}} = jE_{\mathrm{inc}}\frac{\sqrt{1-R_{\mathrm{in}}}}{1-\sqrt{g_{\mathrm{rt}}}g(\omega)} \tag{A.6}$$

$$E_{\mathrm{trans}} = j\sqrt{1-R_{\mathrm{out}}}E_{\mathrm{circ}}\sqrt{g_{\mathrm{rt},0}}g(\omega)_0 \tag{A.7}$$

$$E_{\mathrm{refl}} = 1/\sqrt{R_{\mathrm{in}}}\frac{R_{\mathrm{in}}-\sqrt{g_{\mathrm{rt}}}g(\omega)}{1-\sqrt{g_{\mathrm{rt}}}g(\omega)} \tag{A.8}$$

A.2 Details of filter cavity design

Investigation of old filters For the old cavities, a Finesse of 255 was measured. When on resonance, around 50-55% of light is transmitted, while some 20% of light is reflected. The reason for this high back-reflection can be either bad mode-matching or an imbalanced cavity (i.e. the back-reflected loss of circulating light through the incoupling mirror does not equal the remaining round-trip losses).

We can try to model the experimental parameters. Different values for α are found in the literature. Depending on the manufacturer, they range from $0.0015\,\mathrm{cm}^{-1}$ (Schott) to $0.01\,\mathrm{cm}^{-1}$ (Hikari). The host material used for the old cavities is unknown, so we can only guess. For the reported reflectivity (99%), $\alpha = 0.0027\,\mathrm{cm}^{-1}$ describes best the measured cavity finesse of 255. Under those conditions, one could hope for a maximum transmission of 67%. However, only 3.5% of the light is reflected, not matching the observations. To make the calculations match the observations, one would have to increase losses and introduce additional imbalance of the mirror reflectivity to increase reflection.

This calculation does not take into account mode-matching, which, in a separate estimation based on the mode-mismatch of the cavity mode (assumed to be a Gaussian TEM_{00} mode) and the input beam, should not be larger than 5-10%. However, small inhomogeneties in the host material can distort the mode. If this is the case, interference will not be perfect and a greater part of the light is reflected off the cavity in the first place.

Glass	**Suprasil® 3001**	FS-LO-U	FS-LO-U
Substrate quality	**Best**	Standard	Standard
Surface quality	**Best**	Standard	Best
Cavity transmission (%)	**94.5**	92.6	91.3

Table A.1: Transmission for different substrate qualities and surface qualities.

In conclusion, the best strategy to improve transmission is to change the host substrate. For the right choice, this can simultaneously improve passive transmission (lower α) and mode distortion (lower impurities and higher homogeneity). Additionally, the coating should be optimised for internal reflection.

Design consideration for new filters Based on the above formulism, I simulated the performance of the new filters. This is plotted in Fig. A.1. We decide to order from Laseroptik, and choose a reflectivity of 98.8% and a readily available substrate of 6.35mm center thickness. The simulation assumes $\alpha = 0.0005\,\mathrm{cm}^{-1}$. For those parameters, we expect around 93.4% transmission, with finesse and linewidth of 252 and 64.7 MHz, respectively. Those values are also listed in Table 3.1.

Results The main results are already documented in Table 3.1 and will not be repeated here. However, I would like to give some additional insights, highlighting the importance of the choice of substrate.

In order to understand if the substrate or the surface would be the limiting factor, we asked for different combinations of substrate and surface qualities to be able to compare their performance. This is documented in Table A.1. We learned that all combinations perform substantially better than the old filters based on an unknown BK-7 glass. For the same substrate, better polishing did not improve transmission. From this, we conclude that choosing the appropriate substrate was vital for our application.

The filter has to be tuned by temperature. The effective cavity length is

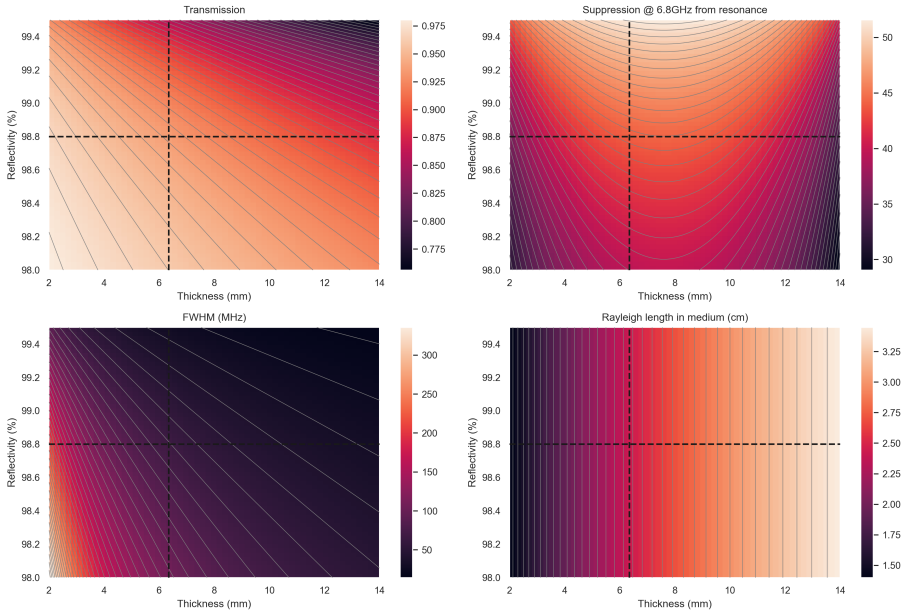

Figure A.1: Simulation of filter transmission, suppression, linewidth and Rayleigh range as a function of mirror reflectivity and substrate thickness. Dotted lines symbolise our choice of substrate thickness and reflectivity.

a function of both the change of refractive index and the thermal expansion of the material. The cavity resonance shifts like [164]

$$\frac{\Delta\nu}{\Delta T} = -(\alpha + \frac{1}{n}\frac{\delta n}{\delta T})\nu. \tag{A.9}$$

For fused silica, we find $\alpha = 5.1e-7$ and $\delta n/\delta T \approx 1e-5$. This gives $2.84\,\mathrm{GHz\,K^{-1}}$. We measure a tunability of $2.6\,\mathrm{GHz\,K^{-1}}$, which is in good agreement with the predicted value. For a cavity FSR of 16.2 GHz, this results in a full FSR scan every 6.3 K.

As shown in Fig. 3.5, the new cavity shows considerably less birefringence. This might be because Suprasil® 3001 is certified as an isotropic substrate

(the homogeneity of most substrates are only specified in one dimension). This should also help to reduce stress-induced birefringence. Birefringence is also reduced by carefully mounting the lens in its holder. The holder is essentially a bulk copper piece with a cavity the diameter of the lens. The lens slides into this cavity and is held in place from the back with a second copper piece. The birefringence increases when the lens is mounted more tightly, demonstrating the influence of stress-induced birefringence. Birefringence was not investigated for FS-LO-U.

Appendix B

Additional information on chapter 4

B.1 Choosing the correct write pulse duration

Two important figures of merit are closely linked to the write pulse duration: the cavity enhancement and the readout efficiency. As mentioned in the main text, the write pulse duration is set to a full-width at half-maximum (FWHM) of $\Delta t_W = 266\,\text{ns}$. This duration is chosen considering both cavity enhancement and readout efficiency, as explained in this section.

Cavity Enhancement The write pulse temporal duration is inversely proportional to its frequency spectrum. However, only the part of the write pulse spectrum that overlaps with the cavity transmission spectrum can be effectively enhanced. This effect is shown in Fig. B.1 where we compare the write photon detection probability p_w for different pulse lengths, scanning the cavity detuning. For long (narrow-band) write pulses, the cavity enhancement spectrum is given by the cavity transmission spectrum. However, when decreasing the write pulse duration, its spectrum broadens. In this case the cavity transmission and write pulse spectra get convoluted, and the cavity enhancement spectrum becomes broader, showing a lower maximum

enhancement. From this measurement we infer that the write pulse has to be longer than ≈ 100 ns in order to obtain the maximum cavity enhancement for the current cavity setup.

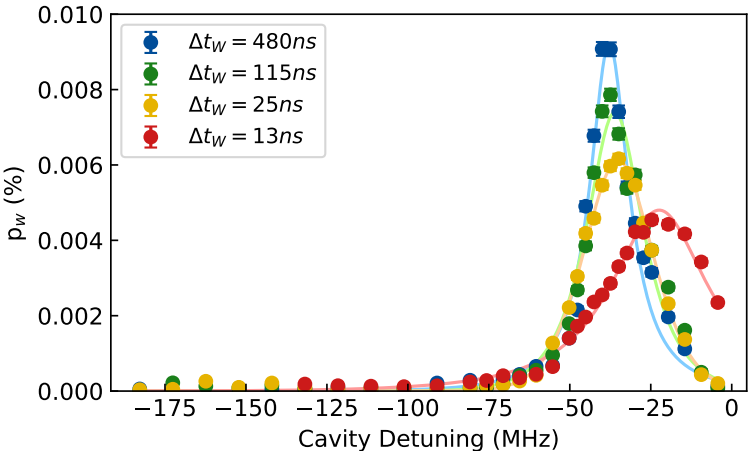

Figure B.1: Write photon detection probability as a function of the cavity resonance frequency (scanned by changing the cavity piezo voltage). The different colors represent different durations Δt_W (FWHM) of the write pulse. The zero point in the cavity detuning corresponds to the center of the $|s\rangle - |e\rangle$ transition. The tendency for shorter pulses to shift towards zero detuning is attributed to increasing frequency overlap (and therefore increasing interaction) of the write pulse with the $|s\rangle - |e\rangle$ transition. Write pulse energy is constant for all traces.

Readout efficiency The write pulse duration also affects the controlled rephasing echo profile. When the write pulse temporal duration is comparable to or longer than the spin wave rephasing profile (which is given by the applied inhomogeneous broadening), excitations generated at different times within the same write pulse will rephase at different times. As opposed to the DLCZ protocol in a homogeneously broadened medium, it is not possible anymore to retrieve the entire spin wave at a specific retrieval time.

Therefore, the retrieval efficiency $p_{r|w} = p_{w,r}/p_w$, considering all the possible spin wave creation times, will decrease. This can be seen in Fig. B.2 where we compare the echo profile for different write pulse lengths. From this measurement we infer that the write pulse cannot be longer than ≈ 100 ns in order to obtain decent retrieval efficiency for the current inhomogeneous broadening.

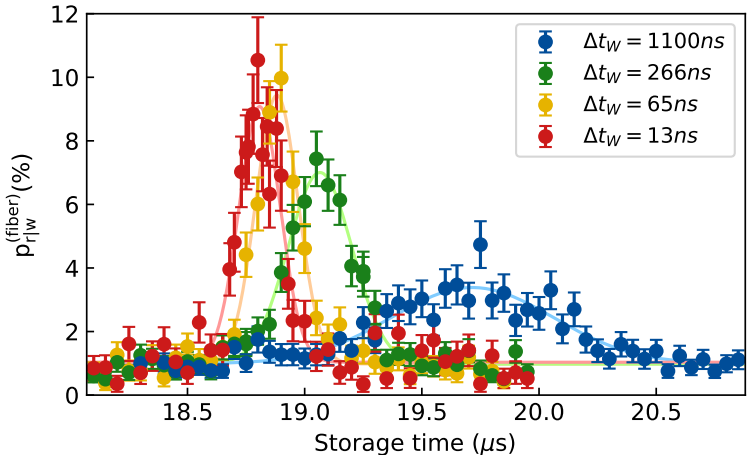

Figure B.2: Probability to collect an heralded read photon into the read fiber as a function as a function of storage time. The different colors represent different durations of the write pulse, which have an impact on the width and amplitude of the rephasing peak. The peaks are slightly shifted in time for technical reasons. Maximum efficiency for $\Delta t_W = 266$ns is slightly lower than in the main text because experimental conditions were not yet optimum.

While the cavity enhancement is the highest for longer write photons, the spin-wave echo shows a higher retrieval efficiency for shorter write pulses. The write pulse that we choose is a trade-off between enhancement and efficiency. While this would indicate $\Delta t_W \approx 100$ ns, we use a slightly longer write pulse of $\Delta t_W = 266$ ns as longer rephasing peaks are less affected by fluctuations in rephasing time (see below).

B.2 Theory model for the cavity-enhanced write photon emission

As explained in the supplemental material of [80], when describing theoretically the write and read photon detection probabilities in the presence of spin wave dephasing, one has to consider both the coherent and the incoherent emission processes. This can be described by the following equations:

$$p_w = p\eta_w \tag{B.1}$$
$$p_r = pp_{r|w}^{int}\eta_r + N_s[1 - p_{r|w}^{int}]\beta_r\xi_{eg}\eta_r \tag{B.2}$$
$$p_{w,r} = pp_{r|w}^{int}\eta_w\eta_r + p\eta_w N_s[1 - p_{r|w}^{int}]\beta_r\xi_{eg}\eta_r \tag{B.3}$$

where p is the spin wave excitation probability, $\eta_{w(r)}$ is the write (read) photon total detection efficiency, $p_{r|w}^{int}$ is the intrinsic readout efficiency, $\beta_{w(r)}$ is the fraction of solid angle corresponding to the write (read) photon collection mode, $N_s = p/\beta_w$, is the total number of created spin excitations, and ξ_{eg} is the branching ratio corresponding to the read photon transition.

Let's now consider the situation with multiple writing temporal modes and subsequent readout of a specific mode at the rephasing time of the corresponding spin wave. The read photon emission contributions from the rephased spin wave can be described by Eq. B.1-B.3. However, in this situation one also has to consider the incoherent read photon emission from spin wave modes that are not rephased. The photon contributions to p_r and $p_{w,r}$ from these dephased modes is:

$$p_r^{deph} = N_s^{deph}\beta_r\xi_{eg}\eta_r \tag{B.4}$$
$$p_{w,r}^{deph} = p\eta_w N_s^{deph}\beta_r\xi_{eg}\eta_r \tag{B.5}$$

where $N_s^{deph} = p(N_m - 1)/\beta_w$ is the total number of spin excitations generated by write pulses corresponding to modes different from the rephased one. Adding the contributions B.4-B.5 to B.2-B.3, we can write the expressions for the detected read-out efficiency ($p_{r|w} = p_{r,w}/p_w$) and the cross correlation function ($g_{w,r}^{(2)} = p_{w,r}/(p_w p_r)$)as

$$p_{r|w} = p^{int}_{r|w}\eta_r + p(N_{\mathrm{m}} - p^{\mathrm{int}}_{r|w})\frac{\beta_r}{\beta_w}\xi_{eg}\eta_r \tag{B.6}$$

$$g^{(2)}_{w,r} = 1 + \frac{p^{int}_{r|w}(1-p)}{pp^{int}_{r|w} + p(N_{\mathrm{m}} - p^{\mathrm{int}}_{r|w})\frac{\beta_r}{\beta_w}\xi_{eg}}. \tag{B.7}$$

We can observe that increasing N_{m} increases the incoherent therm in $p_{r|w}$ and decreases $g^{(2)}_{w,r}$. However this can be overcome by increasing the ratio β_w/β_r. In our experiment we obtain this by having an optical cavity resonant with the write photon but decoupled from the read photon mode. In such a situation the ratio β_w/β_r is equal to the write photon cavity enhancement factor $\frac{2F}{\pi}$ (compare also simulations in the following section).

Please note that experiments with cavities for both write and read process have been realized as well [219], with the aim of improving the read-out efficiency. However, in this case the ratio β_w/β_r is unity, making temporally multimode operation impossible. For achieving higher retrieval efficiencies in the current setup, the optical depth needs to be improved by other means, for example by compressing the atoms during the MOT phase.

B.3 Multi-mode Cross-correlation Simulations: Dependence on cavity enhancement and retrieval efficiency

For the following simulations, the model from the previous section is used. No dependence of retrieval efficiency on storage time was considered, i.e. assuming $N_m\tau_m \ll \tau_{mem}$. Here, τ_m is the single-mode duration and τ_{mem} the memory lifetime.

For the given memory setup and parameters, Fig. B.3a) shows the scaling of cross-correlation as a function of mode number, plotted for different cavity enhancements. In red we show the current setup performance. As apparent from the simulation, for the multi-mode case substantial improvement is

still possible by increasing the cavity's finesse, However, for the single-mode case only small improvement is expected.

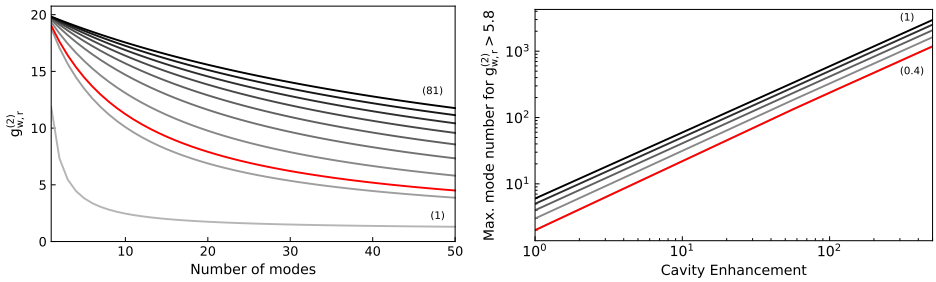

Figure B.3: a) $g^{(2)}_{w,r}$ as a function of number of input modes, for different values of the cavity enhancement between 1 (no cavity) and 81, in steps of 10. In red the current setup with a cavity enhancement of 14. b) Maximum number of input modes to comply with $g^{(2)}_{w,r} > 5.8$ vs. cavity enhancement, for different values of the retrieval efficiency between 0.4 (current setup) and unity, in steps of 0.15. In red the current setup with a retrieval efficiency of 0.4.

We observe that adding modes to the memory reduces quantum correlations due to increased noise. Given a minimum threshold for the cross-correlation function, it is instructive to investigate up to how many modes the memory supports, still complying with this threshold. As a threshold we choose a value of 5.8 (minimum value necessary for violating Bell's inequality [220]). For a given enhancement, Fig. B.3b) shows this maximum number as a function of cavity enhancement, plotted for different retrieval efficiencies. We find a linear behaviour on the cavity enhancement. Furthermore, we see that great improvement is still possible by increasing the retrieval efficiency of the memory towards unity.

B.4 Cavity enhancement for a single temporal mode

Up to now, the cavity was employed solely during multi-mode operation. Now, we investigate the performance of the memory in single-mode operation, i.e. for the DLCZ storage protocol in the homogeneously broadened medium. In Fig. B.4 we show measured cross-correlation as a function of storage time. For the same excitation probability p, we compare the performance with and without cavity enhancement of the write photon generation process. In both cases, measured data is in good agreement with the expected behaviour (solid lines, computed from Eq. B.7 with p, memory lifetime τ and cavity enhancement as stated in the figure caption).

Two important findings can be deduced from this measurement. Firstly, already at time zero the performance of the cavity enhanced memory is superior to the one without enhancement. This is a consequence of the non-unity retrieval efficiency of our memory. The retrieval efficiency at zero storage time is limited by insufficient optical depth and re-absorption (motional or spurious magnetic dephasing mechanisms do not yet play a role). The gain $(\mathrm{g}_{\mathrm{w,r}}^{(2),\,\mathrm{c}} - 1)/(\mathrm{g}_{\mathrm{w,r}}^{(2)} - 1)$, where $g_{w,r}^{(2),\,c}$ ($g_{w,r}^{(2)}$) is the cross-correlation function with (without) cavity, at zero storage time is 2.3. Secondly, the correlation decay versus storage time is much more apparent when the cavity is not employed. With cavity, $(\mathrm{g}_{\mathrm{w,r}}^{(2),\,\mathrm{c}} - 1)$ only drops by 15% between time zero and the $1/e$ memory lifetime $\tau \approx 72\mu s$. However, the same figure drops by 60% without cavity. This shows the noise reduction capability of the cavity and can be further enhanced by enhancing the finesse.

These results demonstrate that cavity enhanced write emission is not only beneficial in multi-mode operation (as investigated in the main body of the thesis) but can also greatly improve the performance of the single-mode protocol.

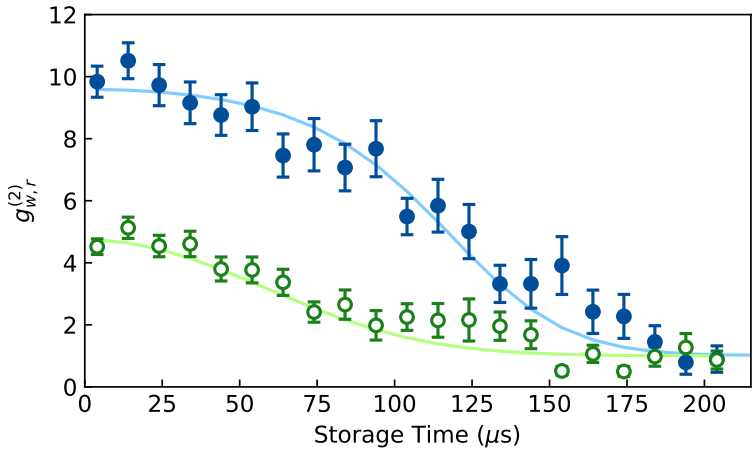

Figure B.4: Cross-correlation function $g^{(2)}_{w,r}$ as a function of storage time for DLCZ storage protocol in homogeneously broadened medium. Blue (green) data is taken with (without) cavity enhancement. $p \approx 10\%$ for both traces. Solid lines simulate expected behaviour, assuming a cavity enhancement of 14 for cavity enhanced emission and a $1/e$ memory lifetime of $\tau \approx 72\mu s$ in both cases.

Appendix C

Additional information on chapter 5

C.1 Memory performance with optical depth (with weak coherent states)

It is instructive to analyse the memory performance when varying optical depth (OD), since OD governs how efficiently the incoming light pulse is absorbed and re-emitted. For that, we vary the trapping laser power during the magneto-optical trap stage and used the shortest interrogation time possible to be able to scan the full range of OD available.

The OD value is obtained by measuring the transmission of a continuous coherent beam around resonance with the $|g_s\rangle \rightarrow |e_s\rangle$ transition. Results are shown in Fig. C.1. The storage efficiencies are measured for WCS pulses as input, shaped to mimic the temporal profile of the single photons generated in the Rydberg-based source.

We observe a saturation of the storage and retrieval efficiency $\eta_{wr} = \eta_w \cdot \eta_r$ for OD around 6.5. However, the write-in efficiency η_w seems to still profit from higher OD, while read-out efficiency η_r is already at the maximum. One possible explanation for this behaviour is re-emission followed by re-absorption, which limits the maximal retrieval efficiency in forward retrieval

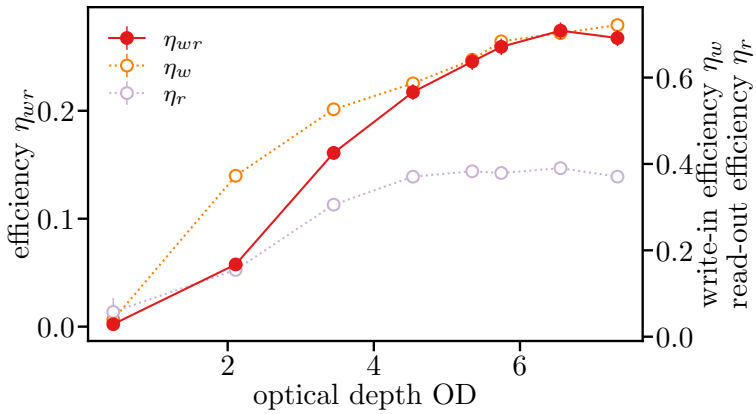

Figure C.1: Storage efficiencies η_w, η_r and η_{wr} as a function of the optical depth of the ensemble for weak coherent input pulses with a mean photon number of 0.077. For each data point, the write-in control pulse power and the delay are optimized.

(i.e. when the photon field is retrieved from the medium co-propagating to the input) [136, 206].

Data in the main text was taken for OD around 5, which constitutes a compromise between achieving high η_{wr} while at the same time maintaining an acceptable duty cycle for data acquisition.

C.2 Effect of the noise in the measured autocorrelation function of single photons

Noise originating either from the control beam or its interaction with the ensemble can lead to uncorrelated coincidences that affect the measured single-photon statistics of the transmitted or stored photon. In the absence of control field and atoms, the unperturbed autocorrelation is measured as:

$$g_{\text{in}}^{(2)}(0) = \frac{c_{1,2}}{p_1 p_2}, \tag{C.1}$$

where p_1 (p_2) is the probability of detection per trial on detector 1(2), and $c_{1,2}$ is the probability of coincidence detection per trial between both detectors. When a storage attempt is performed, the noise introduced by the control pulses and the atoms alter the probabilities for detection and coincidences as follows:

$$\tilde{c}_{1,2} = c_{1,2} + p_1 p_{n,2} + p_2 p_{n,1} + p_{n,1} p_{n,2} \tag{C.2}$$

$$\tilde{p}_{1(2)} = p_{1(2)} + p_{n,1(2)}. \tag{C.3}$$

Here, $p_{n,1}$ ($p_{n,2}$) is the noise probability for detector 1(2). The autocorrelation is therefore:

$$\begin{aligned} g^{(2)}_{\text{out}}(0) &= \frac{\tilde{c}_{1,2}}{\tilde{p}_1 \tilde{p}_2} \\ &= \frac{p_{12} + p_1 p_{n,2} + p_2 p_{n,1} + p_{n,1} p_{n,2}}{p_1 p_2 + p_{n,1} p_2 + p_{n,2} p_1 + p_{n,1} p_{n,2}}, \end{aligned} \tag{C.4}$$

which can be rewritten in terms of SNRs as

$$g^{(2)}_{\text{out}}(0) = \frac{g^{(2)}_{\text{in}}(0) + 1/s_1 + 1/s_2 + 1/(s_1 s_2)}{1 + 1/s_1 + 1/s_2 + 1/(s_1 s_2)}, \tag{C.5}$$

where $s_{1(2)} = p_{1(2)}/p_{n,1(2)}$ is the SNR for detector 1(2).

Assuming that SNRs are the same for both detectors, this expression finally simplifies to

$$g^{(2)}_{\text{out}}(0) = \frac{g^{(2)}_{\text{in}}(0) + 2/s + 1/s^2}{1 + 2/s + 1/s^2}. \tag{C.6}$$

In Fig. C.2, we characterize the effect of noise on the $g^{(2)}(0)$ of the stored and the transmitted photons for different values of $g^{(2)}(0)$ of the input photon (i.e. with no storage attempt). The input $g^{(2)}(0)$ was scanned by varying the mean number of photons in the probe (see Fig. 2 in the main text). We can see that, in general, the output $g^{(2)}(0)$ degrades compared to the input $g^{(2)}(0)$ and that the autocorrelation of the transmitted photon is better than the one of the stored photon. Therefore, we can conclude that the model qualitatively reproduces the expected trend. We attribute the imperfection in the quantitative analysis to low statistics and experimental fluctuations.

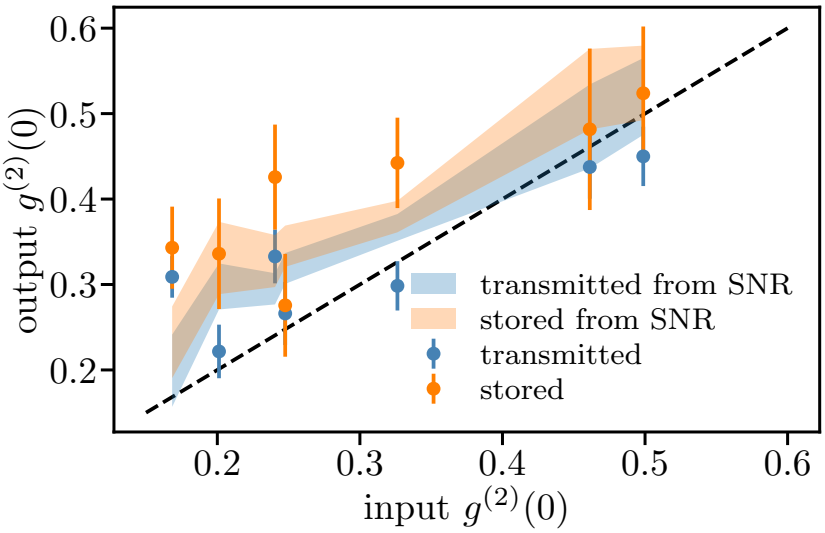

Figure C.2: Output $g^{(2)}(0)$ of the transmitted and the stored photons as a function of the input $g^{(2)}(0)$. Dashed black line: autocorrelation after the memory equals input. Shaded areas: autocorrelation for transmitted and stored photon as expected from eq. C.6, taking into account uncertainty in $g^{(2)}_{\text{in}}(0)$ and SNR.

Appendix D

Additional information on chapter 6

D.1 Phase matching for DLCZ and EIT memories

EIT and Raman memories store an input photon by means of write and read coupling beams. The phase matching and energy conservation conditions for this process reads

$$\boldsymbol{k}_{p,i} - \boldsymbol{k}_{c,w} + \boldsymbol{k}_{c,r} - \boldsymbol{k}_{p,o} = 0 \tag{D.1}$$

$$\omega_{p,i} - \omega_{c,w} + \omega_{c,r} - \omega_{p,o} = 0, \tag{D.2}$$

involving the input and output photons ($\boldsymbol{k}_{p,i}$ and $\boldsymbol{k}_{p,o}$) and the write and the read control pulse ($\boldsymbol{k}_{c,w}$ and $\boldsymbol{k}_{c,r}$). Pulses and photons differ by the ground state splitting of 6.8 GHz.

For experimental simplicity, we demand the two coupling pulses to be colinear and copropagating, which leads to the photon being reemitted in forward direction. eq. (D.1) can then be rewritten as

$$\boldsymbol{e}_p k_{p,i} - \boldsymbol{e}_c k_{c,w} + \boldsymbol{e}_c k_{c,r} - \boldsymbol{e}_p k_{p,o} = \boldsymbol{e}_p(k_{p,i} - k_{p,o}) - \boldsymbol{e}_c(k_{c,w} - k_{c,r}) = 0, \tag{D.3}$$

where $\boldsymbol{e}_p$ and $\boldsymbol{e}_c$ are the unit vectors for the photon and coupling modes. We can now distinguish two cases. If $\boldsymbol{e}_p = \boldsymbol{e}_c$, it follows that $k_{p,i} - k_{c,w} +$

$k_{c,r} - k_{p,o} = 0$. This is naturally fullfilled, as this is precisely the energy conservation condition ($k = \omega/c$). This is also the situation which minimizes the spin wave vector, as $\Delta\boldsymbol{k} = \boldsymbol{e}_p k_{p,i} - \boldsymbol{e}_c k_{c,w} = k_{p,i} - k_{c,w} \approx 0$. A small spin wave vector during storage is preferable to minimize motional dephasing. If $\boldsymbol{e}_p \neq \boldsymbol{e}_c$, $k_{p,i} - k_{p,o} = 0$ and $k_{c,w} - k_{c,r} = 0$ need to be fullfilled simultaneously. This can be accomplished by choosing the same intermediate level, which is usually the case.

For the DLCZ memory, the phase and energy conservation conditions read slightly differently:

$$\boldsymbol{k}_W - \boldsymbol{k}_{p,w} + \boldsymbol{k}_R - \boldsymbol{k}_{p,r} = 0 \tag{D.4}$$

$$\omega_W - \omega_{p,w} + \omega_R - \omega_{p,r} = 0 \tag{D.5}$$

involving the write and read photon ($\boldsymbol{k}_{p,w}$ and $\boldsymbol{k}_{p,r}$) and the write and the read pulse ($\boldsymbol{k}_W$ and $\boldsymbol{k}_R$). Here, we demand that the two pulses are colinear but counterpropagating, leading to a pair of photons which is emitted colinear and counterpropagating as well:

$$\boldsymbol{e}_c k_W - \boldsymbol{e}_p k_{p,w} + (-\boldsymbol{e}_c k_R) - (-\boldsymbol{e}_p k_{p,r}) = \boldsymbol{e}_c(k_W - k_R) - \boldsymbol{e}_p(k_{p,w} - k_{p,r}) = 0. \tag{D.6}$$

where $\boldsymbol{e}_p$ and $\boldsymbol{e}_c$ are the unit vectors for the photon and coupling pulse modes. We again distinguish two cases. $\boldsymbol{e}_p = \boldsymbol{e}_c$ minimizes the spin wave vector, as $\Delta\boldsymbol{k} = \boldsymbol{e}_c k_W - \boldsymbol{e}_p k_{p,w} = k_W - k_{p,w} \approx 0$. It follows that $k_W - k_R - k_{p,1} + k_{p,2} = 0$. This contradicts with the energy conservation and can only be fullfilled for $k_W - k_R = k_{p,1} - k_{p,2} = 0$, i.e. degenerate ground states. The same holds true for $\boldsymbol{e}_p \neq \boldsymbol{e}_c$.

D.2 Level and excitation scheme for cavity-enhanced DLCZ readout

The general setup is the same as in subsection 3.4.2. For this study, $|5^2S_{1/2}, F = 2\rangle$ is chosen as the DLCZ ground state and $|5^2S_{1/2}, F = 1\rangle$ as the storage state, see Fig. D.1. No Zeeman optical pumping is applied, and a small bias field perpendicular to the photon mode is applied. The

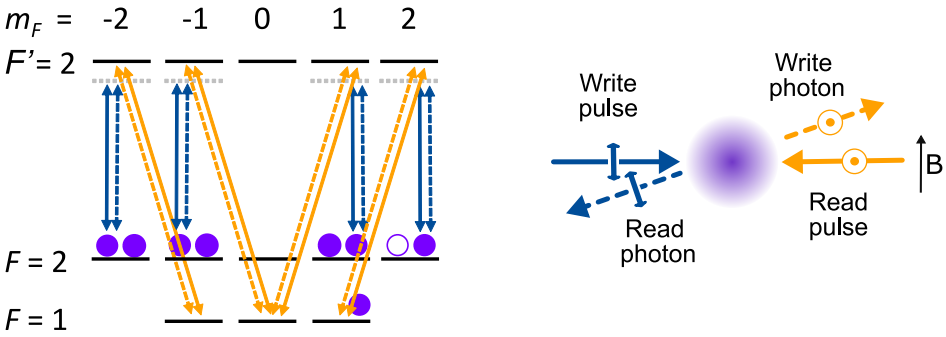

Figure D.1: (a) Level scheme. After excitation with horizontal light, only vertically polarised write photons are detected, which result from a superposition of σ^+ and σ^--polarized decay channels. The read-out reverses this process. (b) Excitation scheme and B-field direction.

quarter-wave plates in the cavity were removed and the atoms were probed with linear light. After excitation with horizontally polarized write pulse light, only vertically polarised write photons are selected by polarisation filtering. Those photons result from a superposition of σ^+ and σ^--polarized decay channels. They are not resonant to the cavity and are reflected on the cavity PBS. After read-out with a vertically polarised read pulse, the read photon is emitted horizontally polarised. This read photon emission is enhanced by the cavity.

D.3 Vacuum Rabi Splitting

To fit the data presented in chapter 7, I used the formalism presented in [209]. The absorption spectrum is proportional to the imaginary part of the atom-cavity susceptibility χ, which essentially contains of two weighted and

displaced Lorentzian curves:

$$\begin{aligned}\mathrm{Im}\chi(\omega) = \cos^2\theta \frac{\Gamma_-/\pi}{\Gamma_-^2 + \{\omega - \omega_0 + \Delta/2 - 1/2(\Delta^2 + \Omega_R^2)^{1/2}\}^2} \\ + \sin^2\theta \frac{\Gamma_+/\pi}{\Gamma_+^2 + \{\omega - \omega_0 + \Delta/2 + 1/2(\Delta^2 + \Omega_R^2)^{1/2}\}^2} \qquad \text{(D.7)}\end{aligned}$$

$$\tan\theta = \frac{-\Delta + (\Delta^2 + \Omega_R^2)^{1/2}}{\Omega_R}, \qquad \Delta = \omega_0 - \omega_c.$$

Here, $\Gamma_\pm$ are the damping factors of the respective decay channels, and define the linewidth of the two peaks. When fitting the data in chapter 7, it was assumed that $\Gamma_- = \Gamma_+$ for simplicity. ω_c is the cavity resonance, ω the atomic resonance, and Ω_R the Rabi frequency / frequency splitting of the peaks.

Fitting the retrieval efficiency with eq. D.7 is justified if we assume that $p_{r|w} \propto \mathrm{OD} \propto \mathrm{Im}\chi$, which is true for low OD. I particular the position of maximum absorption should coincide with those of maximum retrieval efficiency, so the Rabi frequency extracted from those fits should be a good estimate. Free fitting parameters were $\Gamma_\pm$, Δ and Ω_R.

Appendix E

Additional information on chapter 7

E.1 Characterisation of the birefringent beam displacer

For this application, it is crucial that the beam displacer splits or re-combines the optical modes exactly parallel to each other, and with sufficient spacing to make them distinguishable. This is verified in Fig. E.1(a) by sending unpolarised light through the device. The mode spacing is measured as a function of distance after the displacer. For the beam size of our choice, the modes are well separated (inset of Fig. E.1(a)) and sufficiently parallel.

E.2 Locking on the TEM01 mode

In the former setup, a chopped lock was used to iterate between locking and photon detection, thereby avoiding strong lock light from reaching the detector. This is a safe but somewhat lossy setup, as both photons need to be coupled in and out of the fiber for that purpose. The fiber-to-fiber transmission reaches 65%, at best. Here, I was investigating a new

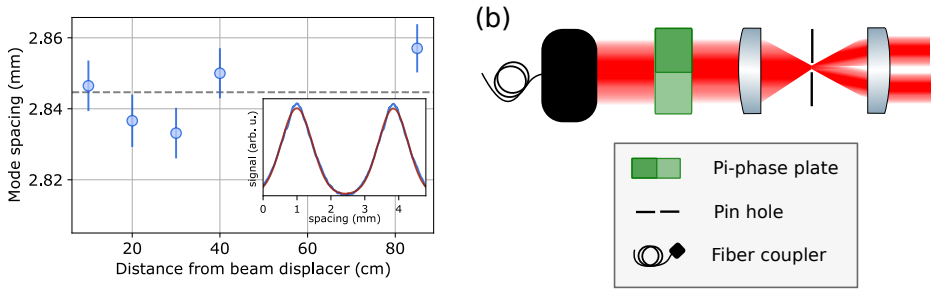

Figure E.1: (a) Mode spacing as a function of distance from the displacer. A mean spacing of 2.845 mm was measured (grey dotted line). Inset shows the spatial mode shape, including a double-Gaussian fit. Each mode has a $1/e^2$ beam radius of $\approx 900\,\mu$m. (b) Transformation of the locking mode from TEM00 to TEM01 via a pi-phase plate and spatial cleaning through a pin hole. The TEM01 mode is subsequently injected into the cavity.

approach based on locking with a higher-order Laguerre-Gaussian mode, namely TEM01 instead of the ground mode TEM00. Those modes are orthogonal to each other and as we are using single-mode fibers, TEM01 does not couple to the photon fiber, rendering the chopped lock obsolete. The cavity is, however, still sufficiently resonant to derive a locking signal from it. The TEM01 mode is generated from a TEM00 mode with a pi-phase plate (Vortex Photonics), followed by a 4f-microscope with a pin hole, as depicted in Fig. E.1(b). Experimentally, an almost 20000-fold (OD = 4.3) coupling suppression into SM fiber could be achieved. The maximum power that can be sent to the cavity for locking, before saturating the SPDs, is around 30 nW, which is sufficient for high-gain avalanche photo detectors.

E.3 Tuning the cavity length

The corner retroreflector is shown in Fig. E.2. In order to change the cavity length by 45 mm, this reflector needs to shift by half that amount, so around 23 mm. For course adjustment, the reflector itself slides on a rail which can

be locked in arbitrary positions by a locking screw. Fine adjustment of up to 12 mm is done with a small translation stage attached to the rail. A kinematic mirror mount is bolted onto the translation stage, holding the retroreflector consisting of two rectangular mirror. The mirror mount also allows for control of pitch and roll angle. The beam height is maintained to below 75 mm. A standard 25 mm translation stage with only z-translation degree of freedom is also shown, illustrating the compactness of the design.

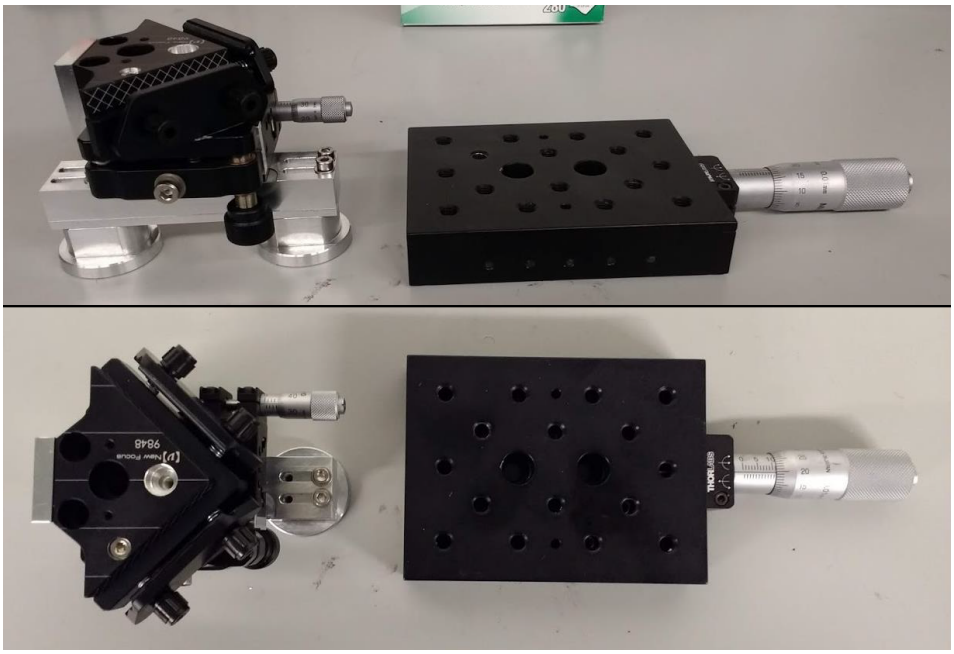

Figure E.2: Translation mount used in the new enhancement cavity design. The retroreflecting mirrors itself are not mounted. To the right, a standard 25 mm translation stage is also shown, illustrating the compactness of the design.

Bibliography

1. Hilbert, M. "Digital Technology and Social Change: The Digital Transformation of Society from a Historical Perspective". *Dialogues in Clinical Neuroscience* **22,** 189–194 (2020) (cit. on p. 1).
2. Hilbert, M. & López, P. "The World's Technological Capacity to Store, Communicate, and Compute Information". *Science* **332,** 60–65 (2011) (cit. on p. 1).
3. Vincent, J. *Former Go Champion Beaten by DeepMind Retires after Declaring AI Invincible*. The Verge. `https://www.theverge.com/2019/11/27/20985260/ai-go-alphago-lee-se-dol-retired-deepmind-defeat` (2022) (cit. on p. 2).
4. Arute, F. *et al.* "Quantum Supremacy Using a Programmable Superconducting Processor". *Nature* **574,** 505–510 (7779 2019) (cit. on p. 2).
5. Pan, F., Chen, K. & Zhang, P. "Solving the Sampling Problem of the Sycamore Quantum Circuits". *Physical Review Letters* **129,** 090502 (2022) (cit. on p. 2).
6. Kimble, H. J. "The Quantum Internet". *Nature* **453,** 1023–1030 (2008) (cit. on p. 2).
7. Simon, C. "Towards a Global Quantum Network". *Nature Photonics* **11,** 678–680 (2017) (cit. on p. 2).
8. Wehner, S., Elkouss, D. & Hanson, R. "Quantum Internet: A Vision for the Road Ahead". *Science* **362,** eaam9288 (2018) (cit. on p. 2).
9. Ekert, A. K. "Quantum Cryptography Based on Bell's Theorem". *Physical Review Letters* **67,** 661–663 (1991) (cit. on p. 2).

10. Bennett, C. H. *et al.* "Teleporting an Unknown Quantum State via Dual Classical and Einstein-Podolsky-Rosen Channels". *Physical Review Letters* **70,** 1895–1899 (1993) (cit. on pp. 2, 3).
11. Broadbent, A., Fitzsimons, J. & Kashefi, E. *Universal Blind Quantum Computation*. in *2009 50th Annual IEEE Symposium on Foundations of Computer Science* (2009), 517–526 (cit. on p. 2).
12. Gottesman, D., Jennewein, T. & Croke, S. "Longer-Baseline Telescopes Using Quantum Repeaters". *Physical Review Letters* **109,** 070503 (2012) (cit. on p. 3).
13. Kómár, P. *et al.* "A Quantum Network of Clocks". *Nature Physics* **10,** 582–587 (8 2014) (cit. on p. 3).
14. Bennett, C. H. & Brassard, G. "Quantum Cryptography: Public Key Distribution and Coin Tossing". *Theoretical Computer Science. Theoretical Aspects of Quantum Cryptography – Celebrating 30 Years of BB84* **560,** 7–11 (2014) (cit. on p. 3).
15. Northup, T. E. & Blatt, R. "Quantum Information Transfer Using Photons". *Nature Photonics* **8,** 356–363 (5 2014) (cit. on pp. 3, 11).
16. Duan, L. M., Lukin, M. D., Cirac, J. I. & Zoller, P. "Long-Distance Quantum Communication with Atomic Ensembles and Linear Optics". *Nature* **414,** 413–418 (2001) (cit. on pp. 3, 6, 7, 11, 19, 25, 87, 95, 114).
17. Sangouard, N., Simon, C., de Riedmatten, H. & Gisin, N. "Quantum Repeaters Based on Atomic Ensembles and Linear Optics". *Reviews of Modern Physics* **83,** 33–80 (2011) (cit. on pp. 3, 5–7, 11).
18. Afzelius, M., Simon, C., de Riedmatten, H. & Gisin, N. "Multimode Quantum Memory Based on Atomic Frequency Combs". *Physical Review A: Atomic, Molecular, and Optical Physics* **79,** 052329 (2009) (cit. on pp. 3, 11, 29, 57).
19. Tittel, W. *et al.* "Photon-Echo Quantum Memory in Solid State Systems". *Laser & Photonics Reviews* **4,** 244–267 (2010) (cit. on pp. 3, 11, 29, 34).
20. Neuwirth, J. *et al.* "Quantum Dot Technology for Quantum Repeaters: From Entangled Photon Generation toward the Integration with Quantum Memories". *Materials for Quantum Technology* **1,** 043001 (2021) (cit. on pp. 3, 16).
21. Ruf, M., Wan, N. H., Choi, H., Englund, D. & Hanson, R. "Quantum Networks Based on Color Centers in Diamond". *Journal of Applied Physics* **130,** 070901 (2021) (cit. on pp. 3, 11, 17).

22. Kumar, P. "Quantum Frequency Conversion". *Optics Letters* **15,** 1476–1478 (1990) (cit. on p. 3).

23. Chou, C.-W. *et al.* "Functional Quantum Nodes for Entanglement Distribution over Scalable Quantum Networks." *Science (New York, N.Y.)* **316,** 1316–20 (2007) (cit. on pp. 3, 7, 17, 70).

24. Li, H. *et al.* "Heralding Quantum Entanglement between Two Room-Temperature Atomic Ensembles". *Optica* **8,** 925–929 (2021) (cit. on pp. 3, 16, 18, 70).

25. Pompili, M. *et al.* "Realization of a Multinode Quantum Network of Remote Solid-State Qubits". *Science* **372,** 259–264 (2021) (cit. on pp. 3, 18).

26. Ritter, S. *et al.* "An Elementary Quantum Network of Single Atoms in Optical Cavities". *Nature* **484,** 195–200 (2012) (cit. on pp. 3, 17, 18).

27. Lago-Rivera, D., Grandi, S., Rakonjac, J. V., Seri, A. & de Riedmatten, H. "Telecom-Heralded Entanglement between Multimode Solid-State Quantum Memories". *Nature* **594,** 37–40 (2021) (cit. on pp. 3, 18, 70, 95, 112, 117).

28. Krutyanskiy, V. *et al. Entanglement of Trapped-Ion Qubits Separated by 230 Meters*. `http://arxiv.org/abs/2208.14907` (2022). preprint (cit. on pp. 3, 18, 19).

29. Maring, N. *et al.* "Photonic Quantum State Transfer between a Cold Atomic Gas and a Crystal". *Nature* **551,** 485–488 (2017) (cit. on pp. 3, 15, 81, 107, 110).

30. Craddock, A. N. *et al.* "Quantum Interference between Photons from an Atomic Ensemble and a Remote Atomic Ion". *Physical Review Letters* **123,** 213601 (2019) (cit. on pp. 3, 17).

31. Wootters, W. K. & Zurek, W. H. "A Single Quantum Cannot Be Cloned". *Nature* **299,** 802–803 (1982) (cit. on p. 4).

32. Briegel, H.-J., Dür, W., Cirac, J. I. & Zoller, P. "Quantum Repeaters: The Role of Imperfect Local Operations in Quantum Communication". *Physical Review Letters* **81,** 5932–5935 (1998) (cit. on pp. 4, 6).

33. Sangouard, N. *et al.* "Long-Distance Entanglement Distribution with Single-Photon Sources". *Physical Review A* **76,** 050301 (2007) (cit. on pp. 8, 9, 70, 84).

34. Simon, C. *et al.* "Quantum Repeaters with Photon Pair Sources and Multimode Memories". *Physical Review Letters* **98,** 190503 (2007) (cit. on pp. 10, 14, 67).

35. Cirac, J. I., Zoller, P., Kimble, H. J. & Mabuchi, H. "Quantum State Transfer and Entanglement Distribution among Distant Nodes in a Quantum Network". *Physical Review Letters* **78,** 3221–3224 (1997) (cit. on p. 11).

36. Boozer, A. D., Boca, A., Miller, R., Northup, T. E. & Kimble, H. J. "Reversible State Transfer between Light and a Single Trapped Atom". *Physical Review Letters* **98,** 193601 (2007) (cit. on p. 11).

37. Stute, A. *et al.* "Tunable Ion-Photon Entanglement in an Optical Cavity". *Nature* **485,** 482–485 (2012) (cit. on p. 11).

38. Moehring, D. L. *et al.* "Entanglement of Single-Atom Quantum Bits at a Distance". *Nature* **449,** 68–71 (7158 2007) (cit. on p. 11).

39. Lukin, M. D. "Colloquium: Trapping and Manipulating Photon States in Atomic Ensembles". *Reviews of Modern Physics* **75,** 457–472 (2003) (cit. on p. 11).

40. Kuzmich, A. *et al.* "Generation of Nonclassical Photon Pairs for Scalable Quantum Communication with Atomic Ensembles". *Nature* **423,** 731–734 (2003) (cit. on pp. 11, 25).

41. Van der Wal, C. H. *et al.* "Atomic Memory for Correlated Photon States". *Science* **301,** 196–201 (July 2003) (cit. on pp. 11, 25).

42. Julsgaard, B., Sherson, J., Cirac, J. I., Fiurášek, J. & Polzik, E. S. "Experimental Demonstration of Quantum Memory for Light". *Nature* **432,** 482–486 (7016 2004) (cit. on p. 11).

43. Chanelière, T. *et al.* "Storage and Retrieval of Single Photons Transmitted between Remote Quantum Memories". *Nature* **438,** 833–836 (7069 2005) (cit. on p. 11).

44. Turukhin, A. V. *et al.* "Observation of Ultraslow and Stored Light Pulses in a Solid". *Physical Review Letters* **88,** 023602 (2001) (cit. on p. 11).

45. De Riedmatten, H., Afzelius, M., Staudt, M. U., Simon, C. & Gisin, N. "A Solid-State Light-Matter Interface at the Single-Photon Level". *Nature* **456,** 773–777 (2008) (cit. on pp. 11, 57).

46. Maurer, P. C. *et al.* "Room-Temperature Quantum Bit Memory Exceeding One Second". *Science* **336,** 1283–1286 (2012) (cit. on p. 11).

47. Heshami, K. *et al.* "Quantum Memories: Emerging Applications and Recent Advances". *Journal of Modern Optics* **63,** 2005–2028 (2016) (cit. on p. 11).

48. Bussières, F. *et al.* "Prospective Applications of Optical Quantum Memories". *Journal of Modern Optics* **60,** 1519–1537 (2013) (cit. on p. 11).

49. Stephenson, L. J. *et al.* "High-Rate, High-Fidelity Entanglement of Qubits across an Elementary Quantum Network". *Physical Review Letters* **124,** 110501 (2020) (cit. on pp. 12, 18).

50. Brekenfeld, M., Niemietz, D., Christesen, J. D. & Rempe, G. "A Quantum Network Node with Crossed Optical Fibre Cavities". *Nature Physics* **16,** 647–651 (6 2020) (cit. on p. 12).

51. Körber, M. *et al.* "Decoherence-Protected Memory for a Single-Photon Qubit". *Nature Photonics* **12,** 18–21 (2018) (cit. on pp. 12, 13).

52. Hedges, M. P., Longdell, J. J., Li, Y. & Sellars, M. J. "Efficient Quantum Memory for Light". *Nature* **465,** 1052–1056 (7301 2010) (cit. on p. 12).

53. Hosseini, M., Sparkes, B., Campbell, G., Lam, P. & Buchler, B. "High Efficiency Coherent Optical Memory with Warm Rubidium Vapour". *Nature Communications* **2,** 174 (1 2011) (cit. on pp. 12, 19, 57, 116).

54. Cho, Y.-W. *et al.* "Highly Efficient Optical Quantum Memory with Long Coherence Time in Cold Atoms". *Optica* **3,** 100–107 (2016) (cit. on pp. 12, 19, 37, 116).

55. Wang, Y. *et al.* "Efficient Quantum Memory for Single-Photon Polarization Qubits". *Nature Photonics* **13,** 346–351 (May 2019) (cit. on pp. 12, 19, 37, 70, 88, 116).

56. Cao, M. *et al.* "Efficient Reversible Entanglement Transfer between Light and Quantum Memories". *Optica* **7,** 1440–1444 (2020) (cit. on pp. 12, 19, 70, 79, 80, 86, 88, 116).

57. Hsiao, Y.-F. *et al.* "Highly Efficient Coherent Optical Memory Based on Electromagnetically Induced Transparency". *Pysical Review Letters* **120,** 183602 (2018) (cit. on pp. 12, 37, 116).

58. Humphreys, P. C. *et al.* "Deterministic Delivery of Remote Entanglement on a Quantum Network". *Nature* **558,** 268–273 (7709 2018) (cit. on pp. 12, 17, 18).

59. Bartling, H. P. *et al.* "Entanglement of Spin-Pair Qubits with Intrinsic Dephasing Times Exceeding a Minute". *Physical Review X* **12,** 011048 (2022) (cit. on p. 13).

60. Wang, P. *et al.* "Single Ion Qubit with Estimated Coherence Time Exceeding One Hour". *Nature Communications* **12,** 233 (1 2021) (cit. on p. 13).

61. Zhou, Z.-Q. *et al.* "A Transportable Long-Lived Coherent Memory for Light Pulses". *Science Bulletin* **67,** 2402–2405 (2022) (cit. on p. 13).

62. Wang, Y., Craddock, A. N., Sekelsky, R., Flament, M. & Namazi, M. "Field-Deployable Quantum Memory for Quantum Networking". *Physical Review Applied* **18,** 044058 (2022) (cit. on pp. 13, 37).

63. Dideriksen, K. B., Schmieg, R., Zugenmaier, M. & Polzik, E. S. "Room-Temperature Single-Photon Source with near-Millisecond Built-in Memory". *Nature Communications* **12,** 3699 (1 2021) (cit. on pp. 13, 37).

64. Dudin, Y. O., Li, L. & Kuzmich, A. "Light Storage on the Time Scale of a Minute". *Physical Review A - Atomic, Molecular, and Optical Physics* **87,** 1–4 (2013) (cit. on pp. 13, 19, 33, 34, 36, 37, 96, 102, 116).

65. Wang, X.-J. *et al.* "Cavity-Enhanced Atom-Photon Entanglement with Subsecond Lifetime". *Physical Review Letters* **126,** 090501 (2021) (cit. on pp. 13, 19, 36–38, 66, 86–88, 95, 96, 106, 116).

66. Simon, C. *et al.* "Quantum Memories". *The European Physical Journal D* **58,** 1–22 (2010) (cit. on p. 14).

67. Vernaz-Gris, P., Huang, K., Cao, M., Sheremet, A. S. & Laurat, J. "Highly-Efficient Quantum Memory for Polarization Qubits in a Spatially-Multiplexed Cold Atomic Ensemble". *Nature Communications* **9,** 1–6 (2018) (cit. on pp. 14, 26, 88).

68. Yang, T.-S. *et al.* "Multiplexed Storage and Real-Time Manipulation Based on a Multiple Degree-of-Freedom Quantum Memory". *Nature Communications* **9,** 3407 (1 2018) (cit. on p. 14).

69. Businger, M. *et al.* "Non-Classical Correlations over 1250 Modes between Telecom Photons and 979-Nm Photons Stored in 171Yb3+:Y2SiO5". *Nature Communications* **13,** 6438 (1 2022) (cit. on p. 14).

70. Pu, Y. F. *et al.* "Experimental Realization of a Multiplexed Quantum Memory with 225 Individually Accessible Memory Cells". *Nature Communications* **8,** 15359 (May 2017) (cit. on pp. 14, 19, 57, 86, 96, 116).

71. Lipka, M., Mazelanik, M., Leszczyński, A., Wasilewski, W. & Parniak, M. "Massively-Multiplexed Generation of Bell-type Entanglement Using a Quantum Memory". *Communications Physics* **4,** 1–10 (1 2021) (cit. on pp. 14, 19, 57, 96, 116).

72. Bradley, C. E. *et al.* "A Ten-Qubit Solid-State Spin Register with Quantum Memory up to One Minute". *Physical Review X* **9,** 031045 (2019) (cit. on p. 14).

73. Puigibert, M. l. G. *et al.* "Entanglement and Nonlocality between Disparate Solid-State Quantum Memories Mediated by Photons". *Physical Review Research* **2,** 013039 (2020) (cit. on pp. 15, 16).

74. Lauritzen, B. *et al.* "Telecommunication-Wavelength Solid-State Memory at the Single Photon Level". *Physical Review Letters* **104,** 080502 (2010) (cit. on p. 15).

75. Kolchin, P., Belthangady, C., Du, S., Yin, G. Y. & Harris, S. E. "Electro-Optic Modulation of Single Photons". *Physical Review Letters* **101,** 103601 (2008) (cit. on p. 15).

76. Morin, O., Körber, M., Langenfeld, S. & Rempe, G. "Deterministic Shaping and Reshaping of Single-Photon Temporal Wave Functions". *Physical Review Letters* **123,** 133602 (2019) (cit. on p. 15).

77. Nisbet-Jones, P. B. R., Dilley, J., Ljunggren, D. & Kuhn, A. "Highly Efficient Source for Indistinguishable Single Photons of Controlled Shape". *New Journal of Physics* **13,** 103036 (2011) (cit. on p. 15).

78. Farrera, P. *et al.* "Generation of Single Photons with Highly Tunable Wave Shape from a Cold Atomic Ensemble". *Nature Communications* **7,** 13556 (2016) (cit. on p. 15).

79. Dudin, Y. O. *et al.* "Entanglement of Light-Shift Compensated Atomic Spin Waves with Telecom Light". *Physical Review Letters* **105,** 260502 (2010) (cit. on pp. 15, 16, 19, 87, 95).

80. Farrera, P., Maring, N., Albrecht, B., Heinze, G. & de Riedmatten, H. "Nonclassical Correlations between a C-band Telecom Photon and a Stored Spin-Wave". *Optica* **3,** 1019–1024 (2016) (cit. on pp. 15, 83, 84, 107, 111, 112, 128).

81. Krutyanskiy, V. *et al. A Telecom-Wavelength Quantum Repeater Node Based on a Trapped-Ion Processor*. `http://arxiv.org/abs/2210.05418` (2022). preprint (cit. on pp. 15, 19).

82. Van Leent, T. *et al.* "Long-Distance Distribution of Atom-Photon Entanglement at Telecom Wavelength". *Physical Review Letters* **124,** 010510 (2020) (cit. on pp. 15, 37, 107).

83. Davidson, O., Finkelstein, R., Poem, E. & Firstenberg, O. "Bright Multiplexed Source of Indistinguishable Single Photons with Tunable GHz-bandwidth at Room Temperature". *New Journal of Physics* **23,** 073050 (2021) (cit. on p. 16).

84. Balić, V., Braje, D. A., Kolchin, P., Yin, G. Y. & Harris, S. E. "Generation of Paired Photons with Controllable Waveforms". *Physical Review Letters* **94,** 183601 (2005) (cit. on p. 16).

85. Shu, C. *et al.* "Subnatural-Linewidth Biphotons from a Doppler-broadened Hot Atomic Vapour Cell". *Nature Communications* **7,** 12783 (1 2016) (cit. on p. 16).

86. Chen, J.-M. "Room-Temperature Biphoton Source with a Spectral Brightness near the Ultimate Limit". *Physical Review Research* **4** (2022) (cit. on p. 16).

87. Srivathsan, B. *et al.* "Narrow Band Source of Transform-Limited Photon Pairs via Four-Wave Mixing in a Cold Atomic Ensemble". *Physical Review Letters* **111,** 123602 (2013) (cit. on p. 16).

88. Thompson, J. K., Simon, J., Loh, H. & Vuletić, V. "A High-Brightness Source of Narrowband, Identical-Photon Pairs". *Science* **313,** 74–77 (2006) (cit. on pp. 16, 88).

89. Matsukevich, D. N. *et al.* "Entanglement of Remote Atomic Qubits". *Physical Review Letters* **96,** 030405–4 (2006) (cit. on p. 16).

90. Chang, W. *et al.* "Long-Distance Entanglement between a Multiplexed Quantum Memory and a Telecom Photon". *Physical Review X* **9,** 041033 (2019) (cit. on p. 16).

91. Burnham, D. C. & Weinberg, D. L. "Observation of Simultaneity in Parametric Production of Optical Photon Pairs". *Physical Review Letters* **25,** 84–87 (1970) (cit. on p. 16).

92. Slattery, O., Ma, L., Zong, K. & Tang, X. "Background and Review of Cavity-Enhanced Spontaneous Parametric Down-Conversion". *Journal of Research of the National Institute of Standards and Technology* **124,** 124019 (2019) (cit. on p. 16).

93. Niizeki, K. *et al.* "Ultrabright Narrow-Band Telecom Two-Photon Source for Long-Distance Quantum Communication". *Applied Physics Express* **11,** 042801 (2018) (cit. on p. 16).

94. Fekete, J., Rieländer, D., Cristiani, M. & de Riedmatten, H. "Ultranarrow-Band Photon-Pair Source Compatible with Solid State Quantum Memories and Telecommunication Networks". *Physical Review Letters* **110,** 220502 (2013) (cit. on p. 16).
95. Rakonjac, J. V. *et al.* "Entanglement between a Telecom Photon and an On-Demand Multimode Solid-State Quantum Memory". *Physical Review Letters* **127,** 210502 (2021) (cit. on pp. 16, 70).
96. Buser, G., Mottola, R., Cotting, B., Wolters, J. & Treutlein, P. "Single-Photon Storage in a Ground-State Vapor Cell Quantum Memory". *PRX Quantum* **3,** 020349 (2022) (cit. on p. 16).
97. Ornelas-Huerta, D. P. *et al.* "On-Demand Indistinguishable Single Photons from an Efficient and Pure Source Based on a Rydberg Ensemble". *Optica* **7,** 813–819 (2020) (cit. on pp. 16, 17, 19, 71, 86).
98. Somaschi, N. *et al.* "Near-Optimal Single-Photon Sources in the Solid State". *Nature Photonics* **10,** 340–345 (5 2016) (cit. on p. 16).
99. Wang, H. *et al.* "High-Efficiency Multiphoton Boson Sampling". *Nature Photonics* **11,** 361–365 (6 2017) (cit. on p. 16).
100. Akopian, N., Wang, L., Rastelli, A., Schmidt, O. G. & Zwiller, V. "Hybrid Semiconductor-Atomic Interface: Slowing down Single Photons from a Quantum Dot". *Nature Photonics* **5,** 230–233 (2011) (cit. on pp. 16, 71).
101. Wolters, J. *et al.* "Simple Atomic Quantum Memory Suitable for Semiconductor Quantum Dot Single Photons". *Physical Review Letters* **119,** 060502 (2017) (cit. on pp. 16, 80).
102. Tang, J.-S. *et al.* "Storage of Multiple Single-Photon Pulses Emitted from a Quantum Dot in a Solid-State Quantum Memory". *Nature communications* **6** (2015) (cit. on pp. 16, 71).
103. Thomas, S. E. *et al. Deterministic Storage and Retrieval of Telecom Quantum Dot Photons Interfaced with an Atomic Quantum Memory*. `http://arxiv.org/abs/2303.04166` (2023). preprint (cit. on pp. 16, 71).
104. Mizuochi, N. *et al.* "Electrically Driven Single-Photon Source at Room Temperature in Diamond". *Nature Photonics* **6,** 299–303 (5 2012) (cit. on p. 16).
105. Wilk, T., Webster, S. C., Specht, H. P., Rempe, G. & Kuhn, A. "Polarization-Controlled Single Photons". *Physical Review Letters* **98,** 1–4 (2007) (cit. on p. 17).

106. Maunz, P. *et al.* "Quantum Interference of Photon Pairs from Two Remote Trapped Atomic Ions". *Nature Physics* **3,** 538–541 (8 2007) (cit. on p. 17).

107. Lettner, M. *et al.* "Remote Entanglement between a Single Atom and a Bose-Einstein Condensate". *PRL* **106,** 210503 (2011) (cit. on pp. 17, 71).

108. Siyushev, P., Stein, G., Wrachtrup, J. & Gerhardt, I. "Molecular Photons Interfaced with Alkali Atoms". *Nature* **509,** 66–70 (2014) (cit. on pp. 17, 71).

109. Firstenberg, O., Adams, C. S. & Hofferberth, S. "Nonlinear Quantum Optics Mediated by Rydberg Interactions". *Journal of Physics B: Atomic, Molecular and Optical Physics* **49,** 152003 (2016) (cit. on p. 17).

110. Lukin, M. D. *et al.* "Dipole Blockade and Quantum Information Processing in Mesoscopic Atomic Ensembles". *Physical Review Letters* **87,** 037901–4 (2001) (cit. on pp. 17, 71).

111. Dudin, Y. O. & Kuzmich, A. "Strongly Interacting Rydberg Excitations of a Cold Atomic Gas". *Science (New York, N.Y.)* **336,** 887–889 (2012) (cit. on pp. 17, 71).

112. Ripka, F., Kübler, H., Löw, R. & Pfau, T. "A Room-Temperature Single-Photon Source Based on Strongly Interacting Rydberg Atoms". *Science* **362,** 446–449 (2018) (cit. on p. 17).

113. Yang, C.-W. *et al.* "Deterministic Measurement of a Rydberg Superatom Qubit via Cavity-Enhanced Single-Photon Emission". *Optica* **9,** 853–858 (2022) (cit. on p. 17).

114. Chou, C. W. *et al.* "Measurement-Induced Entanglement for Excitation Stored in Remote Atomic Ensembles". *Nature* **438,** 828–832 (2005) (cit. on pp. 17, 19, 70).

115. Yuan, Z. S. *et al.* "Experimental Demonstration of a BDCZ Quantum Repeater Node". *Nature* **454,** 1098–1101 (2008) (cit. on pp. 18, 70).

116. Jing, B. *et al.* "Entanglement of Three Quantum Memories via Interference of Three Single Photons". *Nature Photonics* **13,** 210–213 (2019) (cit. on pp. 18, 37, 38, 96).

117. Yu, Y. *et al.* "Entanglement of Two Quantum Memories via Fibres over Dozens of Kilometres". *Nature* **578** (2020) (cit. on pp. 18, 19, 37, 38, 70).

118. Delteil, A. *et al.* "Generation of Heralded Entanglement between Distant Hole Spins". *Nature Physics* **12,** 218–223 (3 2016) (cit. on p. 18).

119. Stockill, R. *et al.* "Phase-Tuned Entangled State Generation between Distant Spin Qubits". *Physical Review Letters* **119,** 010503 (2017) (cit. on p. 18).

120. Van Leent, T. *et al.* "Entangling Single Atoms over 33 Km Telecom Fibre". *Nature* **607,** 69–73 (7917 2022) (cit. on pp. 18, 19).

121. Liu, X. *et al.* "Heralded Entanglement Distribution between Two Absorptive Quantum Memories". *Nature* **594,** 41–45 (7861 2021) (cit. on pp. 18, 70).

122. Hucul, D. *et al.* "Modular Entanglement of Atomic Qubits Using Photons and Phonons". *Nature Physics* **11,** 37–42 (1 2015) (cit. on p. 18).

123. Pu, Y.-F. *et al.* "Experimental Demonstration of Memory-Enhanced Scaling for Entanglement Connection of Quantum Repeater Segments". *Nature Photonics* **15,** 374–378 (2021) (cit. on p. 19).

124. Bhaskar, M. K. *et al.* "Experimental Demonstration of Memory-Enhanced Quantum Communication". *Nature* **580,** 60–64 (2020) (cit. on p. 19).

125. Langenfeld, S., Thomas, P., Morin, O. & Rempe, G. "Quantum Repeater Node Demonstrating Unconditionally Secure Key Distribution". *PRL* **126,** 230506 (2021) (cit. on p. 19).

126. Heller, L., Farrera, P., Heinze, G. & de Riedmatten, H. "Cold-Atom Temporally Multiplexed Quantum Memory with Cavity-Enhanced Noise Suppression". *Physical Review Letters* **124,** 210504 (2020) (cit. on pp. 19, 46, 56, 86, 116).

127. Heller, L., Lowinski, J., Theophilo, K., Padrón-Brito, A. & de Riedmatten, H. "Raman Storage of Quasideterministic Single Photons Generated by Rydberg Collective Excitations in a Low-Noise Quantum Memory". *Physical Review Applied* **18,** 024036 (2022) (cit. on pp. 19, 37, 69).

128. Tanji-Suzuki, H. *et al.* "Interaction between Atomic Ensembles and Optical Resonators. Classical Description". *Advances in Atomic, Molecular and Optical Physics* **60,** 201–237 (November 2011 2011) (cit. on pp. 21, 30).

129. Simon, J. "Cavity QED with Atomic Ensembles" (Harvard University, Cambridge, Massachusetts, 2010) (cit. on pp. 21, 30).

130. Simon, J., Tanji, H., Thompson, J. K. & Vuletić, V. "Interfacing Collective Atomic Excitations and Single Photons". *Physical Review Letters* **98,** 183601 (2007) (cit. on pp. 23, 26, 37, 46, 96).

131. Araújo, M. O., Krešić, I., Kaiser, R. & Guerin, W. "Superradiance in a Large and Dilute Cloud of Cold Atoms in the Linear-Optics Regime". *Physical Review Letters* **117,** 073002 (2016) (cit. on pp. 23, 24).

132. Gorshkov, A. V., André, A., Lukin, M. D. & Sørensen, A. S. "Photon Storage in Λ -Type Optically Dense Atomic Media. II. Free-space Model". *Physical Review A - Atomic, Molecular, and Optical Physics* **76,** 1–25 (2007) (cit. on pp. 24, 26, 28).

133. Bao, X.-H. "Quantum Information with Entangled Photons and Cold Atomic Ensembles" (Ruperto-Carola University of Heidelberg, Germany, 2010) (cit. on p. 24).

134. Bienaimé, T., Piovella, N. & Kaiser, R. "Controlled Dicke Subradiance from a Large Cloud of Two-Level Systems". *Physical Review Letters* **108,** 123602 (2012) (cit. on p. 24).

135. Nunn, J. *et al.* "Mapping Broadband Single-Photon Wave Packets into an Atomic Memory". *Physical Review A - Atomic, Molecular, and Optical Physics* **75,** 1–4 (2007) (cit. on pp. 27, 73, 84).

136. Reim, K. F. *et al.* "Towards High-Speed Optical Quantum Memories". *Nature Photonics* **4,** 218–221 (2010) (cit. on pp. 27, 28, 134).

137. Ding, D. S. *et al.* "Quantum Storage of Orbital Angular Momentum Entanglement in an Atomic Ensemble". *Physical Review Letters* **114,** 1–5 (2015) (cit. on pp. 27, 57).

138. Vernaz-Gris, P. *et al.* "High-Performance Raman Memory with Spatio-Temporal Reversal". *Optics Express* **26,** 12424 (2018) (cit. on pp. 27, 28, 84, 86).

139. Vitanov, N. V., Rangelov, A. A., Shore, B. W. & Bergmann, K. "Stimulated Raman Adiabatic Passage in Physics, Chemistry, and Beyond". *Reviews of Modern Physics* **89,** 015006 (2017) (cit. on p. 27).

140. Ho, M., Teo, C., de Riedmatten, H. & Sangouard, N. "Optimal Photon Generation from Spontaneous Raman Processes in Cold Atoms". *New Journal of Physics* **20,** 123018 (2018) (cit. on pp. 28, 88).

141. Nunn, J. "Quantum Memory in Atomic Ensembles" (University of Oxford, 2008) (cit. on pp. 28, 29, 85).

142. Fleischhauer, M., Imamoglu, A. & Marangos, J. P. "Electromagnetically Induced Transparency: Optics in Coherent Media". *Reviews of Modern Physics* **77,** 633–673 (2005) (cit. on p. 29).

143. Saglamyurek, E., Hrushevskyi, T., Cooke, L., Rastogi, A. & LeBlanc, L. J. "Single-Photon-Level Light Storage in Cold Atoms Using the Autler-Townes Splitting Protocol". *Physical Review Research* **1,** 022004 (2019) (cit. on pp. 29, 79, 80).

144. Main, D., Hird, T. M., Gao, S., Walmsley, I. A. & Ledingham, P. M. "Room Temperature Atomic Frequency Comb Storage for Light". *Optics Letters* **46,** 2960–2963 (2021) (cit. on p. 29).

145. Nunn, J. *et al.* "Multimode Memories in Atomic Ensembles". *Physical Review Letters* **101,** 1–4 (2008) (cit. on p. 29).

146. Albrecht, B., Farrera, P., Heinze, G., Cristiani, M. & de Riedmatten, H. "Controlled Rephasing of Single Collective Spin Excitations in a Cold Atomic Quantum Memory". *Physical Review Letters* **115,** 160501 (2015) (cit. on pp. 33, 56–58, 62, 78).

147. Radnaev, A. G. *et al.* "A Quantum Memory with Telecom-Wavelength Conversion". *Nature Physics* **6,** 894–899 (2010) (cit. on pp. 33, 34, 66, 102).

148. Jiang, Y., Rui, J., Bao, X.-H. & Pan, J.-W. "Dynamical Zeroing of Spin-Wave Momentum to Suppress Motional Dephasing in an Atomic-Ensemble Quantum Memory". *Physical Review A* **93,** 063819 (2016) (cit. on pp. 33, 38, 66).

149. Timoney, N., Lauritzen, B., Usmani, I., Afzelius, M. & Gisin, N. "Atomic Frequency Comb Memory with Spin-Wave Storage in 153Eu3 +:Y2SiO5". *Journal of Physics B: Atomic, Molecular and Optical Physics* **45,** 124001 (2012) (cit. on p. 34).

150. Dudin, Y. O., Zhao, R., Kennedy, T. A. & Kuzmich, A. "Light Storage in a Magnetically Dressed Optical Lattice". *Physical Review A - Atomic, Molecular, and Optical Physics* **81,** 1–4 (2010) (cit. on p. 34).

151. Farrera, P., Heinze, G. & De Riedmatten, H. "Entanglement between a Photonic Time-Bin Qubit and a Collective Atomic Spin Excitation". *Physical Review Letters* **120,** 100501 (2018) (cit. on pp. 35, 57, 96).

152. Da Ros, E., Kanthak, S., Sağlamyürek, E., Gündoğan, M. & Krutzik, M. *Proposal for a Long-Lived Quantum Memory Using Matter-Wave Optics with Bose-Einstein Condensates in Microgravity*. `http://arxiv.org/abs/2210.13859` (2022). preprint (cit. on p. 36).

153. Saunders, D. J. *et al.* "Cavity-Enhanced Room-Temperature Broadband Raman Memory". *Physical Review Letters* **116,** 090501 (2016) (cit. on pp. 37, 91).

154. Li, Y. *et al.* "Noise Suppression in a Temporal-Multimode Quantum Memory Entangled with a Photon via an Asymmetrical Photon-Collection Channel". *Physical Review A* **106,** 022610 (2022) (cit. on p. 37).

155. Laurat, J. *et al.* "Efficient Retrieval of a Single Excitation Stored in an Atomic Ensemble". *Optics Express* **14,** 6912 (2006) (cit. on pp. 37, 87, 88).

156. Bimbard, E. *et al.* "Homodyne Tomography of a Single Photon Retrieved on Demand from a Cavity-Enhanced Cold Atom Memory". *Physical Review Letters* **112,** 033601 (2014) (cit. on pp. 37, 88).

157. Luo, X.-Y. *et al. Entangling Metropolitan-Distance Separated Quantum Memories*. 2022 (cit. on pp. 38, 96).

158. Steck, D. A. *Rubidium 87 D Line Data* ((revision 2.2.2, 9 July 2021)) (cit. on pp. 40, 43, 46).

159. Foot, C. J. *Atomic Physics*. 346 pp. (Oxford University Press, 2005) (cit. on pp. 41, 44).

160. Dalibard, J. & Cohen-Tannoudji, C. "Laser Cooling below the Doppler Limit by Polarization Gradients: Simple Theoretical Models". *Journal of the Optical Society of America B* **6,** 2023 (1989) (cit. on p. 43).

161. Albrecht, B. "Quantum Control of Single Spin Excitations in Cold Atomic Quantum Memories" (UPC, Institut de Ciències Fotòniques, 2015) (cit. on pp. 45, 96, 107).

162. Farrera Soler, P. "A Versatile Source of Light-Matter Quantum States Based on Laser-Cooled Atoms" (UPC, Institut de Ciències Fotòniques, 2018) (cit. on p. 45).

163. Zhao, B. *et al.* "A Millisecond Quantum Memory for Scalable Quantum Networks". *Nature Physics* **5,** 95–99 (2 2009) (cit. on p. 46).

164. Palittapongarnpim, P., MacRae, A. & Lvovsky, A. I. "A Monolithic Filter Cavity for Experiments in Quantum Optics". *Review of Scientific Instruments* **83,** 066101 (2012) (cit. on pp. 49, 123).

165. Albrecht, B., Farrera, P., Fernandez-Gonzalvo, X., Cristiani, M. & de Riedmatten, H. "A Waveguide Frequency Converter Connecting Rubidium-Based Quantum Memories to the Telecom C-band". *Nature communications* **5,** 3376 (2014) (cit. on p. 51).

166. Reid, M. D. & Walls, D. F. "Violations of Classical Inequalities in Quantum Optics". *Physical Review A* **34,** 1260–1276 (1986) (cit. on p. 52).

167. Lan, S.-Y. *et al.* "A Multiplexed Quantum Memory". *Optics Express* **17,** 13639–13645 (2009) (cit. on p. 57).

168. Nicolas, A. *et al.* "A Quantum Memory for Orbital Angular Momentum Photonic Qubits". *Nat Photon* **8,** 234–238 (2014) (cit. on p. 57).

169. Wang, S.-z. *et al.* "Long-Lived and Multiplexed Atom-Photon Entanglement Interface with Feed-Forward-Controlled Readouts". *Communications Physics* **4,** 1–9 (1 2021) (cit. on p. 57).

170. Laplane, C., Jobez, P., Etesse, J., Gisin, N. & Afzelius, M. "Multimode and Long-Lived Quantum Correlations between Photons and Spins in a Crystal". *Physical Review Letters* **118,** 210501 (2017) (cit. on p. 57).

171. Yang, T.-S. *et al.* "Multiplexed Storage and Real-Time Manipulation Based on a Multiple Degree-of-Freedom Quantum Memory". *Nature Communications* **9,** 3407 (2018) (cit. on p. 57).

172. Usmani, I., Afzelius, M., de Riedmatten, H. & Gisin, N. "Mapping Multiple Photonic Qubits into and out of One Solid-State Atomic Ensemble". *Nature communications* **1,** 12– (2010) (cit. on p. 57).

173. Clausen, C. *et al.* "Quantum Storage of Photonic Entanglement in a Crystal". *Nature* **469,** 508–511 (2011) (cit. on p. 57).

174. Saglamyurek, E. *et al.* "Broadband Waveguide Quantum Memory for Entangled Photons". *Nature* **469,** 512–515 (2011) (cit. on p. 57).

175. Gündoğan, M., Ledingham, P. M., Kutluer, K., Mazzera, M. & de Riedmatten, H. "Solid State Spin-Wave Quantum Memory for Time-Bin Qubits". *Physical Review Letters* **114,** 230501– (2015) (cit. on pp. 57, 80).

176. Jobez, P. *et al.* "Towards Highly Multimode Optical Quantum Memory for Quantum Repeaters". *Physical Review A* **93,** 032327 (2016) (cit. on p. 57).

177. Seri, A. *et al.* "Quantum Correlations between Single Telecom Photons and a Multimode On-Demand Solid-State Quantum Memory". *Physical Review X* **7,** 021028 (2017) (cit. on pp. 57, 80).

178. Kutluer, K., Mazzera, M. & De Riedmatten, H. "Solid-State Source of Nonclassical Photon Pairs with Embedded Multimode Quantum Memory". *Physical Review Letters* **118,** 210502 (2017) (cit. on p. 57).

179. Glorieux, Q., Clark, J. B., Marino, A. M., Zhou, Z. & Lett, P. D. "Temporally Multiplexed Storage of Images in a Gradient Echo Memory". *Optics Express* **20,** 12350–12358 (2012) (cit. on p. 57).

180. Wen, Y. *et al.* "Multiplexed Spin-Wave–Photon Entanglement Source Using Temporal Multimode Memories and Feedforward-Controlled Readout". *Physical Review A* **100,** 012342 (2019) (cit. on p. 57).

181. Li, C. *et al.* "Quantum Communication between Multiplexed Atomic Quantum Memories". *Physical Review Letters* **124,** 1–9 (2020) (cit. on p. 57).

182. Simon, C., de Riedmatten, H. & Afzelius, M. "Temporally Multiplexed Quantum Repeaters with Atomic Gases". *Physical Review A: Atomic, Molecular, and Optical Physics* **82,** 010304 (2010) (cit. on pp. 58, 60, 96).

183. Wilmsen, C., Temkin, H. & Coldren, L. *Vertical-Cavity Surface-Emitting Lasers: Design, Fabrication, Characterization, and Applications* (Cambridge University Press, Cambridge, UK, 1999) (cit. on p. 63).

184. Yang, S. J., Wang, X. J., Bao, X. H. & Pan, J. W. "An Efficient Quantum Light-Matter Interface with Sub-Second Lifetime". *Nature Photonics* **10,** 381–384 (2016) (cit. on p. 66).

185. Sparkes, B. M., Hosseini, M., Hétet, G., Lam, P. K. & Buchler, B. C. "Ac Stark Gradient Echo Memory in Cold Atoms". *Physical Review A* **82,** 043847 (2010) (cit. on p. 66).

186. Parniak, M. *et al.* "Quantum Optics of Spin Waves through Ac Stark Modulation". *Physical Review Letters* **122** (2019) (cit. on p. 66).

187. Ding, D. S. *et al.* "Raman Quantum Memory of Photonic Polarized Entanglement". *Nature Photonics* **9,** 332–338 (2015) (cit. on pp. 70, 79, 80).

188. Kroh, T. *et al.* "Slow and Fast Single Photons from a Quantum Dot Interacting with the Excited State Hyperfine Structure of the Cesium D1-line". *Scientific Reports* **9,** 13728 (2019) (cit. on p. 71).

189. Maxwell, D. *et al.* "Storage and Control of Optical Photons Using Rydberg Polaritons". *Physical Review Letters* **110,** 1–7 (2013) (cit. on p. 71).

190. Li, L. & Kuzmich, A. "Quantum Memory with Strong and Controllable Rydberg-level Interactions". *Nature Communications* **7,** 13618 (2016) (cit. on p. 71).

191. Li, J. *et al.* "Semideterministic Entanglement between a Single Photon and an Atomic Ensemble". *PRL* **123,** 140504 (2019) (cit. on p. 71).

192. Li, L., Dudin, Y. O. & Kuzmich, A. "Entanglement between Light and an Optical Atomic Excitation." *Nature* **498,** 466–9 (2013) (cit. on p. 71).

193. Padrón-Brito, A., Lowinski, J., Farrera, P., Theophilo, K. & de Riedmatten, H. "Probing the Indistinguishability of Single Photons Generated by Rydberg Atomic Ensembles". *Physical Review Research* **3,** 033287 (2021) (cit. on pp. 71, 75, 117).

194. Yu, Y. *et al.* "Measurement-Device-Independent Verification of a Quantum Memory". *Physical Review Letters* **127,** 160502 (2021) (cit. on p. 72).

195. Lettner, M. "Ein Bose-Einstein-Kondensat Als Quantenspeicher Für Zwei-Teilchen-Verschränkung" (Technische Universität München, München, 2011) (cit. on pp. 79, 80).

196. Saglamyurek, E. *et al.* "Storing Short Single-Photon-Level Optical Pulses in Bose–Einstein Condensates for High-Performance Quantum Memory". *New Journal of Physics* **23,** 043028 (2021) (cit. on pp. 79, 80).

197. Thomas, S. E. *et al.* "Raman Quantum Memory with Built-in Suppression of Four-Wave-Mixing Noise". *Physical Review A: Atomic, Molecular, and Optical Physics* **100,** 033801 (2019) (cit. on p. 80).

198. Namazi, M., Kupchak, C., Jordaan, B., Shahrokhshahi, R. & Figueroa, E. "Ultralow-Noise Room-Temperature Quantum Memory for Polarization Qubits". *Physical Review Applied* **8,** 034023 (2017) (cit. on p. 80).

199. Hong, C. K., Ou, Z. Y. & Mandel, L. "Measurement of Subpicosecond Time Intervals between Two Photons by Interference". *Physical Review Letters* **59,** 2044– (1987) (cit. on pp. 81, 117).

200. Legero, T., Wilk, T., Kuhn, A. & Rempe, G. "Time-Resolved Two-Photon Quantum Interference". *Applied Physics B* **77,** 797–802 (2003) (cit. on p. 81).

201. Reim, K. F. *et al.* "Multipulse Addressing of a Raman Quantum Memory: Configurable Beam Splitting and Efficient Readout". *Physical Review Letters* **108,** 263602 (2012) (cit. on p. 83).

202. Gorshkov, A. V., André, A., Lukin, M. D. & Sørensen, A. S. "Photon Storage in Λ -Type Optically Dense Atomic Media. I. Cavity Model". *Physical Review A* **76,** 1–16 (2007) (cit. on p. 84).

203. Sheremet, A. S. *et al.* "Quantum Memory for Light via a Stimulated Off-Resonant Raman Process: Beyond the Three-Level Λ-scheme Approximation". *Physical Review A - Atomic, Molecular, and Optical Physics* **82** (2010) (cit. on p. 84).

204. Chen, Y. H. *et al.* "Coherent Optical Memory with High Storage Efficiency and Large Fractional Delay". *Physical Review Letters* **110,** 1–5 (2013) (cit. on p. 84).

205. Yang, C.-W. *et al. Sequential Generation of Multiphoton Entanglement with a Rydberg Superatom*. 2021 (cit. on p. 86).

206. Gorshkov, A. V., André, A., Fleischhauer, M., Sørensen, A. S. & Lukin, M. D. "Universal Approach to Optimal Photon Storage in Atomic Media". *Physical Review Letters* **98,** 123601 (2007) (cit. on pp. 87, 134).

207. Surmacz, K. *et al.* "Efficient Spatially Resolved Multimode Quantum Memory". *Physical Review A - Atomic, Molecular, and Optical Physics* **78,** 1–9 (2008) (cit. on p. 88).

208. Wang, M. *et al. Generation of Perfect-Cavity-Enhanced Atom-Photon Entanglement with a Millisecond Lifetime via a Spatially-Multiplexed Cavity*. 2021 (cit. on pp. 88, 96, 99).

209. Agarwal, G. S. "Vacuum-Field Rabi Splittings in Microwave Absorption by Rydberg Atoms in a Cavity". *Physical Review Letters* **53,** 1732–1734 (1984) (cit. on pp. 89, 139).

210. Cox, K. C., Meyer, D. H., Schine, N. A., Fatemi, F. K. & Kunz, P. D. *30-Fold Increase in Atom-Cavity Coupling Using a Parabolic Ring Cavity*. 2018 (cit. on p. 89).

211. Cox, K. C., Meyer, D. H., Castillo, Z. A., Fatemi, F. K. & Kunz, P. D. "Spin-Wave Multiplexed Atom-Cavity Electrodynamics". *Physical Review Letters* **123,** 1–6 (2019) (cit. on p. 89).

212. Ma, L. *et al.* "High-Performance Cavity-Enhanced Quantum Memory with Warm Atomic Cell". *Nature Communications* **13,** 2368 (1 2022) (cit. on p. 91).

213. Borregaard, J. *et al.* "Scalable Photonic Network Architecture Based on Motional Averaging in Room Temperature Gas". *Nature Communications* **7,** 11356 (1 2016) (cit. on p. 91).

214. Maring, N. "Quantum Frequency Conversion for Hybrid Quantum Networks" (2018) (cit. on pp. 96, 107, 112).

215. Grimm, R., Weidemüller, M. & Ovchinnikov, Y. B. *Optical Dipole Traps for Neutral Atoms*. 1999 (cit. on p. 99).

216. *Nonlinear Optics* 4th ed. (ed Boyd, R. W.) (Academic Press, 2020) (cit. on pp. 106, 107).

217. Zaske, S., Lenhard, A. & Becher, C. "Efficient Frequency Downconversion at the Single Photon Level from the Red Spectral Range to the Telecommunications C-band". *Optics Express* **19,** 12825–12836 (2011) (cit. on p. 109).

218. Siegman, A. E. *Lasers*. 1322 pp. (University Science Books, 1986) (cit. on p. 119).

219. Bao, X. H. *et al.* "Efficient and Long-Lived Quantum Memory with Cold Atoms inside a Ring Cavity". *Nature Physics* **8,** 517–521 (2012) (cit. on p. 129).

220. De Riedmatten, H. *et al.* "Direct Measurement of Decoherence for Entanglement between a Photon and Stored Atomic Excitation". *Physical Review Letters* **97,** 113603–4 (2006) (cit. on p. 130).